Image Analysis of Retinal Changes in Eyes with Ophthalmic Diseases

August 2022

Tin Tin Khaing

Graduate School of Science and Engineering

CHIBA UNIVERSITY

（千葉大学審査学位論文）

Image Analysis of Retinal Changes in Eyes with Ophthalmic Diseases

August 2022

Tin Tin Khaing

Graduate School of Science and Engineering

CHIBA UNIVERSITY

Contents

List of Figures

Chapter-1

Chapter-2

Chapter-3

Chapter-4

Chapter-5

Chapter-6

Chapter-7

Chapter-8

List of Tables

Chapter-4

Chapter-5

Chaper-7

List of Acronyms

AC	Active Contour
ADI-GVF	Alternative Deflation/Inflation Gradient Vector Flow
ChoroidNET	Choroid segmentation Network
CNN	Convolutional Neural Network
CNV	Choroid NeoVascularization
CT	Choroidal Thickness
CTM	Circular Transform Method
DIARETDB0	DIAbetic RETinopathy DataBase with calibration level 0
DIARETDB1	DIAbetic RETinopathy DataBase with calibration level 1
DME	Diabetic Macular Edema
DR	Diabetic Retinopathy
DRUNET	Dilated-Residual U-Net
EDI-OCT	Enhanced-Depth Imaging Optical Coherence Tomography
EM	Exclusion Method
EM-ACCF	EM combined with Active Contour and Circle Fitting
FAC	Factorization-based Active Contour
FC	Fuzzy Convergence Method
FOV	Field Of View
GT	Ground Truth
GVF	Gradient Vector Flow
HLM	Hybrid Localization Method
HLM-ACCF	HLM combined with Active Contour and Circle Fitting
HLM-FAC	HLM combined with Factorization-based Active Contour
HM	Hybrid Method
ICC	Intraclass Correlation Coefficient
ILM	Internal Limiting Membrane
LA	Luminal Area
LDM	Line Detection Method
LDM-ACCF	LDM combined with Active Contour and Circle Fitting
LSM	Layer Segmentation Module
OCT	Optical Coherence Tomography
OC	Optic Cup
OD	Optic Disc
ODE	Optic Disc Edema

PR-AUC	Precision-Recall Area Under the Curve
ReLU	Rectified Linear Unit
ROC-AUC	Receiver Operator Characteristics Area Under the Curve
ROI	Region Of Interest
RP	Retinitis Pigmentosa
RPE	Retinal Pigmented Epithelium
SA	Stromal Area
SD-OCT	Spectral-Domain Optical Coherence Tomography
SS	Scale Space Algorithm
SSHM	Scale Space Algorithm with Hybrid Method
SSVT	Scale Space Algorithm with Vessel Transform
SSVVPPA	Scale Space Algorithm with Vessel Vector-based Phase Portrait Analysis
SS-OCT	Swept-Source Optical Coherence Tomography
STARE	STructured Analysis of the REtina
TCA	Total Choroidal Area
VSM	Vessel Segmentation Module
VT	Vessel Transform
VVPPA	Vessel Vector-based Phase Portrait Analysis

Chapter 1

Introduction

Chapter 1 Introduction

This chapter introduces the background and provides an overview of this thesis. The anatomy of a human's retina and its related components are described in Section 1.1. The pathology of the retina changes in various ophthalmic diseases. Some clinical backgrounds related to retinal changes are presented in Section 1.2. Section 1.3 discusses retinal imaging techniques which are broadly used in the diagnosis and management of ophthalmic diseases. The problem statement and the purpose of this study are described in Sections 1.4 and 1.5. Lastly, the arrangement of this thesis is shown in Section 1.6.

1.1 Retina and related components

Visual perception (Figure 1.1) begins when an eye focuses light onto the retina, where the light is absorbed by a layer of photoreceptor cells (called rods and cones). In particular, the retina is an ocular extension of the brain to perform the interpretation of visual signals and object recognition. It sends sensory information from the outside world to the brain's visual cortex through the optic nerve in the form of coded electrical impulses. It is an essential part of the optical system and also an approachable part of the brain. Understanding its functions and structures is of fundamental importance.

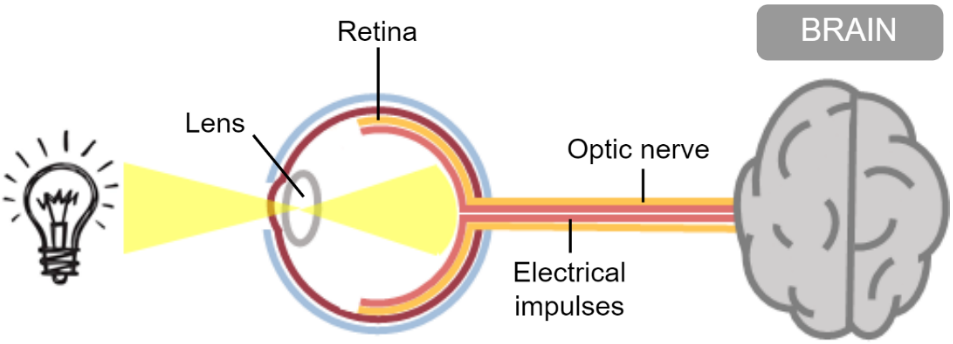

Figure 1.1 Visual perception process.

The retina is a complex transparent tissue consisting of several layers. It includes the neural retina and the retinal pigmented epithelium (RPE), separating the neural retina and the choroid coat of the eye. The neural retina comprises various types of neurons, such as the retinal ganglion cells, the amacrine cell, the bipolar cells, the horizontal cells, and the photoreceptor cells. RPE is a pigmented cell layer that nourishes the neural retina. It is composed of hexagon cells that are densely packed with pigment granules. The choroid is a vascular layer that contains choroidal vessels embedded in connective tissues. The optic nerve is formed by the convergence of retinal ganglion cells at the optic disc (OD). The OD is a blind spot where photoreceptors are absent. Figure 1.2 illustrates the components in the retina.

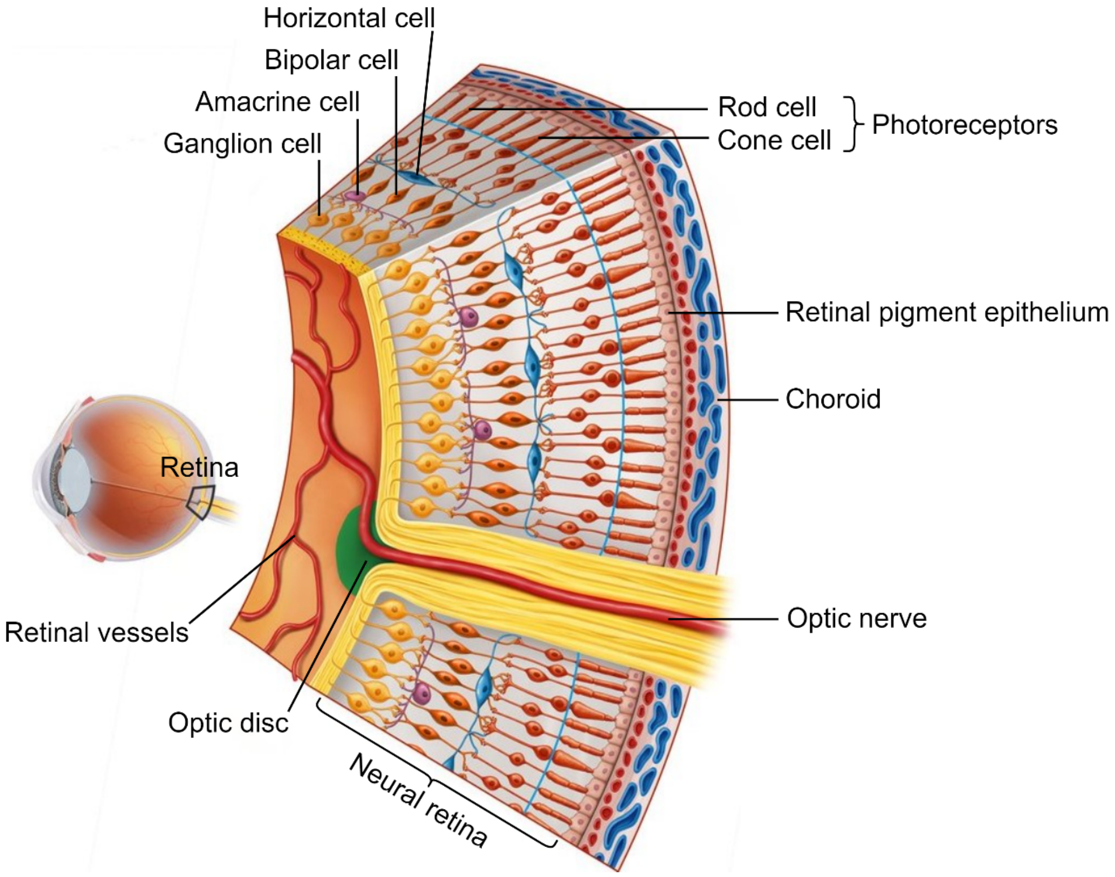

Figure 1.2 Retina and related components.

(Image downloaded from *www.kenhub.com*. Accessed date: 23 August 2021)

1.2 Clinical background related to retinal changes

Visual impairment and loss of vision affect an individual's public health and ability to participate in educational activities or work. It leads to a reduction in the quality of life with a life-threatening condition. The vision loss expert group predicted trends in the prevalence of blindness and vision impairment over 30 years [1]. The number of people with blindness and visual impairment (with moderate to severe symptoms) worldwide is estimated to grow to 61 million and 474 million by 2050. According to a recent nationwide survey [2] of certified visual impaired individuals in Japan, the leading causes of visual impairment are chronic diseases associated with aging and other lifestyle-related risk factors. The most common disease was reported as glaucoma (28.6%), followed by retinitis pigmentosa (14%) and diabetic retinopathy (12.8%) [2] (see Figure 1.3).

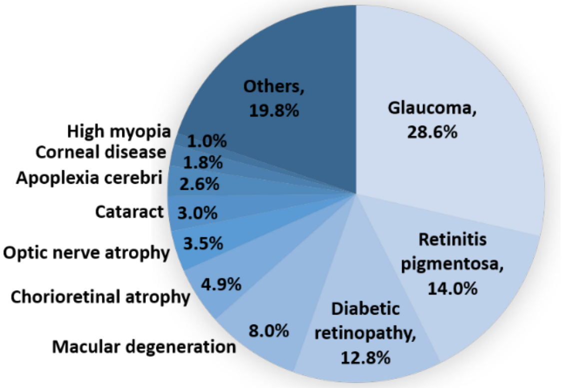

Figure 1.3 Distribution of retinal diseases among all certified visual impaired individuals [2].

Chronic conditions such as glaucoma and diabetes can interfere with the eye's health, characterized by a steady deterioration of vision. Most conditions commonly damage components of the retina such as the fovea, the OD, and retinal vessels. Eyes with chronic retinal diseases may experience different signs and symptoms according to the characteristics and severity of specific conditions. The details of the top three most common diseases are described in the following subsections.

1.2.1 Glaucoma

Glaucoma is an eye disorder that causes enlargement of the optic nerve head area, including the OD and the optic cup, due to intracranial pressure elevation. Glaucoma is primarily classified into open-angle and closed-angle (also called angle-closure). Open-angle glaucoma happens when the intracranial pressure in an eye increases gradually due to the clogging of drainage between the cornea and iris. It is the most common form of glaucoma, found in 90% of glaucomatous patients. Closed-angle glaucoma occurs when the drainage angle is completely blocked. The cerebrospinal fluid cannot circulate properly through the eye to the optic nerve, resulting in an unexpected and rapid increase in intracranial pressure. All types of glaucoma cause loss of peripheral vision at first and lead to blindness. A patient may not notice visual changes and symptoms until a late stage of glaucoma. Regular eye examinations are crucial for the early diagnosis to avoid irreversible vision loss. Analyzing the OD and OC abnormalities through retinal imaging is promising in diagnosing and managing glaucoma. A glaucomatous retinal image and a vision with glaucoma are shown in Figure 1.4 (a). Glaucoma is mainly diagnosed based on intracranial pressure, visual acuity examination, and OD and OC assessment from digital fundus images.

1.2.2 Retinitis pigmentosa (RP)

RP is a group of chronic and inherited disorders characterized by progressive bilateral degeneration of photoreceptor cells and pigmentary changes in the retina. Each cell in the body comprises 23 pairs of chromosomes: a pair of X and Y chromosomes (that determines the gender of a person) and 22 autosomal pairs of chromosomes. RP can be inherited in one of three ways: autosomal recessive inheritance, autosomal dominant inheritance, and X-linked inheritance. There are four types of photoreceptors in a human's retina. They are a single type of rods, long-wavelength (red-sensing) cones, medium-wavelength (green-sensing) cones, and short-wavelength (blue-sensing) cones. Rods are responsible for scotopic vision (appearing in black and white) and motion detection, whereas cones are responsible for photopic vision. In most forms of RP, rods are harmed first; consequently, a patient with RP may experience peripheral and night vision loss. When the disease progresses, and cones become affected, color perception and central vision can also be damaged. In preliminary research, choroidal thinning and a decrease in choroidal vasculature are suggested as a preclinical stage of photoreceptors degeneration in eyes with RP [3]. A retinal image with RP and a night-blind vision due to RP are illustrated in Figure 1.4 (b). RP is mainly diagnosed based on pigmentary deposits in digital fundus images and the choroidal changes in optical coherence tomography images.

1.2.3 Diabetic retinopathy (DR)

DR is a common complication of diabetes, characterized by progressive damage to the retina's blood vessels and leaking fluid in the retina. DR is generally classified into two types: non-proliferate DR, which refers to the early stages of the disease, and proliferate DR, which is an advanced stage. In mild and moderate non-proliferate stages, small lesions (called microaneurysms) appear, and the retinal vessels, supplying oxygen and nourishment to the neural retina, swell and deteriorate. With distorted retinal vessels, blood transportation becomes blocked, and new vessels start to grow at the severe stage of non-proliferate DR. In the proliferate DR stage, newly developed blood vessels leak into the vitreous. This causes blurry vision and reduced visual acuity and threatens vision. DR impairs the optic nerve, causing diabetic papillitis and neovascularization of the OD. Early retinal screening is a standard of care for patients with DR. It helps patients prevent possible blindness. Thus, all people with diabetes should attend an annual clinical check-up. DR-related retinal image and its vision are shown in Figure 1.4 (c). The primary diagnosis of DR is made by analyzing the presence of microaneurysms, exudates, or hemorrhages in digital fundus images. To detect those abnormalities effectively, OD detection is performed as an initial essential process for removing the OD in advance.

1.3 Retinal imaging techniques

Eye specialists and ophthalmologists document the presence of eye diseases and the retina changes over time. There are several imaging tools to diagnose and manage various retinal diseases. They are retinal fundus imaging, optical coherence tomography (OCT) [4], OCT angiography, autofluorescence imaging, and scanning laser ophthalmology. This thesis mainly analyzes fundus and OCT images of retinas with various diseases. The fundus imaging and OCT imaging techniques are mentioned as follows.

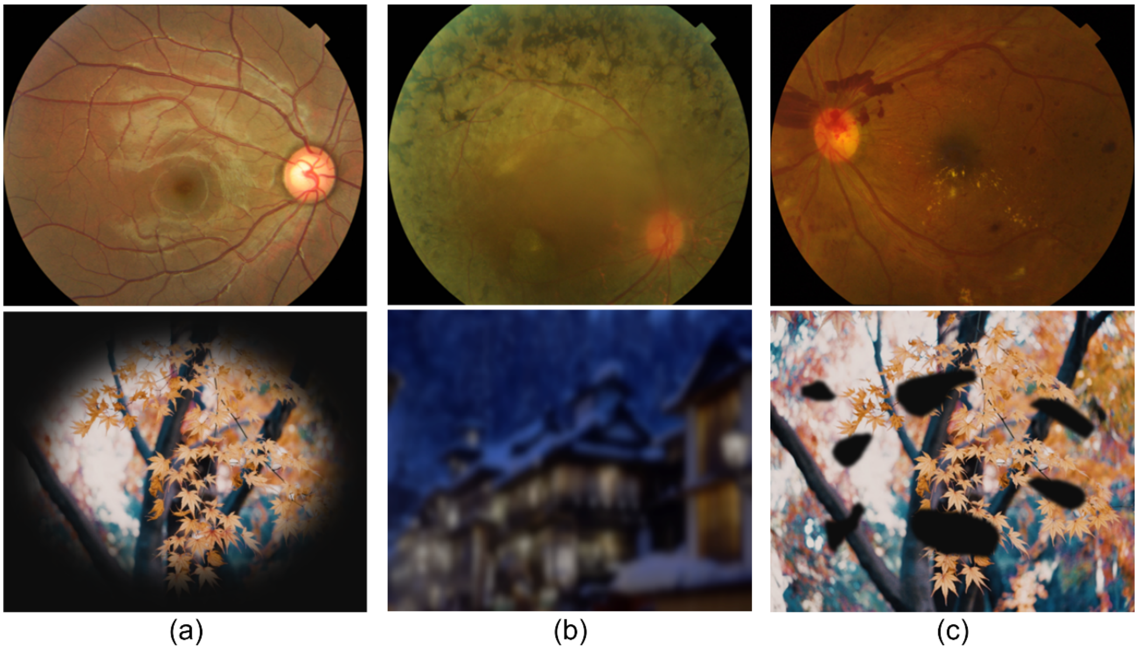

Figure 1.4 Retinal images and vision of (a) an eye with glaucoma, (b) an eye with RP, and (c) an eye with DR.

Retinal fundus imaging

Fundus imaging using standard slit-lamp machines is a fundamental technique to take a fundus photograph that records a color image of the inner surface of the eye, including the retina, retinal vessels, fovea, macula, the OD. It has evolved over the last century and improved by digital cameras and new innovative optical techniques. With a growing aging and vision-impaired population, the demand for eye screening services is increasing worldwide. With an advance in telemedicine programs, smartphone-attached portable fundus cameras make retinal imaging more efficient and offer cost-effectiveness and the possibility of remote diagnosis, especially in rural areas. The use of portable fundus cameras is thus gaining popularity in recent years over traditional equipment. Figure 1.5 shows examples of fundus imaging techniques, including standard equipment and smartphone-attached portable cameras widely used in clinical practice.

Optical coherence tomography (OCT)

The great advance in retinal imaging has come from OCT which allows acquiring a cross-sectional image of the retina while fundus imaging does not. OCT was suggested as a diagnostic imaging method with the ability to detect abnormalities through retinal layers [5]. Based on the principle of Michelson interferometry, OCT detects interference of low-coherent and infra-red light reflected from a reference arm and the object (the retina) when the distance between the light source and the reference arm is equal to the distance between the light source and the retina. The detector then processes the inference into a signal (called A-scan). The light source across the retina acquires a two-dimensional OCT image (called B-scan). The OCT imaging principle is illustrated in Figure 1.6. Examples of OCT imaging devices are shown in Figure 1.7.

Figure 1.5 Fundus imaging techniques, (a) standard equipment (Image downloaded from *www.maridimedical.com/*. Accessed date: 8 October 2021) and (b) smartphone-attached portable cameras (Images downloaded from http://welchallyn.jp/iExaminer/ and https://www.volk.com/. Accessed date: 22 October 2021).

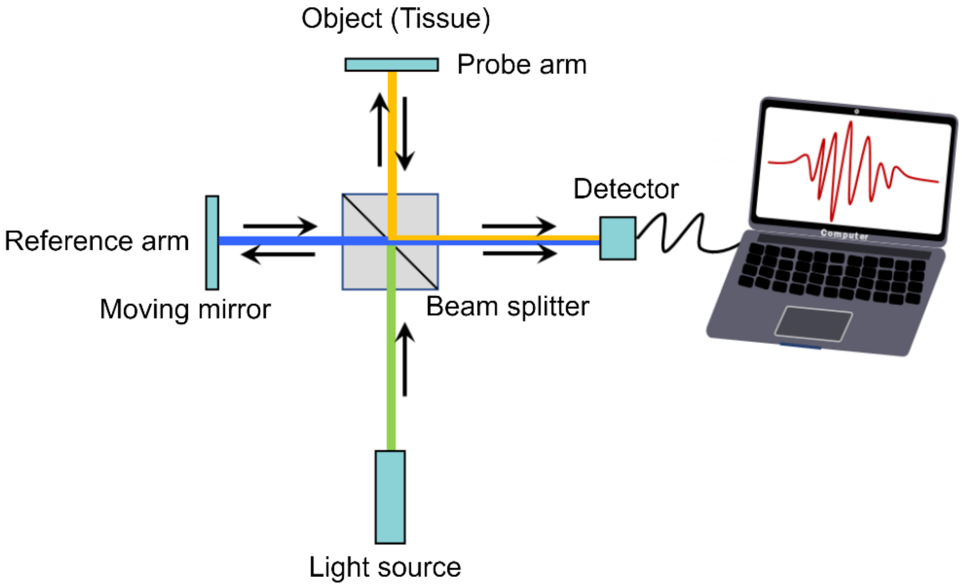

Figure 1.6 Principle of OCT imaging.

There are two types of OCT imaging systems standard in use, which are based on time-domain and spectral-domain. Conventional OCT imaging systems do not allow visualization of the structures below RPE, such as the choroid and the sclera, in detail because the hyperreflectivity of RPE prevents light from penetrating the deeper layers [6]. Swept-source OCT (SS-OCT) is a variation of Fourier-domain OCT that includes additional bulk optics components and a photodetection device. SS-OCT is recently applied as OCT angiography imaging. With the recent improvement of OCT, a new imaging mode, called enhanced depth imaging OCT (EDI-OCT), uses increased depth of field and a closer scanning position from spectral-domain OCT (SD-OCT) devices to the object [7]. Therefore, EDI-OCT could provide a more enhanced choroidal structure and a clearer choroid-sclera interface.

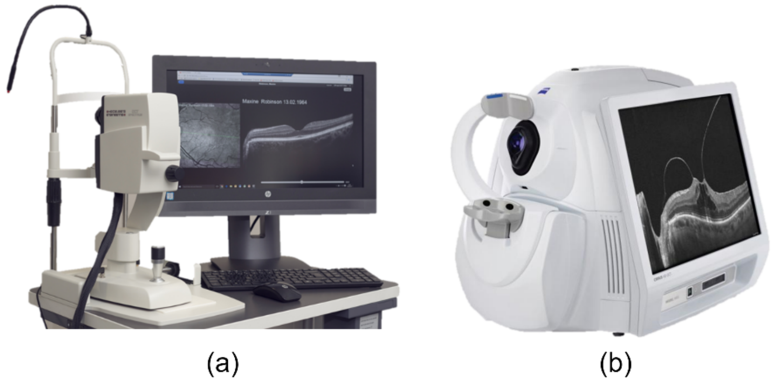

Figure 1.7 OCT imaging devices (a) from Heidelberg Engineering and (b) from ZEISS. (Images downloaded from https://www.heidelbergengineering.com/gb/en/products/ and https://www.zeiss.com/corporate/int/home.html. Accessed date: 22 October 2021)

1.4 Statement of problem

In the digital era, computer-aided diagnosis is becoming a subject of research in ophthalmology to alleviate the burden on eye doctors. Advancements in computer vision contribute to developing computer-aided systems for many retinal diseases such as DR, glaucoma, age-related macular degeneration, etc. Computerized systems ease clinicians dealing with a massive number of visually impaired patients. They help to save the necessity of resources and to minimize observer variability. Zhang et al. [8] conducted a survey on computer-aided diagnosis for ocular diseases based on clinical data (such as age, gender, intraocular pressure, etc.), image data (such as fundus images, OCT images, etc.), and genetic data (such as patient's DNA, genes, proteins, etc.). According to that survey, the analysis of OD in fundus images and the analysis of retinal layers in OCT images are the most prominent ways to diagnose and manage several ocular diseases. In this thesis, we present two different tasks according to the availability of image data. The first task is OD segmentation in fundus images with DR and with swelling OD, and the second is the analysis of choroidal structures in OCT images with RP. The details are described in Subsections 1.4.1 and 1.4.2.

1.4.1 Analysis of OD in retinal fundus images

Automatic segmentation of OD is a critical process for diagnosing and managing retinal diseases. Generally, the OD can be conveniently detected in a retinal image of a healthy subject based on its typical characteristics such as color, shape, and size. It is a bright and circular object that appears in fundus images. Its size in a fundus image depends on the camera's relative field of view (FOV). Hoover and Goldbaum [9] assumed that the OD occupies approximately one-sixth of an image’s width, acquired by a camera with a 35-degree field view. It is critical to trace other important objects such as the fovea or macula and other irregular regions such as exudate and hemorrhage. The images with an unhealthy retina may contain abnormal exudates, hemorrhage, or bright lesions that can be misclassified as OD. Besides, a damaged or swelling OD may have an atypical texture, size, and shape. To handle a large-scale screening in a clinical setting, the time complexity of the imaging and OD detection processes are essential to be considered.

Existing OD detection works have claimed a success rate close to 100% for retinal datasets acquired from standard machines. The smartphone-attached portable retinal lens is extensively used in clinical practice and research since it is easy to take an image, efficient in terms of cost and imaging time, and possible for remote diagnosis. Despite its advantages over traditional slit-lamp machines, it produces a poor-quality image with an incomplete vessel structure due to its narrow FOV and quality. Therefore, analyzing the retinal images acquired by smartphone cameras needs new computerized algorithms capable of processing lower-quality images. Figure 1.8 shows fundus images of an eye produced from a standard camera and a smartphone camera. Conclusively, the presence of retinal abnormalities and the aforementioned inaccuracies produced by smartphone cameras make OD detection a complex problem.

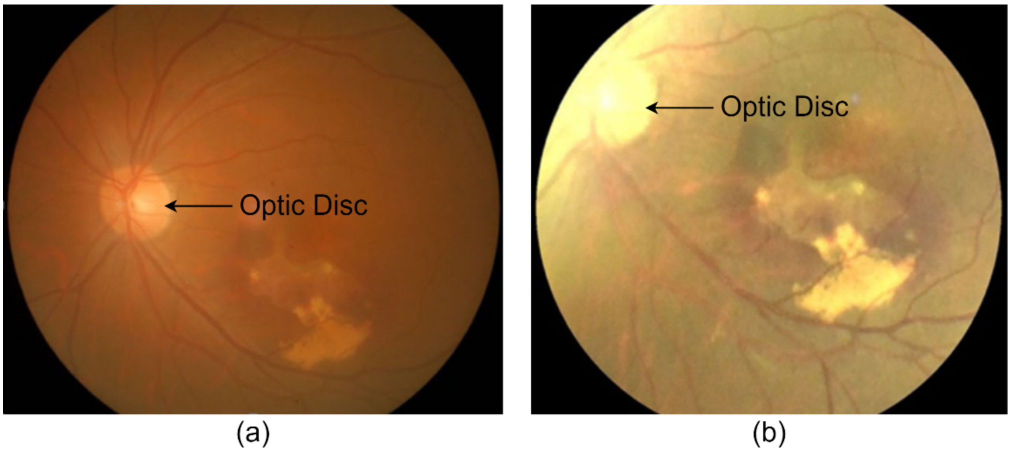

Figure 1.8 Fundus images acquired by (a) a standard camera and (b) a smartphone camera.

1.4.2 Analysis of choroidal structures in retinal OCT images

The choroid is a layer consisting of choroidal vessels (also called choroidal lumina) and elastic stromal tissues (also called choroidal stroma). It lies between RPE and the sclera and involves the diagnosis, prediction, and follow-up of acute or chronic choroidal and retinal disorders. The retina has two sources of oxygenation that supply oxygen and nourishment to the neural retina. They are retinal vasculature and choroidal vasculature. To maintain the metabolic and homeostatic functions of the retina, retinal oxygenation should be in a normoxia state with an adequate oxygen supply. Unbalanced blood flows from the retinal and choroidal vasculatures could lead to hyperoxia and hypoxia, which are early signs of retinal diseases [10]. Therefore, the choroidal vascular factor is one of the significant contributions to the pathogenesis of the eyes. The change in the choroidal thickness is also a vital biomarker that implicates in several diseases [11][12], including age-related macular degeneration [13][14], central serous chorioretinopathy [15], choroid neovascularization (CNV) which is a pathological state of age-related macular degeneration [16], diabetic macular edema (DME) [17], polypoidal choroidal vasculopathy [14], and RP [18][19].

Due to indistinct choroidal vessel structure, manual segmentation of choroids and choroidal vessels is tedious, time-consuming, and error-prone. There may have high variability among various observers. Thus, manual segmentation is not suitable for clinical practice. There are significant challenges for automatic choroid segmentation techniques. The Choroid-sclera interface (also denoted as the choroid outer boundary) is fuzzy and usually indistinguishable from the choroid. The choroid itself has an inhomogeneous texture due to the presence of choroidal vessels. Traditional image processing techniques are tireless and faster compared to manual segmentation. However, they are sensitive to the above challenges and the pathologies presented in images with diseased eyes. No existing work automatically segments the choroid layer and the choroidal vessels together and analyzes the choroidal structure based on the segmentation results. Figure 1.9 shows an EDI-OCT image of an eye with RP, indicating each component in the choroid.

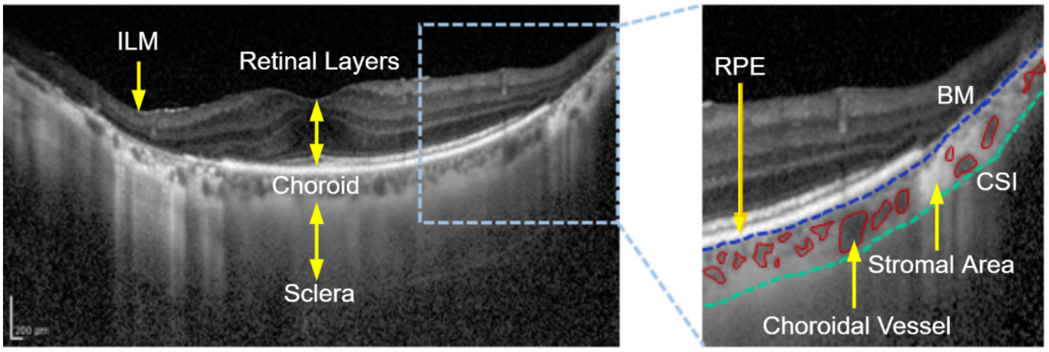

Figure 1.9 An OCT image of an eye with RP (left) and an enlarged image showing components of the choroid (right).

1.5 Purpose of study

In this thesis, we aim to present the analysis of OD and the choroidal structures based on image segmentation techniques and address the challenges and demands of computer-aided diagnostic systems in ophthalmology. Our work falls into two main categories. The overview of our work is shown in Figure 1.10. The objective of each work is described as follows.

1) The first work aims to develop fast and precise algorithms for detecting and segmenting the OD and swelling OD, also called OD edema (ODE), validated on fundus images acquired by a smartphone camera and standard equipment. We propose a hybrid OD localization method to detect the OD region, which is an important landmark in diagnosing DR. We also test the proposed method in detecting ODE. Then, the detected ODs are segmented using the active contour models. Moreover, the proposed method's performance will be evaluated using standard datasets and compared with other existing methods. Lastly, we aim for the proposed approach to yield high accuracies within a short computing time and to be able to apply compatibly to the fundus images regardless of the imaging device’s quality.

2) The second work aims to establish a deep learning model that offers a robust and precise segmentation of the choroid layer and choroidal vessels, which are clinically essential for analyzing the choroidal structures. We aim for the proposed model to be trained and tested on eyes with various retinal and choroidal diseases and to be superior to other existing models. Our ultimate goal is to measure the choroidal-related parameters such as the total choroid area, the luminal area, the stromal area, and the choroidal thickness to investigate the choroid-related diseases based on the segmentation results of the proposed model.

1.6 Thesis arrangement

The structure of this thesis is arranged as follows.

Chapter 2 describes existing OD detection and segmentation works in retinal fundus images.

Chapter 3 presents the proposed methods for OD detection and segmentation. In this chapter, the proposed hybrid OD localization method (HLM) based on the analysis of vessel structures is described. Then, the active contour models are then performed for segmenting the OD and ODE. The new experimental results are presented in this chapter.

Chapter 4 presents mobile-phone camera retinal datasets collected from patients with DR at Thammasat University Hospital of Thailand and public datasets used in our experiments. The experimental settings, the ground truth preparation, and evaluation metrics are also explained. The experimental results and discussion regarding OD segmentation are described in this chapter.

Chapter 5 describes related works of choroid layer and vessel segmentation in retinal OCT images.

Chapter 6 presents the proposed deep learning model for segmenting the choroid layer and choroidal vessels. The architecture of the proposed model is explained in this chapter. With segmentation results, the measurement of choroidal parameters is also described.

Chapter 7 presents a public OCT dataset that contains images with CNV, DME, Drusen, and of normal subjects and an OCT dataset collected from RP patients at Chiba University Hospital of Japan. The experimental settings and evaluation metrics are also explained. The experimental results of the segmentation and measurement process and discussion are described in this chapter.

Chapter 8 concludes the proposal and discusses the future tentative works and other perspectives.

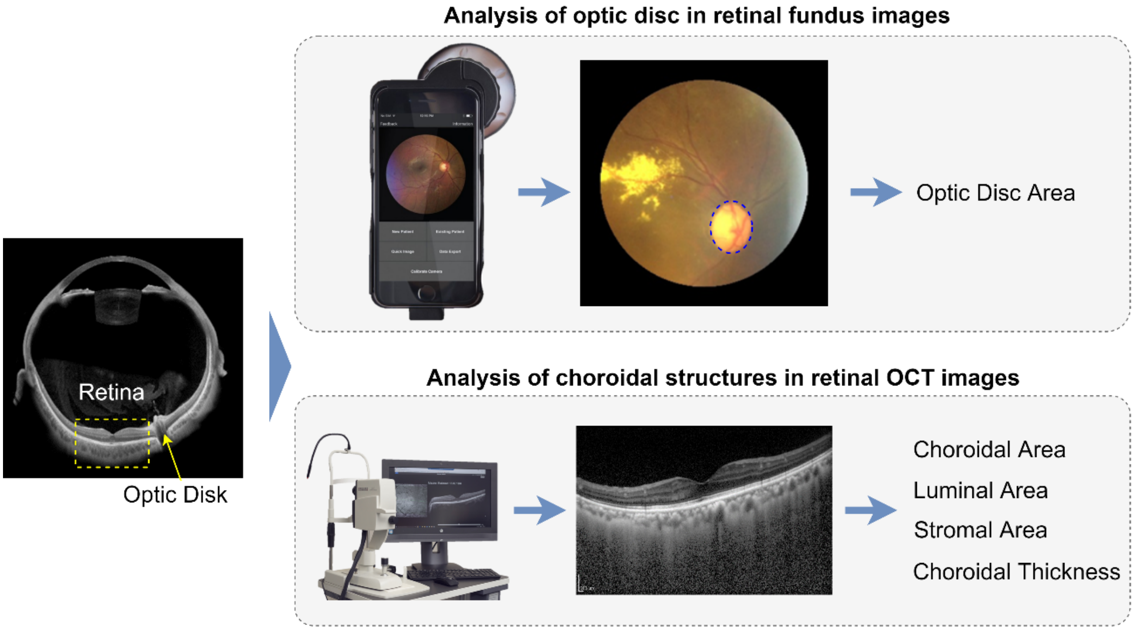

Figure 1.10 Overview of our work.

Chapter 2

Related works of optic disc detection and segmentation

Chapter 2 Related works of optic disc detection and segmentation

This chapter describes a brief analysis of recently published related works of OD detection and the clinical applications in which the OD area is essential. There are significant efforts to develop automatic OD detection and segmentation algorithms applied to retinal fundus images taken by standard devices. Several surveys on OD segmentation [20] and glaucoma classification using OD segmentation results [21-24] were conducted in preliminary research. The OD detection and segmentation methods are categorized according to their working principles: thresholding-based, level-set-based, active-contour and active shape model-based, clustering-based, component-based, vessel-based, and hybrid approaches.

2.1 Optic disc detection and segmentation

2.1.1 Thresholding-based techniques

Thresholding is the most time-efficient and straightforward segmentation technique. It creates a segmented image by selecting a threshold value to assign the binary values below and above that threshold. Noor et al. [25] segmented the OD using color multi-thresholding, differentiating the OD and the background pixels by analyzing the color values in each channel. Ruennark et al. [26] applied the optimal thresholding technique [27] based on histogram equalization, finding the brightest regions and merging the nearby areas. The centroid of the merged part is used as the initial OD location for segmenting the OD boundary. The thresholding-based technique is susceptible to abnormalities such as drusen, which have similar intensity values as the OD.

2.1.2 Level-set-based techniques

The level-set approach utilized the concept of curves and surfaces and was applied to detect the boundaries of the moving objects by evolving their contours. Esmaeili et al. [28] detected the potential OD location using the curvelet transform and the Canny edge detector. The OD boundary was extracted based on the variational level-set deformable model, in which the detected OD is used as the initial level-set contour. The contour deforms and moves toward the desired OD boundary in each iteration. The final OD contour was obtained after 150 iterations. Wang et al. [29] presented a two-layer level-set model in which the primary elliptic-shape constraint of the OD was introduced, which efficiently segments an elliptical object as the OD. The model forces the contours of the 0-level and k-level of the level-set function to approximate an ellipse during the deformation process. The level-set method may generate a curve passing through the OD boundary in a mobile camera image with poor contrast and uneven illumination.

2.1.3 Active contour and active shape model-based techniques

The active contour and active shape models mainly use an object's boundary and shape information. The active contour model finds the object contour by minimizing the energy function based on the internal energy, which controls the deformation of a snake, and the external energy, which exerts forces towards the contour. Naqvi et al. [30] proposed an OD segmentation method based on OD homogenization and active contours. It segments the OD in the presence of peripapillary atrophy, characterized by thinning of retinal layers around the OD area. Their method inpaints the major vessels interfering with the OD margin using local Laplacian filtering and applies the active contour model to estimate the OD boundary. Gao et al. [31] introduced the locally statistical active contour model to solve the intensity inhomogeneity issue caused by illumination variations. To preserve the appearance and shape of the OD, the local image probability information around the area of interest from a multidimensional feature space and the shape information were integrated into their model. Thus, their model becomes robust to variations inside and around the OD.

Yin et al. [32] used active shape modeling to identify the OD shape by 24 landmark points around the OD boundary. Each pair of adjacent points forms an angle of 15 degrees with the OD center. The landmark shape vectors were aligned to each other by rotation, scaling, and translation until the training set was completely aligned. Then, the knowledge-based circular Hough transform estimates the circle that best fits the OD within the specified OD diameter range. They claim that it outperforms the level-set and fuzzy c-means clustering methods.

2.1.4 Clustering-based techniques

The clustering-based approach groups a cluster with similar pixels based on color similarity. The grouped clusters are merged with one of their similar neighboring clusters until the specified number of iterations is reached. Rehman et al. [33] proposed an OD classification method using a linear iterative clustering technique based on OD segmentation. The technique segments the image into superpixels based on their spatial and intensity-based distances. Next, the intensity-based statistical features, textures, and fractal features are extracted from each superpixel. A support vector machine (SVM) classifier is used to classify a superpixel as the OD. The clustering-based approach cannot recognize the OD boundary when the OD is pale and has an invisible edge merged with the background or when the image includes larger exudates than the OD.

2.1.5 Component-based techniques

The component-based approach extracts the required region based on the intensity, shape, and size. Gui et al. [34] employed Harris corner detection to capture the OD location as the window with the maximum number of corner points. Wavelets, mathematical morphology, and Hessian-based multi-scale filtering were used in the OD segmentation method of Rodrigues et al. [35]. Their approach works on the deformability of the OD but ignores the fact that the OD has a shattered boundary due to vessels emerging from inside the OD. Sopharak et al. [36] utilized a median and a contrast-limited adaptive histogram equalization (CLAHE) filter on the intensity image. The method calculates the entropy value for each pixel in a local region.

The location with the highest entropy value is the OD candidate. The firefly algorithm by Rahebi et al. [37] uses the differences in the light intensities to calculate the rate of attraction, which governs the movements of the fireflies towards the OD. Abed et al. [38] compare several AI techniques, i.e., an artificial bee colony, particle swarm optimization, a bat algorithm, a cuckoo search, and firefly optimization. Their experiments showed that the fireflies produced the best accuracy under certain conditions. Lu proposed one of the most successful component-based algorithms [39]. Lu employed the modified circular transform method (CTM) and the evaluation of brightness. The process was tested against many state-of-art methods and claimed to be more accurate, efficient, and faster. However, the component-based approaches fail to localize the OD when the physical appearance of the OD (shape, color, brightness, or size) becomes abnormal. The OD, obscured by blood vessels or only partially visible (blur, shadows, noise), is often misclassified. In addition, the approaches may not be practical if the pathological features (such as lesions) appear in the image or the quality of the image is not sufficiently good.

2.1.6 Vessel-based techniques

Methods that emphasize the structure of vessels are categorized as a vessel-based approach. The vascular network is an essential feature for OD detection. The fuzzy convergence (FC) technique, proposed by Hoover and Goldbaum [9], creates fuzzy segments of the vessels to provide the points of strongest intersection. The illumination equalization technique is combined with the FC to minimize the large intensity variation at different scales. Then, the FC algorithm generates an image in which a pixel's brightness indicates the presence of the OD. To detect the OD location, Youssif et al. [40] proposed the vessels' directional-matched filter to match the direction of the vessels surrounding the OD. The vessel direction map was created by matching the structure of the vessels with a template at different scales. The OD center is the pixel having the least accumulated difference. The vessel-based approaches offer outstanding performance for images with good quality and prominent vessels; however, their computing time is impractically high.

OD detection based on the projection of the blood vessel intensities was proposed by Mahfouz and Fahmy [41]. It is an ultrafast algorithm. Therefore, it is a good candidate when speed is a concern. The method assumes that the area around the OD contains many vertical vessels and only a few horizontal vessels. Hence, it maps a 2-D image onto two 1-D signals representing the number of vessel pixels in the horizontal and vertical directions. The OD location is where the most significant difference in the number of vessels in the vertical and horizontal directions occurs. Since the method is simple, it localizes the OD within less than a second per image with an average accuracy of 97%. From our observation, it works well when the main vessel structure is approximately a parabola. However, an incomplete vessel structure may result in incorrect locations.

2.1.7 Hybrid techniques

A hybrid approach applies a combination of more than one approach. Lalonde et al. [42] used a Canny edge detector to find the OD edge information and a Hausdorff-based template matching to fit the OD rim by a circle. Abdullah et al. [43] presented a hybrid OD segmentation method composed of fuzzy-means clustering and the active contour model, followed by the ellipse fitting approach. Thakur et al. [44] combined a clustering approach and the level-set model for segmenting OD. Their method applies to cluster using the adaptively regularized kernel-based fuzzy c-means. The level-set model is used to segment the final contour. Khan et al. [45] localized the OD by morphological operations, using the disc-structuring element, and segmented the boundary by combining adaptive thresholding and region growing.

Muangnak et al. [46] presented an OD segmentation method that arranges the major vessels into clusters. The shortest distance to those clusters characterizes each point of the image. The operation is called the vessel transform (VT). The VT is considered a supplementary feature to detect the OD. The algorithm is integrated into the scale-space analysis [47] so that the vessel transform is applied on several resolution levels. They also provided an improved hybrid OD detection algorithm employing vessel vector-based phase portrait analysis (VVPPA) [48]. The hybrid method reported high localization accuracies of up to 98.87%. The VVPPA is a computationally heavy method, however. A tradeoff between speed and accuracy is typical for most algorithms.

Only a few works done for OD segmentation use retinal images acquired from a mobile camera. Besenczi et al. [49] presented an automatic OD and optic cup detection in retinal images taken by a handheld camera. They combined the works of Lalonde et al. [42] and Sopharak et al. [36] as a hybrid OD localization method. Each of these OD localization methods finds the center of the OD. Initial OD areas are obtained by extending the OD center into a circle. The OD areas' intersection is used to initialize the level-set method. They tested using a local dataset containing 48 mobile camera images. However, they did not show the accuracy of OD detection. It is essential to design fast and accurate methods applicable in a real clinical environment.

Our proposed OD localization method (HLM) is a hybrid approach based on an analysis of the vessel structure. It is derived from a general observation that the main vessel structure in the retinal image usually has a parabolic shape. However, vessels may also appear as a line or a half-parabola due to the camera's orientation while taking a picture, the imperfection of the imaging device, or insufficient patient cooperation. The HLM adaptably localizes the OD from the above vascular network patterns. It uses two different localization techniques to handle each pattern. The OD location result of the HLM is used as the initial point of a segmentation method. The details of our proposed OD detection and segmentation are presented in Chapter 3. The proposed algorithm has been tested using three mobile camera datasets and several datasets acquired from standard equipment. The information on datasets used in this study and the experimental results are provided in Chapter 4.

2.2 Optic disc edema segmentation

Another application of the OD analysis is the assessment of optic disc edema (ODE), an ophthalmoscopic finding characterized by unilateral or bilateral swelling of the optic disc (OD). There are a wide variety of conditions that cause ODE, such as papilledema (swelling secondary to raised intracranial pressure), papillitis (inflammation of OD caused by demyelination), pseudo papilledema (optic disc drusen), and diabetic papillopathy (swelling due to vessel leakage in the retina and axonal edema near the OD region) [50]. In general, ODE may present with blurring the OD margin, disc hyperemia, elevation of OD, peripapillary hemorrhage, and venous engorgement (tortuosity of retinal veins). Patients with ODE may suffer a range of symptoms depending on the underlying causes. Urfalioglu et al. [51] suggested that the presence of ODE should be evaluated to be able to avoid possible blindness and increase visual acuity in patients with symptoms of vision loss and elevated intracranial pressure. If left undetected at an early stage, it can lead to serious eye problems and life-threatening visual impairment. Figure 2.1 shows retinal images of a normal eye and an eye with ODE.

Automatic classification of the ODE stage, determining causes of ODE, and ODE detection through fundus images are subjective in the field of computer-aided diagnosis in ophthalmology. Akbar et al. [52] presented a decision support system for detecting papilledema and grading the stages if papilledema is suspected. The system applied the support vector machine classifier along with radial basic function kernel to perform detection and grading based on the extracted texture features from the gray-level co-occurrence matrix, features from the disc margin obscuration, and color features from the OD region, and features from the segmented vascular structures. Saba et al. [53] implemented a deep learning model composed of Dense-Net (an architecture with five dense blocks that takes cropped images containing the OD region) for classifying normal and papilledema images, and U-Net, for extracting the vessel network. Then, grading the severity of papilledema images was performed based on the vessel discontinuity index and the vessel discontinuity index to disc proximity. Liu et al. [54] confirmed that the ODE area is a reliable index in the diagnosis of POEMS syndrome, of which ODE plays an important ocular manifestation. In addition, ODE segmentation is essential for evaluating the ODE severity in other neuro-ophthalmic diseases.

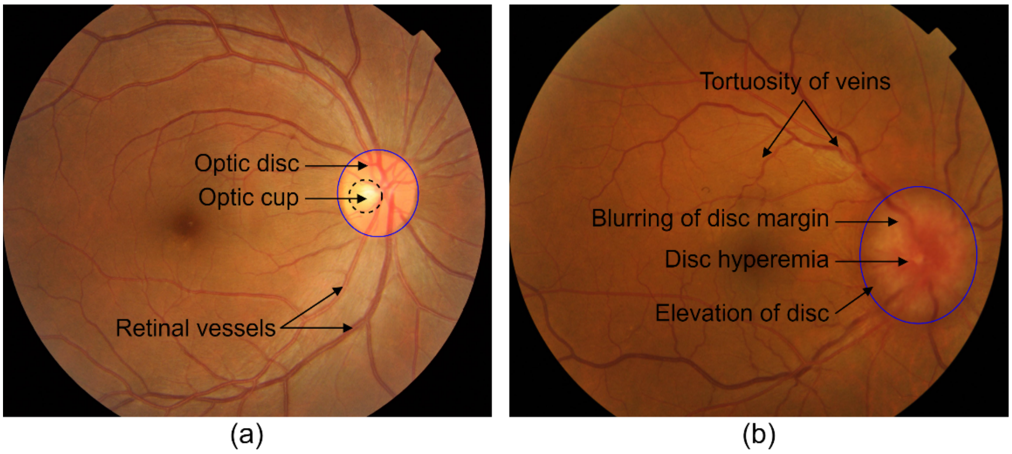

Figure 2.1 Retinal images of a normal eye (a) and an eye with ODE (b).

To localize an initial location of OD/ODE, the above papilledema classification and grading systems [52][53] applied a localization method [55] that identifies the OD location as the bright region(s) after enhancing the image using Laplacian of Gaussian kernel. If there is more than one bright region, the OD is defined as the region with the highest vessel density in the extracted vessel image. Then, an OD segmentation method based on the ellipse fitting approach [56] was applied to segment the OD boundary roughly. The images were cropped centered at the segmented OD and were fed to the systems for feature extraction. Since their ultimate goal is to classify papilledema, the accuracy and performance of OD/ODE localization and segmentation were not reported.

In our work, we apply HLM to detect a location in ODE. For ODE segmentation, we modify the active contour model based on the factorization of the image's texture feature. The details of the proposed ODE segmentation method, the datasets with ODE, and the experimental results are described in Chapters 3 and 4.

Chapter 3

Proposed methods for optic disc detection and segmentation in fundus images

Chapter 3 Proposed method for optic disc detection and segmentation in fundus images

This chapter presents the hybrid proposed OD localization and segmentation methods. Our proposed localization and segmentation method are based on an analysis of the vessel structure.

The HLM adaptably localizes the OD from the above vascular network patterns. The input image is initially converted to a grayscale image of the green channel (see Figure 3.2 (a)). Otsu's method [57], combined with the top-hat transformation, is applied to obtain a binary vessel image. The morphological top-hat filtering is utilized with the cross-shaped structuring element of which the size is the maximum thickness of the vessels extracted from the vessel image (see Figure 3.2 (b)). Then, we extract the two thickest vessels (see Figure 3.2 (c)). HLM uses two different localization techniques to handle each pattern. If the extracted vessels fit a parabola, HLM applies the exclusion method (EM) [58]. Otherwise, HLM applies a line detection method (LDM) alternatively. Thus, we obtain candidates of OD locations using either the EM or LDM. After detecting multiple OD locations, we extract the features of the vessels in circular regions centered at the OD location candidates. By learning the extracted features, a decision tree is used to decide the final OD location. Finally, an active contour (AC) model followed by circle fitting (CF) is used to segment the OD boundary using the detected OD location. HLM-ACCF denotes the entire localization-segmentation procedure. The details of each step are described in the following subsections. The overall framework of OD localization and segmentation is presented in Figure 3.1.

3.1 Optic disc detection

First, we analyze the vessel structure by calculating the orientations of the two extracted main vessels. The directions of the two vessels are determined based on the moment of inertia. The principle is to estimate an equivalent ellipse centered at the vessel's centroid. The moment (M_{pq}) of the vessel (V) is defined as follows.

$$M_{pq} = \sum_{i,j \in V} i^p j^q \tag{3.1}$$

Using the first-order moments (M_{10}, M_{01}) and the vessel area (a), the coordinates $(\bar{x}, \bar{y})$ of the centroid of a vessel are given by

$$\bar{x} = \frac{M_{10}}{a}\ ,\ \bar{y} = \frac{M_{01}}{a} \tag{3.2}$$

Then, the inertia matrix of a vessel, $\begin{bmatrix}\mu_{20} & \mu_{11}\\ \mu_{11} & \mu_{02}\end{bmatrix}$, is obtained by using the second-order central moments, $\mu_{20} = \frac{M_{20}}{a} - (\bar{x})^2$, $\mu_{11} = \frac{M_{11}}{a} - \bar{x}\bar{y}$ and $\mu_{02} = \frac{M_{02}}{a} - (\bar{y})^2$. The inertia matrix's eigenvectors correspond to the ellipse's major and minor axes. The orientation (θ) is given by

$$\theta = \frac{1}{2} tan^{-1}\left(\frac{2\times\mu_{11}}{\mu_{20}-\mu_{02}}\right) \tag{3.3}$$

θ represents the angle between the horizontal axis and the ellipse's major axis. Figure 3.2(d) shows the vessels with the corresponding ellipses and their axes and orientations.

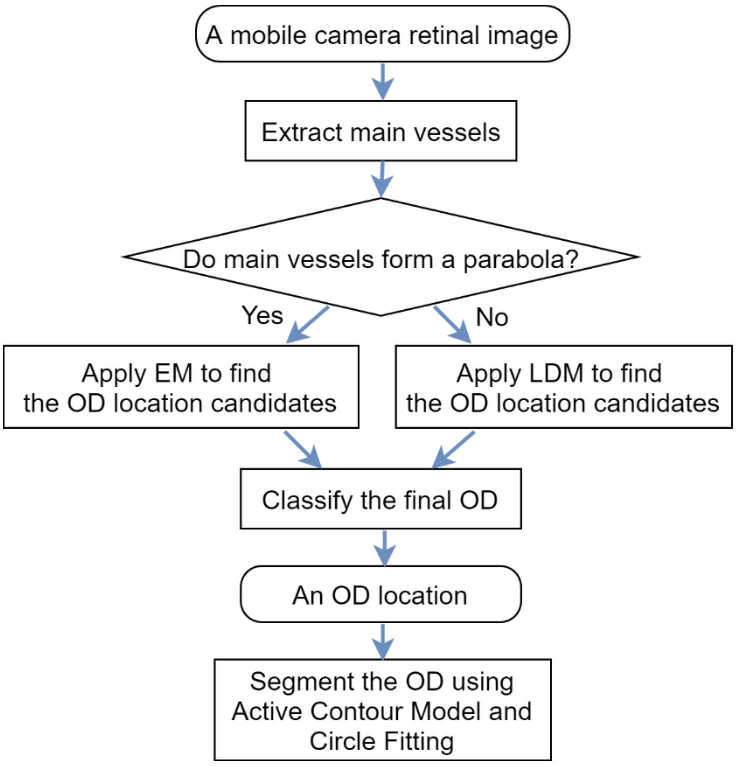

Figure 3.1 The hybrid framework for localizing and segmenting the OD.

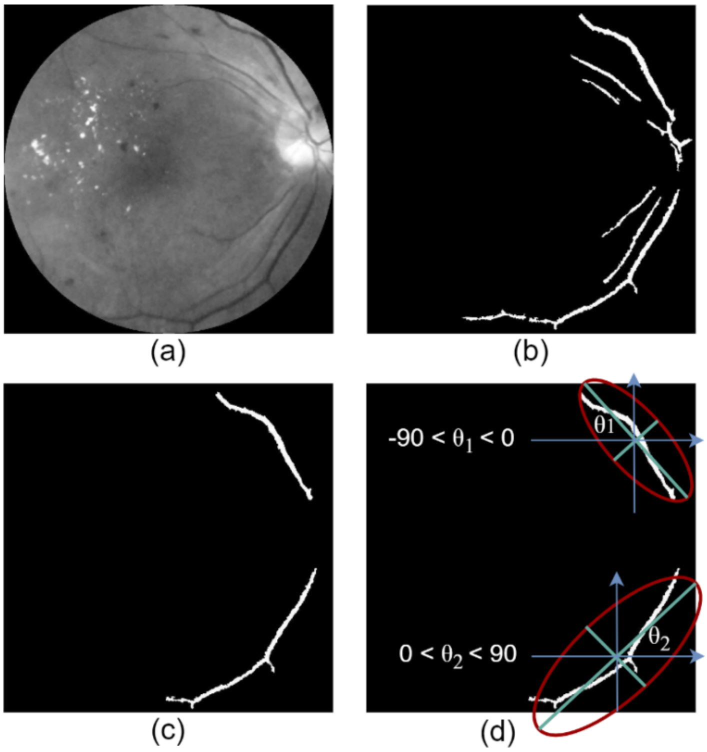

Figure 3.2 Analysis of the vessel structure; (a) a retinal image, (b) vessel image of (a), (c) extracted main vessels, and (d) analyzing the form of vessels.

If the orientation values have opposite signs, we consider that the vascular structure is parabola-shaped and apply the EM to find multiple OD locations. If both orientations have the same sign, we use the LDM. The EM relies on the assumption that the main vessels in the vascular network approximate a horizontal parabola. The extremum of the parabola is the location of the OD. Moreover, there are significantly fewer vessels oriented horizontally than vertically at this location. For non-parabola vascular networks, the EM's assumptions are not correct. For those cases, we apply the newly proposed LDM. The LDM uses the OD as a bright area where the blood vessels converge. The details of EM and LDM are described in Sections 3.1.1 and 3.1.2, respectively.

3.1.1 Exclusion method (EM)

The morphological opening operation is employed using a line structuring element to create horizontal and vertical vessel images characterized by the skeletons of the vascular network (see Figure 3.3 (c) and (d)).

Mahfouz and Fahmy [41] supposed that the area inside or surrounding the OD has a low count of horizontal and a high count of vertical vessels. Inspired by that idea, EM calculates a set of y locations in which the number of horizontal vessels is less than the average. Given an input image of width m and height n pixels, let y be the y location in the image and $HV(y)$ be the function of y representing the number of pixels in the horizontal vessel image at a y-location. The formula for calculating a set of a set of the y-locations is as follows.

$$Y_{loc} = \left\{ y \,\middle|\, HV(y) < \frac{1}{n}\sum_{y=1}^{n} HV(y) \right\} \tag{3.4}$$

We consider regions across the image at Y_{loc}. The adjacent regions are then grouped and called the horizontal region of interest (*HROI*). An OD candidate is calculated from each $HROI$. The y location of an OD candidate is at the middle of the HROI. The x location is where the number of the vertical vessels in the HROI is the largest. Figure 3.3 illustrates how the EM finds candidates for the OD.

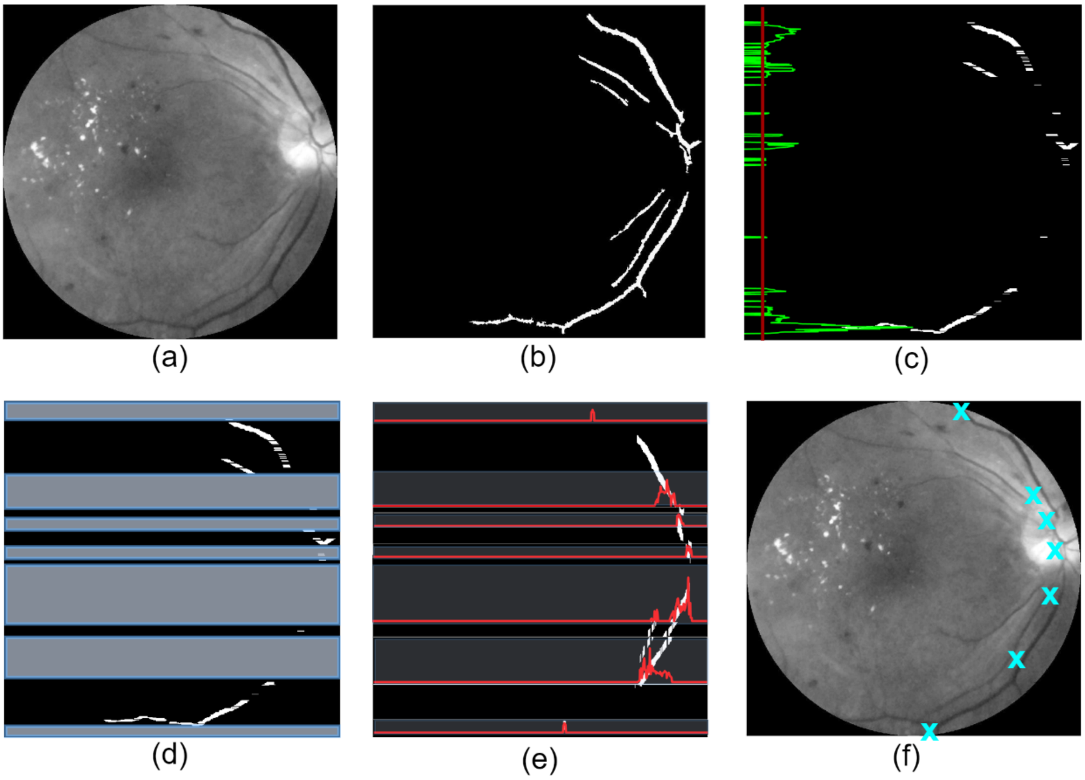

Figure 3.3 EM procedure; (a) retinal image with a parabolic vascular network, (b) vessel image of (a), (c) horizontal vessels with a graph showing the number of horizontal vessels (green line) at different y's and their average (red line), (d) HROI blocks that have the number of horizontal vessels lower than average (shown in grey), (e) vertical vessels with graphs showing the number of vertical vessels (red line) in each HROI, and (f) OD candidates (shown as X) from HROIs.

By considering the two 1-D signals used separately, EM increases the chance of getting a correct OD location. It can perform well even if the OD deteriorates since it depends less on the OD appearance than on retinal vessels.

3.1.2 Line detection method (LDM)

Line detection over the extracted main vessels is done using the Hough transform. The Hesse normal form (shown below) is used in the Hough transform to detect the lines as in the works of Duan et al. [59] and Duda and Hart [60].

$$\rho = x \cdot cos\theta + y \cdot sin\theta \tag{3.5}$$

where x and y denote the coordinates of a point on a line. The Hough space consists of two dimensions (ρ and θ). The ρ and θ are the distance from the line to the origin and the angle of the line to the x-axis, respectively. All detected lines are represented in this form when $\rho \geqslant 0$ and $\theta \in [0, 360]$. Each line in the x-y plane corresponds to a unique point in the ρ-θ plane. Figure 3.4 illustrates the transformation. The Hough transform algorithm detects the lines by finding intersections of the Hough lines.

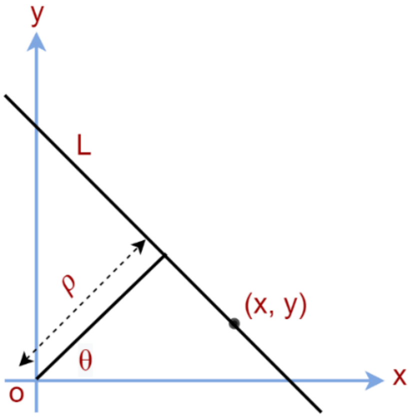

Figure 3.4 Mapping of a line to a point in Hough space.

To detect the OD, the LDM creates a square searching window, sized approximately one-sixth the width of the retina, centered at the detected lines. The window size is chosen according to the experimental relationship by Hoover and Goldbaum [9]. The average pixel intensity is calculated inside the search window across the line. For each line, the center of the region with maximum average intensity value is assumed to be an OD location. Figure 3.5 illustrates the approach.

3.1.3 Classification of the final OD location

The automatic decision tree, available from the Waikato Environment for Knowledge Analysis implemented by Hall et al. [61], is constructed to classify the OD location among multiple candidates. Each OD-location candidate is expanded into a circular region where the radius equals one-twelfth of the width of the retina. The number of vessels (NV), the area of vessels (AV), the vessel thickness (VTh), and the brightness (B) are used as the features for the decision tree. A 70/30 ratio was used for training and testing. After the classification process, we select the OD location with a higher number of vertical vessels if there is more than one OD location.

All retinal image datasets used in our experiment are collected from different devices with different FOV, angle, aspect ratio, and quality. Thus, different decision trees are constructed for each dataset. The decision tree of the STARE dataset in Figure 3.6 exemplifies the algorithm.

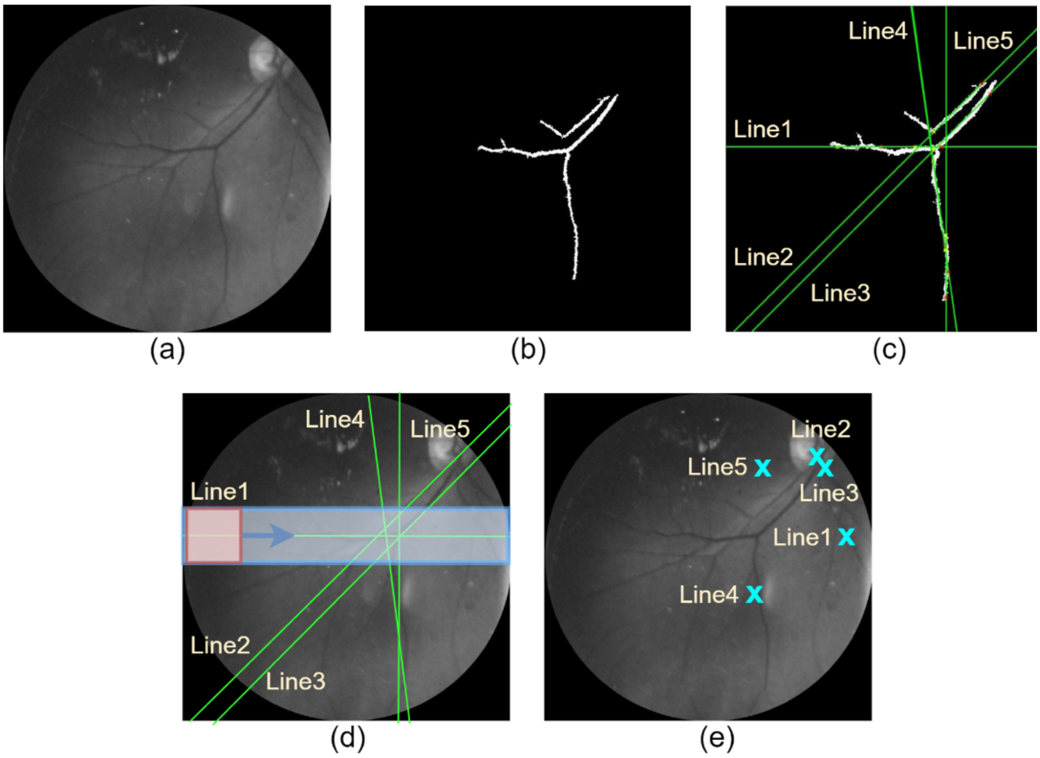

Figure 3.5 LDM procedure; (a) retinal image with a non-parabolic vascular network, (b) vessel image of (a), (c) Vessel image with detected Hough lines, (d) calculating average intensity inside the red search window across blue search space (for Line1 as an example), and (e) OD candidates (shown as X) for each line.

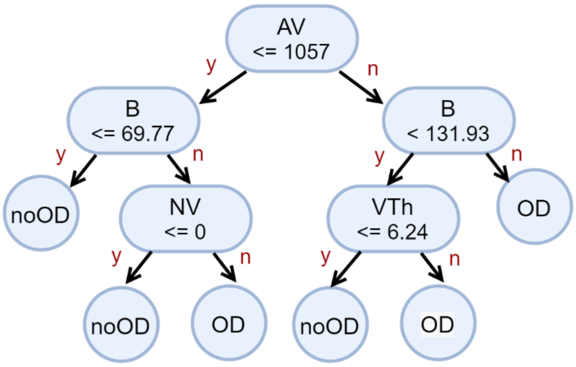

Figure 3.6 Decision tree for OD classification (STARE dataset).

3.2 Optic disc segmentation

To segment the OD, we first narrow the search space from the whole image to a region of interest (ROI) inside the square centered at the OD location (obtained from the HLM method). Using the ROI helps to reduce the computing time and to avoid abnormalities in the retinal image. For the ROP dataset, the size of the OD is usually smaller than in the other datasets because it was collected from infants. Thus, the estimated OD diameter is one-twelfth of the retina's width. The ROI size for the ROP dataset is set to be one-sixth of the image's width, while it is set to be one-third of the image's width for the other datasets. If the OD exists close to the rim, the ROI is a quarter of a circle. Figure 3.7 shows examples of ROIs.

For OD segmentation, we use the red channel of the ROI to obtain less interference of vessels and the highest inequality between the OD area and the background. The framework of HLM-ACCF is shown in Figure 3.8.

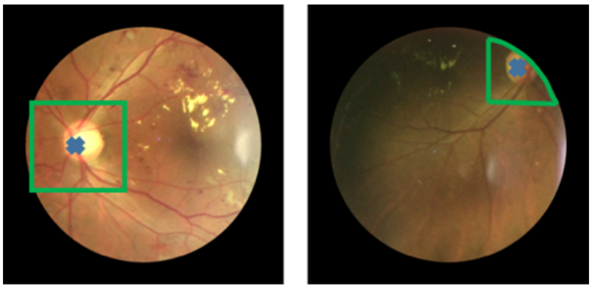

Figure 3.7 Creating ROI image; ROI when the OD location is not close to the rim (left) and ROI when the OD location is close to the edge (right).

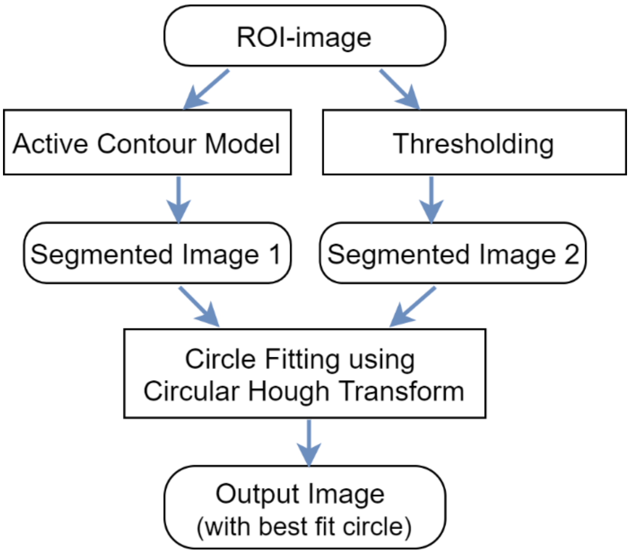

Figure 3.8 Framework of the HLM-ACCF for segmenting the OD.

The proposed HLM-ACCF identifies the OD boundary based on the active contour model and thresholding. Although the active contour model can detect an OD with weak and discontinuous edges, sometimes the model is affected by artifacts acquired while taking images by a handheld camera. Thus, the artifacts decrease the contrast between the background and the OD. To better determine the accurate OD boundary, we perform a simple thresholding step using the pixel intensity value of the OD location obtained from the HLM.

Active contour model

We apply the variational active contour model proposed by Chan and Vese [62] to detect the OD boundary. For an initial contour, we create a window of 100 × 100 pixels for the mobile camera datasets, DIARETDB0 and DIARETDB1, and 30 × 30 pixels for the STARE and ROP datasets, centered at the OD location from the HLM. Let Ω be a bounded set of $\mathbb{R}^2$, u_0 the ROI-image, C the parametrized curve, and $|C|$ the length of the curve C. To find the contour of OD, the model minimizes the energy functional F, defined by

$$F(c_1, c_2, C) = \mu\,|C| + \lambda_1 \iint_{inside(C)} (u_0(\mathrm{x,y}) - c_1)^2 dxdy + \lambda_2 \iint_{outside(C)} (u_0(\mathrm{x,y}) - c_2)^2 dxdy \tag{3.6}$$

where $\mu \geq 0$ and $\lambda_1, \lambda_2 > 0$ are weighting parameters and c_1, c_2 is the average pixel intensity inside and outside C given by

$$c_1(\Phi\,) = \frac{\iint_{\Omega} u_0(\mathrm{x,y}) H(\Phi(\mathrm{x,y}))dxdy}{\iint_{\Omega} H(\Phi(\mathrm{x,y}))dxdy} \tag{3.7}$$

$$c_2(\Phi\,) = \frac{\iint_{\Omega} u_0(\mathrm{x,y})\left(1 - H(\Phi(\mathrm{x,y}))\right)dxdy}{\iint_{\Omega}\left(1 - H(\Phi(\mathrm{x,y}))\right)dxdy} \tag{3.8}$$

The curve C is defined by $\{(x, y) \mid \Phi(\mathrm{x,y}) = 0\}$ where $\Phi(\mathrm{x,y})$ is the signed distance function. H is the Heaviside function, defined by

$$H(\Phi) = \begin{cases} 1, if\ \Phi \geq 0 \\ 0, if\ \Phi < 0 \end{cases} \tag{3.9}$$

We find experimentally that $\mu = 0.01$ and $\lambda_1 = \lambda_2 = 1$.

Circle Fitting using Hough Transform

The OD boundaries from the active contour model and thresholding appear in irregular shapes with an uneven edge. To provide smooth and round contours, we fit the OD boundaries with circles.

We adopt the circle fitting approach, implemented by Duda and Hart [60] and Kimme et al. [63]. Their approach transforms a set of feature points in the image space into a set of accumulator votes in the parameter space. The array of elements that have the highest number of votes indicates the presence of circular shapes.

The circle fitting approach produces two circular OD contours, together with the fitting scores. The fitting score specifies the point-by-point matching degree between the estimated circumference and the fitted shape in the image. A higher score indicates better OD boundary extraction and produces better segmentation quality. Thus, we select the circle with the higher fitting score as the OD region. The segmentation process performed by HLM-ACCF is illustrated in Figure 3.9.

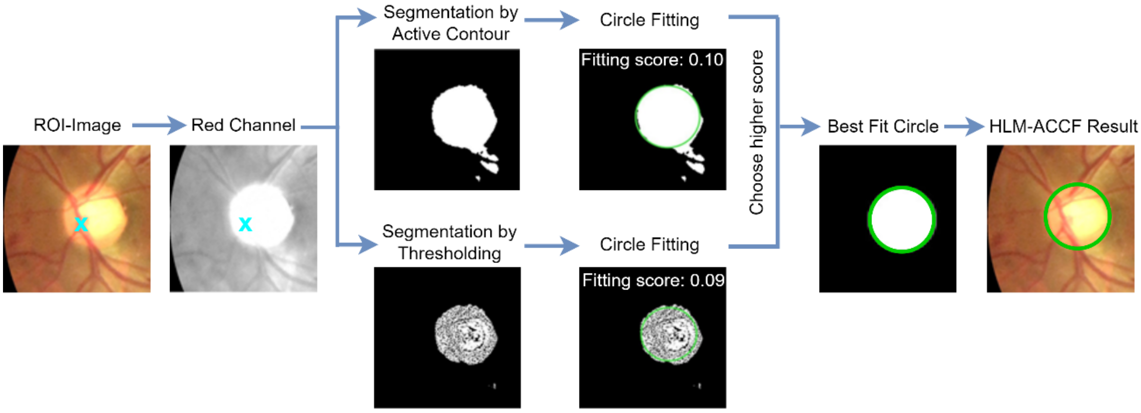

Figure 3.9 Segmentation process performed by the HLM-ACCF.

3.3 Optic disc edema segmentation

The HLM-ACCF method does not provide a good result if the images have a swelling OD or ODE since the neighboring pixels in the swelling area have as same intensity as the OD. When an OD swells, its texture appears featureless compared to a normal one [64]. The texture is an essential feature in images with ODE. For instance, all papilledema grading systems utilize texture information in the classification process.

For this purpose, we propose an ODE segmentation method based on image texture. The proposed method applies HLM to detect a location in the ODE area and segments the ODE boundary using a factorization-based active contour model (FAC). Centered at the OD location given by HLM, the input image is cropped into a sub-image of which the size is reduced by half. The image is converted from RGB to LAB color. It is then enhanced using adaptive histogram thresholding followed by vessel removal. The enhancement process is illustrated in Figure 3.10.

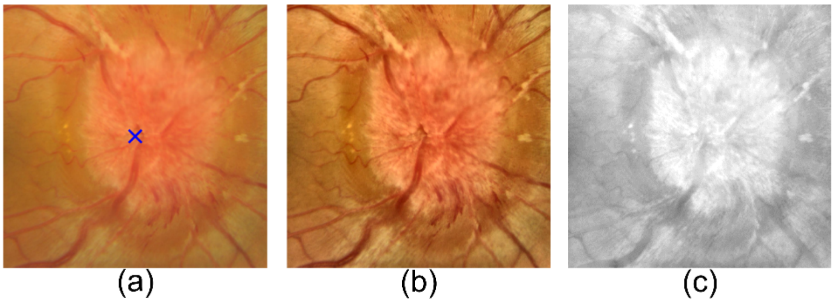

Figure 3.10 Pre-processed images, (a) after cropping, (b) after enhancement, and (c) after vessel removal.

To segment the ODE area, HLM is integrated with FAC proposed by Gao et al. [65]. The HLM's OD location is extended into the circle to create an initial contour. The energy of the FAC model (E_{FAC}) is composed of factorization-based fitting energy (E_{data}) and a regularization term which derives from a level set function, $\nabla_{\emptyset}(x)$.

$$E_{FAC} = E_{data} + \int_{\Omega} \frac{1}{2}(|\nabla_{\emptyset}(x)| - 1)^2 dx \tag{3.10}$$

$$E_{data} = -\int_{\Omega}\left[H(\emptyset)\omega_o(x,R) + \left(1 - H(\emptyset)\omega_b(x,R)\right)\right] dx \tag{3.11}$$

$$\omega = [\omega_o,\ \omega_b] = (RR^T)^{-1}R^TY \tag{3.12}$$

where Ω denotes the weight of the pixel x, Y is the feature matrix calculated over the sub-image in which different kinds of texture feature maps are mixed to distinguish object and background effectively, and R is a feature matrix used in the FAC model to update new contour weights of object and background regions (ω_o, ω_b). The deformation process is repeated until the contour converges into the object boundary. Then, the segmented sub-image is converted into the original image's size. Figure 3.11 illustrates the segmentation process of FAC.

3.4 Measurement of optic disc area

The measurement of the OD area is usually performed after OD segmentation. Since the area of OD varies in various diseases, it is also an important step to analyze changes in the size of OD. The cup-to-disc area ratio is a widely used technique to diagnose glaucoma based on OD and OC segmentation results. The area of OD/ODE ($Area_{OD}$) can be simply calculated as the pixels occupied in the segmented image of OD/ODE (I_{OD_Seg}).

$$Area_{OD} = \sum_{i=1,j=1}^{n} I_{OD\_Seg}(i,j) \tag{3.13}$$

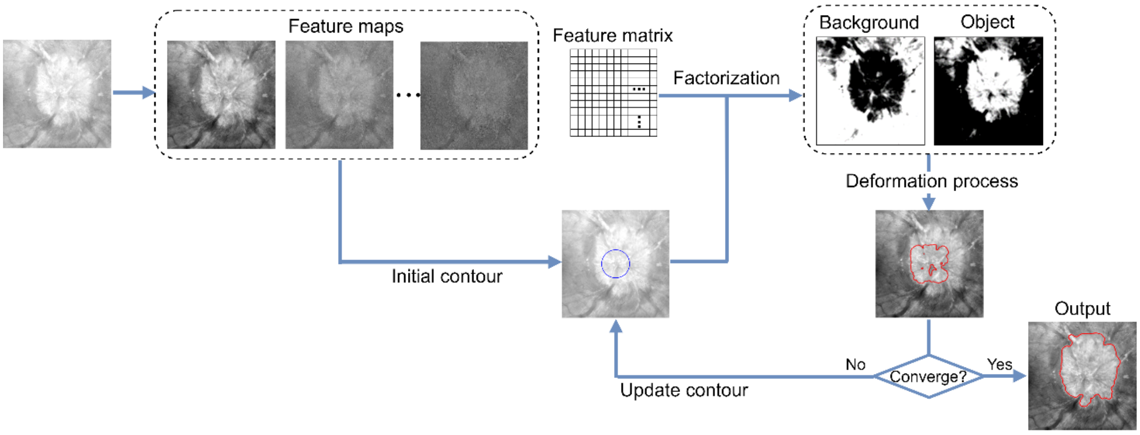

Figure 3.11 Segmentation process performed by the HLM-FAC.

Chapter 4

Experiments for optic disc detection and segmentation in fundus images

Chapter 4 Experiments for optic disc detection and segmentation in fundus images

This chapter presents the experiments of OD and ODE segmentation. Section 4.1 describes the datasets used in this work. The ground truth preparation process and evaluation metrics are described in Section 4.2. Section 4.3 presents the results obtained from these experiments.

4.1 Retinal fundus images

This section provides information on mobile-phone retinal image collections from Thammasat Eye Center of Thammasat University Hospital, Thailand. The details about the standard datasets and the ground truths annotations are also given.

4.1.1 Mobile-phone camera retinal datasets

Thammasat Eye Center [66] provides an inexpensive retinal imaging service using an iPhone 6s attached to a portable iNview lens from Volk [67] (see Figure 1.5 (b)) for patients at Thammasat University Hospital. After an imaging process, the images were automatically stored in Google Drive and further proceeded for other image processing steps. The signs of DR include the presence of exudates and hemorrhages in the retina. We include the normal images from the healthy retina to verify the robustness of our proposed methods. This study was approved by the National Medical Council of Thailand and has received an official ethical clearance. The details of mobile-phone datasets are summarized in Table 4.1.

Table 4.1 Descriptions of the mobile-phone camera retinal datasets

Dataset Name	Imaging Device	Description	No. of Images	Image Size (pixels)
Exudate	iPhone Fundus Camera	This dataset contains images with soft and hard exudates, which manifest yellow spots.	50	1,196×1,196
Hemorrhage		This dataset consists of images with hemorrhages, which manifest many red scattered splotches.	50	
Healthy		In this dataset, the images do not contain any sign of glaucoma and DR.	50	

As mentioned in Chapter 1, mobile camera retinal images have a narrower FOV with poorer quality than those of a standard slit lamp machine. Most images have artifacts such as pale blurring of the OD area, external light reflections, and incomplete vessel structures. For example, retinal images from each dataset are displayed in Figure 4.1 to show their characteristics.

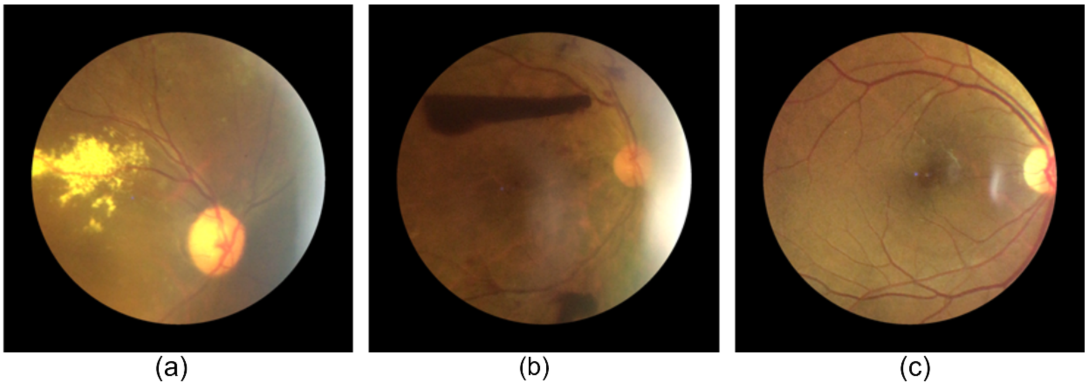
(a) (b) (c)

Figure 4.1 Examples of mobile-phone camera retinal images; (a) Exudate, (b) Hemorrhage, and (c) Healthy.

4.1.2 Standard retinal datasets

The four datasets (STARE, ROP, DIARETDB0, and DIARETDB1) were used for OD segmentation in DR cases. An ODE-related dataset was used for segmenting ODE areas in retinal fundus images. Most of them are publicly available. Example retinal images from standard datasets are shown in Figure 4.2.

STARE

The structured analysis of the retina (STARE) dataset [68] consists of 31 normal and 50 diseased images. The images (dimension of 700×605 pixels) were acquired from a TopCon TRV-50 Fundus Camera with a FOV of 35°.

Retinopathy of Prematurity (ROP)

The ROP dataset contains a total of 91 images. There are 31 poor images and 60 fair images. ROP occurs in premature infants born with undeveloped retinal vessels [70]. The images (dimension of 640×480 pixels) were captured using a KOWA-7 non-mydriatic Retinal Camera with 45° FOV at Kingston University of UK. The ROP dataset contains several images with abnormal vessel structures and a small OD. Thus, segmenting the OD in the ROP dataset is also challenging.

DIARETDB0

This public dataset [71] consists of 130 (dimension of 1500×1152 pixels), of which 110 contain signs of DR and 20 are normal. The objective of collecting this dataset is to detect DR from a digital fundus image. The images were collected using a standard fundus camera with calibration levels of 0 and 50° FOV.

DIARETDB1

DIARETDB1, with calibration level 1, is an extension of DIARETDB0 [72] and contains a total of 89 images, of which 84 have mild symptoms of DR and five are normal. The acquisition setting of this dataset is the same as DIARETDB0.

ODE

This dataset combines images from two sources. A set of 22 images with papilledema, pseudo-papilledema, and disc swelling due to local and systemic causes (dimension of 600×600 pixels) were obtained from a public source [72]. The details of the imaging setting are unknown. Another set of 13 images (dimension of 2300×1900 pixels) was obtained from the "Disc swelling and elevation" category in a publicly available dataset [73]. The images were acquired from a TopCon TRV-50 Fundus Camera and a ZEISS IR Fundus Camera with a FOV of 35-50°.

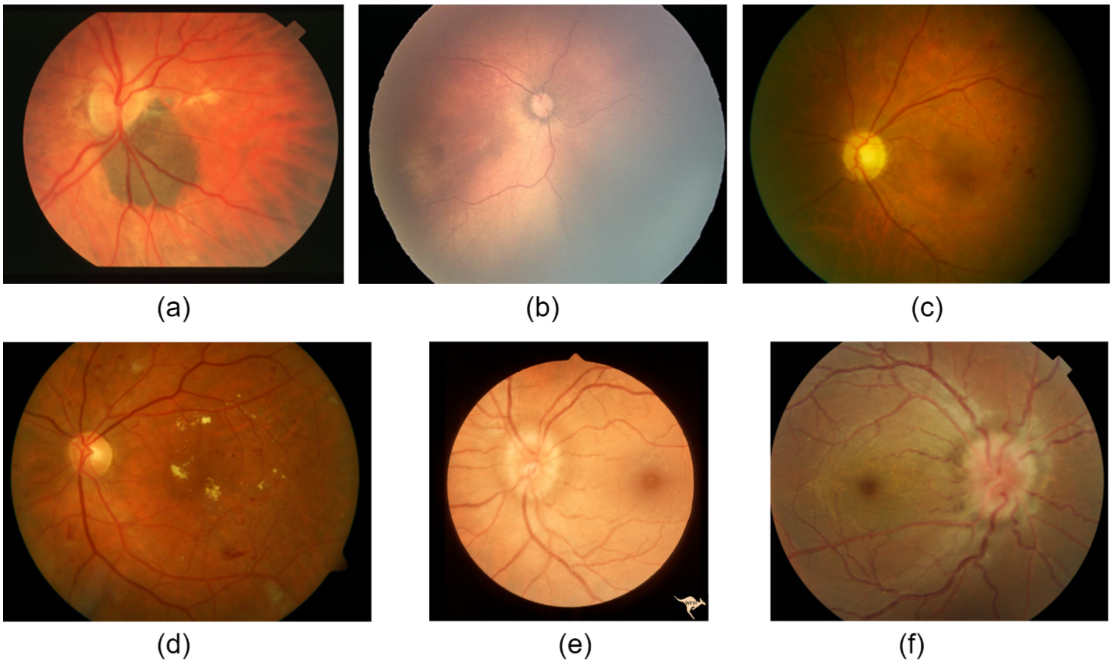
(a) (b) (c)

(d) (e) (f)

Figure 4.2 Examples of retinal images; (a) STARE, (b) ROP, (c) DIARETDB0, (d) DIARETDB1, (e) ODE1, and (f) ODE2.

4.2 Ground truth preparation and evaluation metrics

Hand-drawn annotations of OD and ODE are required to evaluate the performance of the proposed methods. The ground truths of the datasets: DIARETDB0 and DIRETDB1, are publicly available. We obtained manual annotations of OD (for mobile-phone camera datasets, STARE, and ROP) from the ophthalmologists of Thammasat University Hospital. An ophthalmologist from the Chiba University Hospital helped train the observer to be able to annotate the ground truths of images with ODE.

The OD localization and segmentation results of the proposed methods are evaluated using the corresponding ground truths. We consider that a localization method successfully detects the OD if the OD location from that method lies inside the ground truth contour.

The segmentation performance for the OD and OC was quantitatively evaluated by using three evaluation metrics, namely precision, recall, and F-measure. The formulas for these metrics are given in Equations 4.1, 4.2, and 4.3. Based on four possibilities, true-positive (TP), true-negative (TN), false-positive (FP), and false-negative (FN), the metrics were calculated. TP and TN indicate mutual agreement between the predicted OD and the actual OD, whereas FP and FN indicate incorrect predictions. A confusion between TP, TN, FP, and FN is illustrated in Figure 4.3.

$$\text{Precision} = \left(\frac{TP}{TP+FP}\right) \tag{4.1}$$

$$\text{Recall} = \left(\frac{TP}{TP+FN}\right) \tag{4.2}$$

$$\text{F-measure} = 2\times \left(\frac{precision \times recall}{precision + recall}\right) \tag{4.3}$$

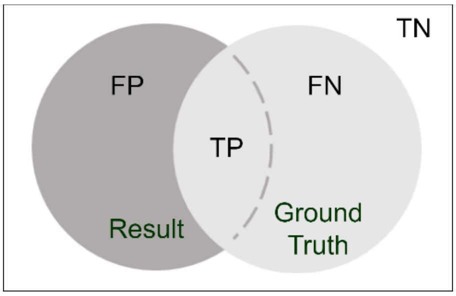

Figure 4.3 Illustration of a confusion for OD segmentation.

4.3 Experimental Results

The proposed method was tested on three datasets (Exudate, Hemorrhage, Healthy) obtained from a mobile camera and several standard datasets. HLM, HLM-ACCF, and HLM-FAC were implemented using Matlab (MathWorks, Inc.). The comparative studies of the proposed vessel-based hybrid localization and segmentation methods were performed against several state-of-the-art methods. The numerical results of the OD localization and OD and ODE segmentation are presented in Sections

4.3.1, 4.3.2, and 4.3.3, respectively.

4.3.1 Optic disc detection and segmentation

Figure 4.4 shows the qualitative results of the localizations performed by the HLM and some existing methods. Table 4.2 compares the performances of OD localization by the optimal thresholding method of Ruennark et al. [26], the vessel-based feature projection method of Mahfouz and Fahmy [41], EM, LDM, and the proposed HLM using three mobile camera datasets (Exudate, Hemorrhage, and Healthy). The proposed HLM had a success rate as high as 98% for Exudate, 96% for Hemorrhage, and 100% for Healthy. The average improvements of the proposed method over the optimal thresholding method, the feature projection method, EM, and LDM are 8.67%, 22.67%, 5.33%, and 3.33% for three mobile datasets, respectively.

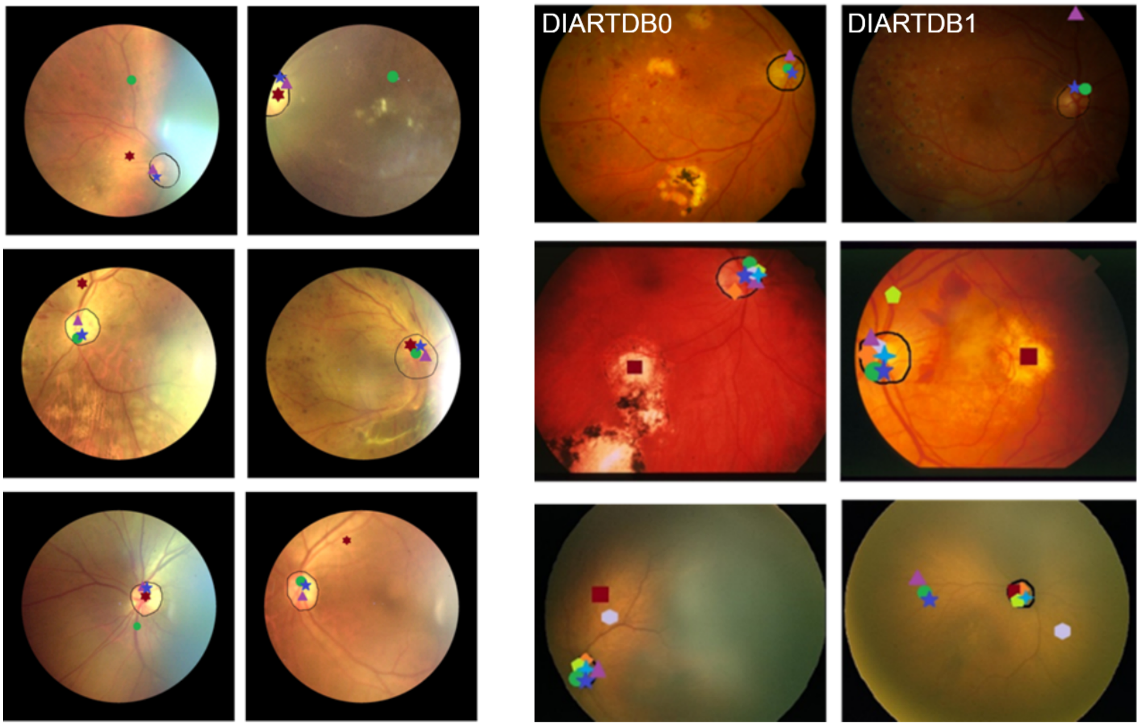

(a) (b)

Figure 4.4 Examples of OD localization results performed by FC, CTM, VT, VVPPA, Hybrid, EM, LDM, and HLM for each dataset, (a) for mobile-phone camera datasets: Exudate (top), Hemorrhage (middle), Healthy (bottom), and (b) standard datasets: DIARETDB0 (top left), DIRETDB1 (top right), STARE (middle), and ROP (bottom). Optimal thresholding - ✸ , FC - ◆ , CTM - ■ , VT - ⬟ , VVPPA - ⬢ , HM - ✦ , EM - ● , LDM - ▲ , HLM - ★ , and Ground truth contour - black solid line.

Table 4.2 Comparison of the OD localization accuracies for mobile camera datasets

Methods	Types of Approach	OD Localization Accuracy (%)		
		Exudate	Hemorrhage	Healthy
Optimal Thresholding	Thresholding	92.00	88.00	88.00
Feature Projection	Vessel-based	70.00	76.00	80.00
EM	Vessel-based	88.00	92.00	98.00
LDM	Vessel-based	92.00	94.00	98.00
HLM (Proposed)	Hybrid	**98.00**	**96.00**	**100.00**

Table 4.3 compares the performance of the OD localization of the methods described in Chapter 2 (which reported the localization performance in their works) and the proposed HLM, using the datasets acquired from standard equipment. For the STARE dataset, the CTM by Lu [39] and Youssif et al. [40] achieved the highest success rate of 98.77%. For the ROP dataset, the HM by Muangnak et al. [48] had the best accuracy of 98.87%. For DIARETDB0, Mahfouz and Fahmy [41] obtained the highest accuracy of 98.50%. For DIARETDB1, Esmaeili et al. [28], Abed et al. [38], and Abdullah et al. [43] claimed the best performance with 100% accuracy.

The proposed HLM-ACCF is a hybrid OD segmentation method designed to achieve efficiency in computing time, high accuracy, and robustness. In this section, the OD segmentation results performed by the HLM-ACCF are tested against several OD segmentation methods. A comparison of the methods for Exudate, Hemorrhage, and Healthy is shown in Table 4.4. Table 4.5 compares the results using the standard datasets. Examples of OD segmentation performed by the HLM-ACCF and the existing methods are illustrated in Figure 4.5.

The HLM-ACCF provides good performance for mobile camera datasets with 92.64% precision, 82.39% recall, and 87.17% of the F-measure, on average. The HLM-ACCF shows an improvement upon the EM-ACCF and LDM-ACCF by 4.33% and 5.1% for the average precision, by 2.22% and 6.42% for the average recall, and by 3.15% and 5.85% for the F-measure, respectively.

Table 4.5 shows that the HLM-ACCF outperforms the EM-ACCF and LDM-ACCF on the standard datasets. For the STARE and DIARETDB1 datasets, Abdullah et al. [43] deliver the best performance with the highest recall of 80.21% and 93.37%, respectively. The precision of the HLM-ACCF for the STARE dataset is close to the (highest) precision of 75.54% obtained by CTM of Lu [39].

Table 4.3 Comparison of the OD localization accuracies for standard datasets

Authors/ Methods	Types of Approach	OD Localization Accuracy (%)			
		STARE	ROP	DIARETDB0	DIARETDB1
Hoover et al. (2003)	Vessel-based	88.89			
Esmaeili et al. (2012)	Level-set	93.80			**100.00**
Rehman et al. (2019)	Clustering-based				
Gui et al. (2018)	Component-based	86.40			
Rahebi et al. (2016)	Component-based	95.00			94.38
Abed et al. (2016)	Component-based	95.00			**100.00**
CTM	Component-based	**98.77**	80.21		
Youssif et al. (2008)	Vessel-based	**98.77**			
Mahfouz et al. (2010)	Vessel-based	92.60		**98.50**	97.80
Abdullah et al. (2020)	Vessel-based	97.53			**100.00**
Khan et al. (2020)	Hybrid				
VT	Hybrid	95.06	95.60		
VVPPA	Vessel-based	97.53	94.50		
HM	Vessel-based	98.76	**98.87**		
EM	Hybrid	91.36	79.12	96.92	98.88
LDM	Vessel-based	81.48	85.71	95.38	96.63
HLM (Proposed)	Vessel-based	90.12	90.11	96.15	97.75

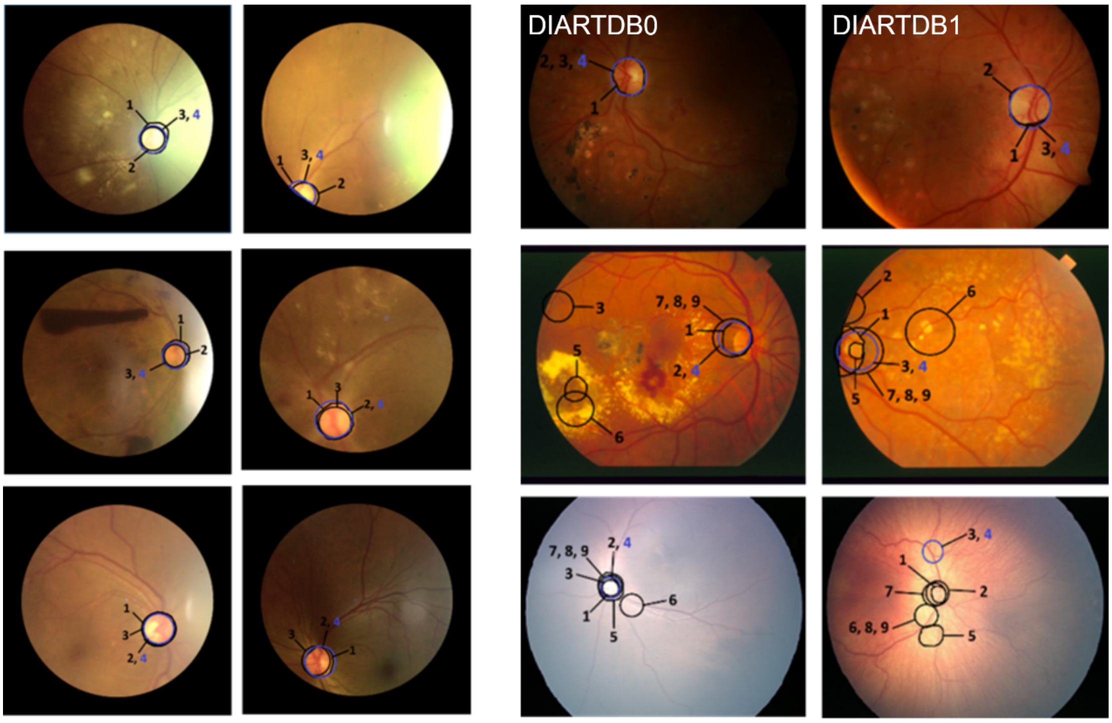

(a) (b)

Figure 4.5 Examples of OD segmentation results for each dataset, (a) for mobile-phone camera datasets: Exudate (top), Hemorrhage (middle), Healthy (bottom), and (b) standard datasets: DIARETDB0 (top left), DIRETDB1 (top right), STARE (middle), and ROP (bottom). **1**-Ground truth contour, **2**-EM-ACCF, **3**-LDM-ACCF, **4**-HLM-ACCF, **5**-CT, **6**-SS, **7**-SSVT, **8**-SSVVPPA, and **9**-SSHM.

Table 4.4 Comparison of the OD segmentation performance using mobile-phone camera datasets

Methods	Type of Approach	Dataset	Evaluation Metrics		
			Precision	Recall	F-measure
EM-ACCF	Vessel-based	Exudate	84.48	73.46	78.59
LDM-ACCF	Vessel-based		87.45	73.26	79.73
HLM-ACCF (Proposed)	Hybrid		94.10	80.23	86.61
EM-ACCF	Vessel-based	Hemorrhage	87.37	78.18	82.52
LDM-ACCF	Vessel-based		89.34	75.81	82.02
HLM-ACCF (Proposed)	Hybrid		91.09	79.08	84.66
EM-ACCF	Vessel-based	Healthy	93.09	88.87	90.93
LDM-ACCF	Vessel-based		85.84	78.83	82.19
HLM-ACCF (Proposed)	Hybrid		92.73	87.87	90.23

Table 4.5 Comparison of the OD segmentation performance using standard datasets

Authors/ Methods	Type of Approach	Dataset	Evaluation Metrics		
			Precision	Recall	F-measure
CTM	Component-based	STARE	75.54	53.23	
Abdullah et al. (2020)	Hybrid			80.21	88.01
SS	Component-based		62.21	48.89	
SSVT	Vessel-based		74.42	52.13	
SSVVPPA	Vessel-based		73.82	54.39	
SSHM	Hybrid		75.05	54.40	
EM-ACCF	Vessel-based		73.84	57.22	64.48
LDM-ACCF	Vessel-based		66.85	51.69	58.30
HLM-ACCF (Proposed)	Hybrid		75.16	59.13	66.19
CTM	Component-based	ROP	59.60	69.85	
SS			74.81	68.50	
SSVT	Vessel-based		86.20	74.20	
SSVVPPA	Vessel-based		83.08	73.24	
SSHM	Hybrid		86.20	74.20	
EM-ACCF	Vessel-based		58.11	52.81	55.33
LDM-ACCF	Vessel-based		69.98	61.21	65.30
HLM-ACCF (Proposed)	Hybrid		74.03	62.13	67.56
EM-ACCF	Vessel-based	DIARETDB0	88.29	77.54	82.57
LDM-ACCF	Vessel-based		87.89	77.37	82.30
HLM-ACCF (Proposed)	Hybrid		87.95	76.70	81.94
Abdullah et al. (2020)	Hybrid	DIARETDB1		86.21	87.10
Khan et al. (2020)	Hybrid			93.37	
EM-ACCF	Vessel-based		91.16	79.21	84.77
LDM-ACCF	Vessel-based		89.09	77.90	83.12
HLM-ACCF (Proposed)	Hybrid		91.11	78.33	84.24

4.3.2 Optic disc edema detection and segmentation

This section presents the qualitative and quantitative performance of ODE localization and segmentation. The proposed HLM obtained an average success rate of 97.14%. It successfully located the OD in 34 images out of 35. The feature projection method by Mahfouz and Fahmy [41] had 74.29%, whereas the optimal thresholding method of Ruennark et al. [26] had 77.14%. Figure 4.6 shows the localization results.

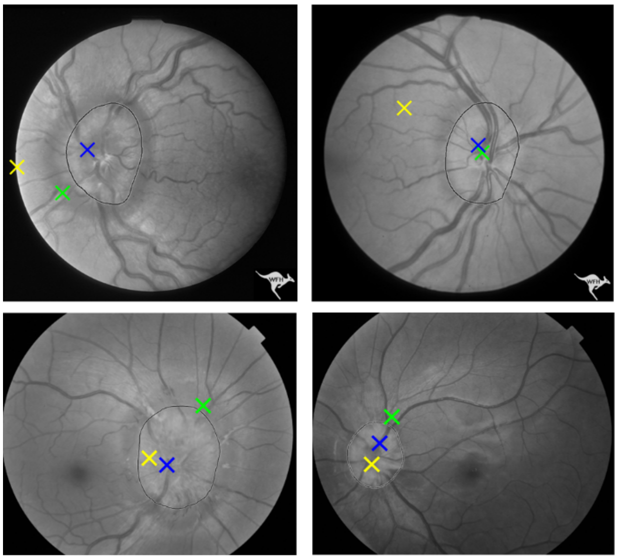

Figure 4.6 Examples of ODE locations from Feature Projection (×), Optimal Thresholding (×), and HLM (×).

Active contour (also called gradient Vector Flow (GVF) snakes) are extensively used for OD segmentation. A snake is defined by an energy function that is a sum of internal energy that controls the snake's elasticity and stiffness and the external energy that is image-gradient-based. Kusumandari et al. [74] compared the performance of GVF and ellipse fitting methods in OD detection and proved that GVF had better performance. In our previously proposed glaucoma screening, we have also applied adaptive deflation and inflation GVF (ADI-GVF), in which the balloon force is conditioned to enable the snake curve to perform deflation and inflation dynamically system [75]. A clustering method proposed by Wilson et al. [76] was included in comparing ODE segmentation against the proposed FAC model.

Tables 4.6 shows the comparisons of the numerical results for ODE segmentation. The proposed FAC model achieved the best F-measure of 84.24% and a precision of 91.74%. It generally outperformed the comparative methods: conventional GVF [74], ADI-GVF [75], and the clustering method [76] by 3.53%, 11.15%, and 11.04%, respectively. The region growing method [45] had the highest 85.42% of recall; however, it is inferior to the proposed HLM-FAC in terms of F-measure by 19.48% and precision by 40.66%. Figure 4.7 shows examples of ODE segmentation results. ADI-GVF and the proposed HLM-FAC produce more smooth contours compared to other methods. In ODE images, ADI-GVF cannot correctly perform its dynamic deformation process (deflation and inflation). Most methods suffer from over-segmentation since the ODE regions have blurry edges and low contrast between the ODE and the background.

Table 4.6 Comparison of the ODE segmentation performance

Authors/ Methods	Type of Approach	Dataset	Evaluation Metrics		
			Precision	Recall	F-measure
GVF	Active contour and active shape model	ODE	90.62	76.90	80.71
ADI-GVF			75.31	74.04	73.09
Region Growing	Component-based		50.58	**85.42**	64.48
Superpixel Clustering	Clustering-based		83.08	68.70	73.20
HLM-FAC (Proposed)	Hybrid		**91.74**	79.21	**84.24**

4.4 Summary and discussion

This work presents an automatic OD segmentation method (HLM-ACCF) specially designed for mobile camera retinal images of DR and normal eyes and an automatic ODE segmentation method (HLM-FAC) for images with swelling OD.

The HLM-ACCF has been evaluated using three mobile camera datasets (Exudate, Hemorrhage, Healthy), three standard datasets (STARE, DIARETDB0, DIARETDB1), and ROP (total of 541 images). The proposed HLM achieves an average localization accuracy of 98% for the three mobile camera datasets. The method shows an average precision of 92.64% and an average recall of 82.38% for OD segmentation. The performance of the proposed algorithms is comparable with the accuracy achieved by the state-of-the-art methods on standard datasets. The proposed method can also be applied as an initial processing step for detecting other components/abnormalities in the retina (such as exudates, fovea, or hemorrhages) which are essential in the analysis of DR.

However, the performance of the HLM-ACCF for the ROP dataset is lower than the well-performed VT-VVPPA Hybrid by Muangnak et al. [48] because there are many poor-condition images, resulting in 9.88% incorrect localization. Due to the unique characteristics of the ROP images, HLM incorrectly localized the ODs, and the segmentation results returned the wrong boundaries. Figure 4.8 (a) illustrates these experiments. Our proposed method fails to segment the OD when the OD boundaries are not well-defined. Figure 4.8 (b) shows the latter case.

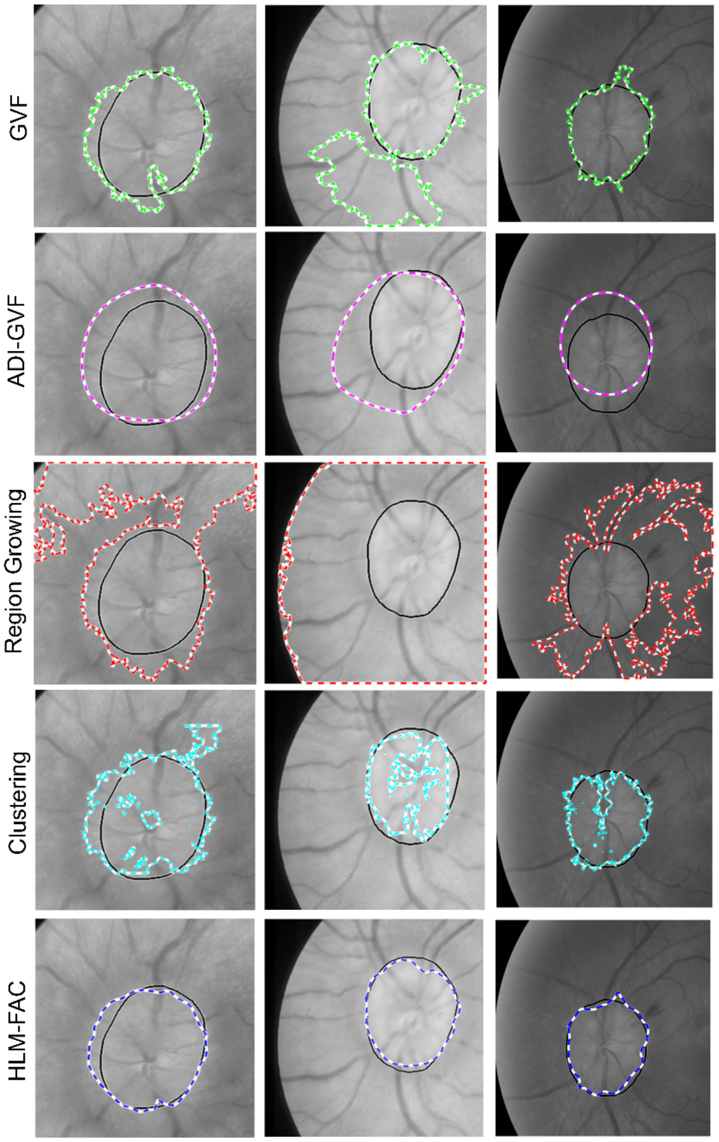

Figure 4.7 Examples of ODE segmentation from GVF, ADI-GVF, region growing, clustering method, HLM-FAC. (The ground truth contour is shown as the solid black contour.)

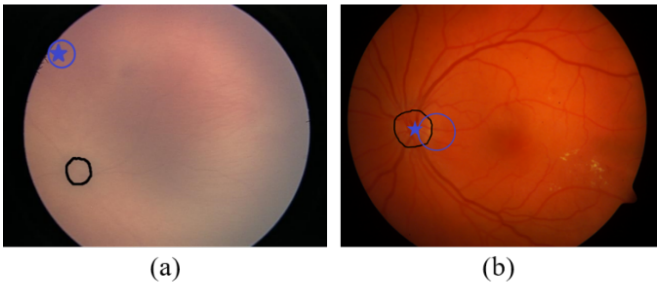
(a) (b)

Figure 4.8 Failure cases of HLM and HLM-ACCF; (a) image with the very faint vessels; (b) image with the invisible OD boundary.

The HLM-FAC has been evaluated using 35 images with ODE. It could correctly locate the OD in 34 out of 35 images (with a success rate of 97.14%) and segment ODE areas with the highest F-measure of 84.24%. Finding the ODE area is essential in the ODE severity grading process. With the performance of our proposed method, our work can be applied in an ODE grading/classification system to yield more precise results.

Nonetheless, the proposed method shows an inconclusive ODE localization and segmentation case. HLM applies the exclusion method for images with a complete vessel pattern. In Figure 4.9, the main vessels (the thickest vessels) are parabola-shaped. Thus, HLM chose EM to perform the localization process. There are many horizontal vessels at the left and right sides of the ODE area. EM excludes areas with high horizontal vessel density to find the candidate locations. Therefore, the location given by the proposed method was outside the actual OD region. To segment the ODE area, the proposed HLM-FAC used that location as a seed point to create an initial contour. The intersection between the initial contour and the actual contours is small. As a consequence, our method could not segment the whole ODE area.

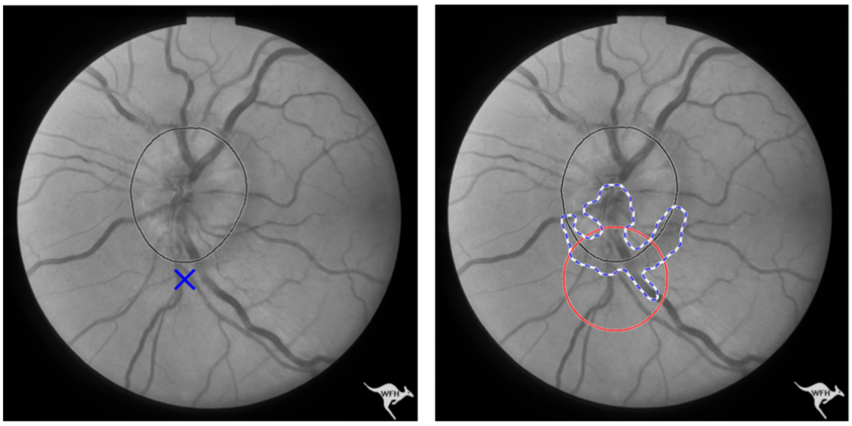
(a) (b)

Figure 4.9 Inconclusive cases of the proposed method; (a) incorrect locations from HLM (shown as ×), and (b) inaccurate segmentation of ODE area by HLM-FAC (shown in the blue dashed contour). The red circle indicates the initial contour centered at the incorrect location. The solid black contour indicates the ground truth.

Chapter 5

Related works of choroid layer and vessel segmentation

Chapter 5 Related works of choroid layer and vessel segmentation

This chapter briefly describes related works of choroid layer and vessel segmentation in retinal OCT images. All OCT images are centered at the fovea, optic nerve head, or OD. Most choroid layer segmentation mainly uses the foveal-centered (macular) OCT images as the choroid is the more significant and essential vascular supply at the fovea. Traditional image processing techniques were used to segment the choroid layer and vessels before the emergence of deep learning techniques. With the development of deep learning techniques, the complex problems in digital image processing such as image segmentation, object detection, and image classification could be better solved. Therefore, several deep learning models were recently developed for choroid segmentation to improve performance.

5.1 Choroid layer segmentation

Many traditional image processing methods have been proposed to segment the choroid layer fully or semi-automatically for various retinal diseases. The graph search, dynamic programming, and the Dijkstra algorithms are widely used in previous works.

Hu et al. [77] presented a multistage segmentation technique based on a graph searching approach to delineate junctions between the RPE and the choroid and between the choroid and the sclera. Danesh et al. [78] applied dynamic programming to detect RPE. Then, wavelet-based features were extracted to develop a gaussian mixture model for segmenting the choroid-sclera interface. Salafian et al. [79] proposed a technique of choroid segmentation in which the input image is transformed into a neutrosophic space that contains true, false, and indeterminacy sets. Then, the Dijkstra shortest path algorithm is applied to detect the choroid boundaries based on the calculated weights between every two nodes in the neutrosophic image. Wang et al. [80] segmented a choroid layer using the level set method in which a distance regularization term, an edge constraint term, and a region (around CSI) term are embedded to detect the indistinct CSI and to compensate for uneven textures in the choroid. The above methods were tested only for healthy subjects and may be highly sensitive to pathological images. Graph cuts [81], min-cut max-flow graph theory [82], other Dijkstra shortest path algorithms [83][84], and the active contour method [85] have been applied to detect the choroid boundaries in OCT images. Most of the above methods were tested on OCT images of healthy subjects. A major drawback of traditional image processing for choroid segmentation techniques is poor robustness since they are highly sensitive to severe pathological images.

Deep learning has gained increasing interest in the domain of medical image processing. Sui et al. [86] presented a multi-scale convolutional neural network (CNN) to learn the edge weights in a graph searching approach to detect the choroid boundaries. Masood et al. [87] performed automatic choroid segmentation using a patch-based CNN and morphological operations. First, they divided the input image into patches, dimensions of 32×32, and then used those patches to train the CNN model. Their dataset consists of healthy, short-sighted, glaucomatous, and DME images. The CNN model shows a precise performance of choroid segmentation in terms of the Dice coefficient, 97.4 ± 2.3. A variety of deep learning models such as CNN, residual network, recurrent neural network, and squeeze and excitation network were explored in the choroid segmentation works of Kugelman et al. [88] and Alonso-Caneiro et al. [89]. They investigated the effects of patch size, network architectures, and image pre-processing techniques on their patch-based and semantic segmentation networks. Chen et al. [90] used two SegNet models [91] to generate edge probability maps for BM and the CSI. Then, seam carving was applied to obtain a complete choroid layer by finding a path of connected pixels between BM and the CSI.

The U-Net [92] is the mainly used network architecture for medical image segmentation tasks. Devalla et al. [93] presented a dilated-residual U-Net model (DRUNET) to segment optic nerve head tissues containing the choroid using glaucomatous and healthy OCT images. DRUNET claims the choroid segmentation performance in Dice coefficient of 90.6 ± 3.5 for healthy images and 91.2 ± 5.0 for glaucomatous images. Zhang et al. [94] introduced an infusing biomarker prior to the global-to-local network (BIONET) for choroid segmentation. BIONET is composed of 1) a biomarker-infused prediction network to learn the biomarker features, 2) a global multi-layered segmentation module to initially segment all layers (retinal layers and choroid layer) in OCT images, and 3) a local choroid segmentation module to segment the choroid using the result from the global module and the learned biomarker features. BIONET obtains a good performance of choroid segmentation in Dice coefficient of 92.5 ± 0.02 for healthy images and 90.2 ± 0.9 for the images with CNV. Hsia et al. [95] segmented the choroid layer using a mask region-based CNN model, composed of deep residual network and feature pyramid networks.

The choroid segmentation performance of deep learning models is very competitive and generally better than those of traditional image processing techniques. In our work, we propose a dense-dilated U-Net model, namely ChoroidNET, to segment the choroid layer and choroidal vessels in OCT images. Automatic extraction of these regions would greatly assist ophthalmologists in diagnosis and monitoring treatment outcomes. ChoroidNET uses the U-Net [92] as a backbone architecture and integrates dilated convolutions with different dilation factors at the bottleneck. The dense connection of dilated convolutions exploits image contexts at multiple scales and improves segmentation performance. The architecture of our proposed ChoroidNET model is explained in Chapter 6. The proposed model has been tested on OCT images with different ophthalmic diseases and pathologies.

The information on datasets used in our experiments and the experimental results are provided in Chapter 7.

5.2 Choroid vessel segmentation

Algorithms based on traditional image processing techniques have been developed for choroidal vessel segmentation. Srinath et al. [96] initially defined the RPE by finding the brightest region and the CSI by calculating the structural similarity index between the choroid and the sclera. Then, choroidal vessels were segmented between the RPE and the CSI using the level set method.

Recently, Liu et al. [97] presented a deep-learning-based choroidal vessel segmentation model adapted from RefineNet [98] in healthy and high myopic OCT images. In their work, RefineNet was evaluated with two ground truth sets annotated by two clinicians (C1 and C2) and compared against VGG-Net-based fully convolutional networks (VGG-FCN) adaptive thresholding and the level-set method [96]. RefineNet was claimed as the best-performed approach, achieving the segmentation agreement of 84.0±3.5 with C1 and 82.3 ± 2.7 with C2, whereas the inter-observer variation between C1 and C2 is 82.1 ± 3.7.

There have been attempts to obtain the choroidal thickness and vasculature from SS-OCT images. Zheng et al. [99] detected the choroid's upper and lower boundaries in OCT images collected from 23 healthy subjects using the Residual U-Net model [100] and then binarization to detect the choroidal vessels using Niblack's algorithm. Based on the detected choroid boundaries and choroidal vessels, six choroidal parameters: choroidal vascularity index, choroidal stromal index, luminal area, stromal area, total choroid area, and choroidal thickness were measured.

Zhou et al. [101] applied an attenuation correction approach to compensate for the attenuated light in SS-OCT images as a pre-processing step in choroid segmentation. Then, choroidal vessel maps, which enable the choroidal vasculature to be visualized without OCT angiography, were generated using a projection of OCT structural information.

Although choroidal vessels are as crucial as the choroid layer in the analysis of retinal diseases, there were only a few state-of-the-art methods for choroidal vessel segmentation. Therefore, our work includes ChoroidNET to perform choroidal vessel segmentation.

5.3 Reviews on existing methods

Table 5.1 discusses and reviews a summary of performances, datasets, advantages, and drawbacks/limitations of some existing choroid layer and vessel segmentation methods.

Table 5.1 A brief description of recent existing methods for the choroid layer and vessel segmentation

Authors	Segmentation Method		Dataset	Performance		Advantages	Drawbacks/Limitations
	Layer	Vessel		Metrics	Value		
Chen et al. [82] (2015)	Detected the choroid upper boundary by thresholding and CSI by searching the shortest path of the graph with the max-min flow in the gradual intensity distance	-	212 peripapillary High Definition-OCT images of eyes from patients (disease unspecified)	Overlap ratio (Choroid Layer)	85.0%	Performance was evaluated in terms of inter-and intra-observer variability.	Thresholding-based upper boundary detection may be sensitive to severe pathology present in the image.
Hussian et al. [84] (2018)	Segmented the choroid layer using Dijkstra's short path algorithm and depth-based intensity normalization technique.	Segmented the choroidal vessels using Otsu's clustering method.	190 foveal-centered EDI-OCT images of eyes without a history of retinal diseases	Dice coefficient (Choroid Layer)	92.9%	Performance was validated against two expert observers.	To confirm the robustness, only two SS-OCT images of eyes with AMD and CNV were tested. Vessel segmentation performance
Salafian et al. [79] (2018)	Transformed the input image into a neutrosophic space that contains true, false, and indeterminate sets. Then, the Dijkstra shortest path algorithm was applied to detect the choroid boundaries based on the calculated weights between pairs of nodes in the image.	-	15 foveal-centered and 17 peripapillary EDI-OCT images of healthy eyes and eyes with multiple sclerosis	Unsigned error (foveal-centered) Unsigned error (peripapillary)	3.34 pixels 6.65 pixels	Choroid segmentation was performed in both peripapillary and foveal-centered OCT images.	The algorithm was tested on small datasets.
Lu et al. [85] (2013)	Segmented the choroid upper boundary using a variational active-contour model and CSI by minimizing an energy function model using a dynamic programming technique.	-	30 foveal-centered EDI-OCT images of eyes from patients with diabetes	Dice coefficient (Choroid Layer)	92.7 ± 3.6	Real-time human interaction was offered to guide CSI segmentation intelligently.	The algorithm may not be robust for the images which have poorer quality than EDI-OCT images.
Wang et al. [80] (2017)	Segmented the choroid layer using the level set method in which a distance regularization term, an edge constraint term, and a region (around the CSI) term are embedded to detect the indistinct CSI and to compensate for inconsistent textures in the choroid.	-	600 foveal-centered SS-OCT images from healthy subjects	(Choroid Layer) Dice coefficient Mean signed difference Mean unsigned difference	 90.0 ± 4.0 1.59 ± 1.65 2.17 ± 1.77	Construction of a thickness map of the choroid layer in the same volume image was performed.	There is a lack of performance testing on pathological images.
Sui et al. [86] (2017)	Segmented BM and CSI using a convolutional neural network (CNN) which generates graph-edge weights for BM and CSI, and a graph searching technique.	-	912 foveal-centered EDI-OCT images (618 normal images and 294 macular edema images)	Mean square error (BM) Mean square error (CSI) Absolute error (BM) Absolute error (CSI)	0.9 9.5 4.6 ± 4.8 11.4 ± 11.0	The multi-scale CNN combines local and global information, at coarse, middle, and fine image scales, which is important for object segmentation.	Choroidal vessel segmentation was not performed.
Masood et al. [87] (2019)	Segmented the choroid layer using a patch-based CNN model and morphological operations.	-	525 foveal-centered OCT images of healthy, short-sighted, glaucomatous, and DME eyes	Dice coefficient (Choroid Layer)	97.4 ± 2.3	High segmentation performance was claimed and the thickness map construction of the choroid layer in the same volume image was provided.	Choroidal vessel segmentation was not performed.

Table 5.1 (Continued)

Authors	Segmentation Method		Dataset	Performance		Advantages	Drawbacks/Limitations
	Layer	Vessel		Metrics	Value		
Kugelman et al. [88] (2019)	Segmented the boundaries of the outer RPE and CSI using different deep learning methods such as standard U-Net, residual network, recurrent neural network, squeeze and excitation network, and the combined network, followed by a graph search procedure.	-	594 foveal-centered SD-OCT images of eyes from 99 healthy children	Mean absolute error (Outer RPE) Mean absolute error (CSI)	0.44 ± 0.11 (in pixel) 2.53 ± 1.52 (in pixel)	ILM segmentation was also included in their experiment. Comparisons of segmentation performance based on different patch sizes were also presented.	There is a lack of performance testing on pathological images.
Chen et al. [90] (2017)	Segmented BM and CSI using two SegNet models [24]. Then, the region between BM and CSI was filled to provide a full choroid layer segmentation.	-	62 foveal-centered EDI-OCT images of eyes with dry and wet AMD	Dice coefficient (Choroid Layer)	83.0 ± 0.1	The segmentation model is robust to the pathology in eyes with AMD.	Choroidal vessel segmentation was not performed.
Devalla et al. [93] (2018)	Segmented optic nerve head (ONH) tissues, including the choroid, using a dilated-residual U-Net model (DRUNET).	-	100 ONH-centered EDI-OCT images (40 healthy subjects and 60 subjects with glaucoma)	(Choroid Layer) Dice coefficient - healthy - glaucoma	 90.6 ± 3.5 91.2 ± 5.0	Segmentation of other ONH tissues (lamina cribrosa, sclera, etc.) was included.	Choroidal vessel segmentation was not performed.
Zhang et al. [94] (2020)	Segmented the choroid layer using a biomarker-infused global-to-local network (Bio-Net).	-	1,280 foveal-centered OCT images of healthy eyes and eyes with CNV	(Choroid Layer) Dice coefficient - healthy - CNV	 92.7 ± 0.0 90.2 ± 0.9	Visualization of choroidal vasculature in en-face images was further performed using a generative adversarial inpainting network.	Choroidal vessel segmentation in OCT images was not included.
Hsia et al. [95] (2021)	Segmented the choroid layer using a mask region-based CNN model, composed of ResNet and feature pyramid networks.	-	750 foveal-centered EDI-OCT images of healthy eyes	Accuracy (Choroid Layer)	87.5%	The performances of ResNet-50, ResNet-101, (ResNet-50 ∩ ResNet-101), and (ResNet-50 ∪ ResNet-101) were reported.	There is a lack of performance testing on pathological images. Choroidal vessel segmentation was not performed.
Srinath et al. [96] (2014)	Detected the choroid boundaries using structural similarity and adaptive Hessian technique.	Segmented the choroidal vessels using the level set approach.	OCT images	-	-	-	The algorithm may be sensitive to the retinal pathology.
Liu et al. [97] (2019)	-	Segmented the choroidal vessels using RefineNet [30].	40 foveal-centered SS-OCT images of eyes with emmetropes and high myopia.	Segmentation agreement C1 vs RefineNet C2 vs RefineNet	 84.0 ± 3.5 82.3 ± 2.7	Good segmentation agreement between the RefineNet results and clinicians (C1 and C2) was achieved.	Choroid layer segmentation was not performed.
Zheng et al. [99] (2021)	Segmented the choroid's upper and lower boundaries using Residual U-Net [100].	Segmented the choroidal vessels using Niblack's binarization	217 foveal-centered SS-OCT images of eyes without retinal pathology.	Failure ratio (2%) (Upper boundary) Failure ratio (2%) (Lower boundary)	0.22 13.23	Six choroidal parameters were measured based on the choroid layer and vessel segmentation results.	The performance of choroidal vessel segmentation was not reported.

5.4 Reviews on deep learning techniques

This section reviews deep learning techniques that are currently applied in the analysis of OCT images. U-Net and its variants are described in the following sub-sections.

5.4.1 U-Net architecture

The U-Net [92] is a convolutional network architecture for segmenting medical images. It comprises an encoder (a contracting path) and a decoder (an expansion path). The encoder is as same as the conventional CNN. Each step in the encoder contains two consecutive 3×3 standard convolutions followed by a rectified linear unit (ReLU) [102] and a 2×2 max-pooling operation (downsampling) with stride 2 and doubling the number of feature maps. Each step in the decoder performs up-sampling of the feature maps and a 2×2 convolution with half the number of feature maps. The activation maps of the encoder path are directly concatenated with the corresponding up-sampled maps in the decoder path through skip connections. A 1×1 convolution is employed to map the features to the number of classes at the network's last layer. An example of U-Net architecture is shown in Figure 5.1. With recent advancements in deep learning, there have been large efforts in modifying and improving conventional U-Net.

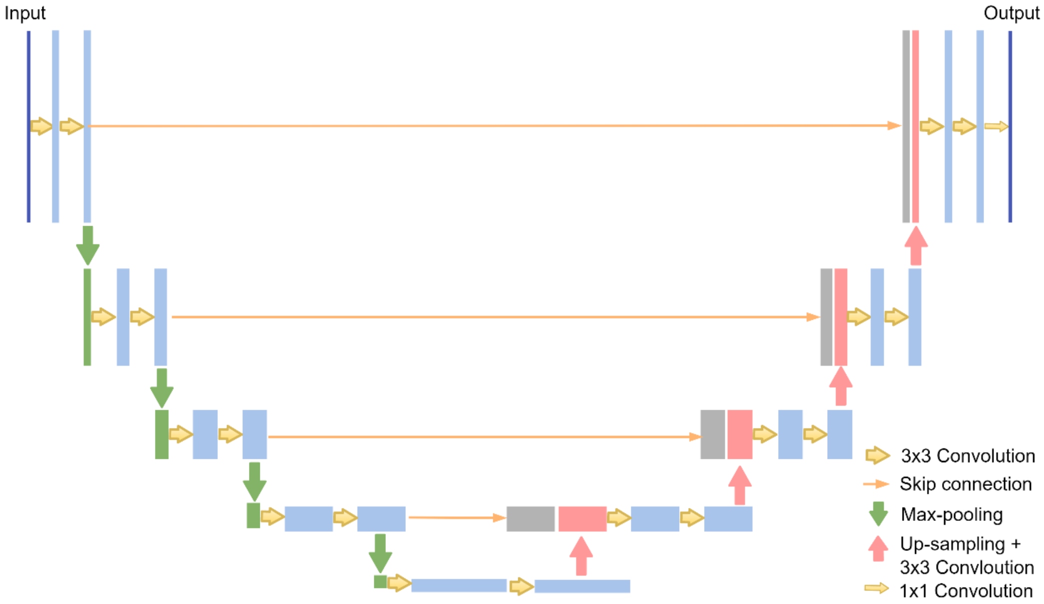

Figure 5.1 Network architecture of U-Net.

5.4.2 U-Net++ architecture

U-Net++ [103] is an enhanced variant of the U-Net architecture [92] that contains densely connected nested sub-networks and skip connections. The architecture of U-Net++ is illustrated in Figure 5.2. Similar to U-Net, a convolutional block contains two consecutive 3 × 3 standard convolutions and results in an activation map ($X^{i,j}$) where i denotes the max-pooling layer along the encoder and j denotes the up-sampling layer along the skip pathways. All layers in a convolutional block are batch-normalized (BN) and activated by a rectified linear unit (ReLU). Similar to U-Net, the number of feature vectors is doubled along with the encoder and is halved along with the decoder. At the last layer of the network, a 1 × 1 convolution and a sigmoid activation are applied to obtain the pixel-wise binary segmentation for each pixel. The gray convolutional blocks distinguish U-Net++ from U-Net. The use of nested skip pathways aids U-Net++ in bridging the semantic gaps and flowing the gradient information between the encoder and decoder paths and enables it to perform segmentation more precisely. U-Net++ provides better performance than U-Net but still cannot resolve the loss of spatial information. U-Net++ was used to segment polyp, liver, and cell nuclei datasets.

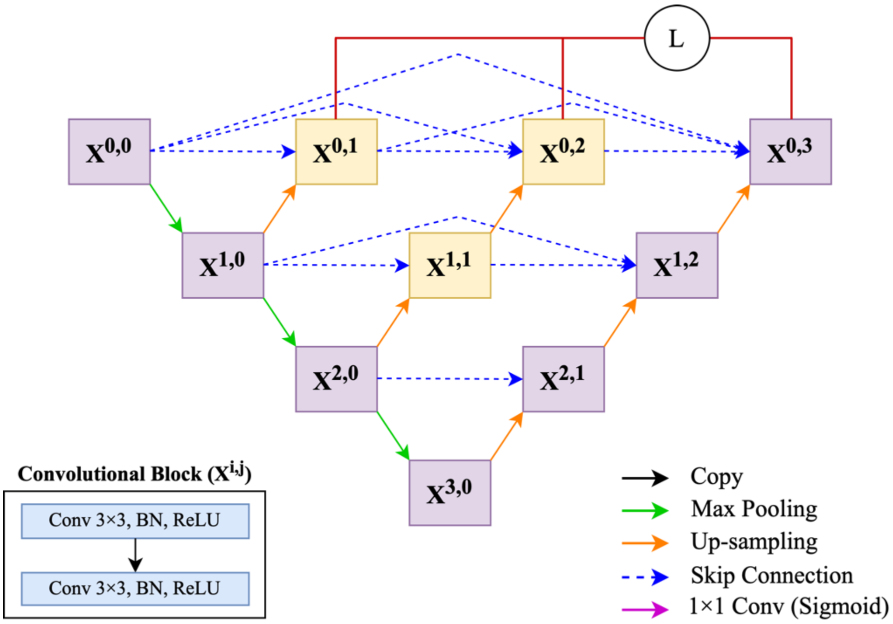

Figure 5.2 Network architecture of U-Net++.

5.4.3 DRUNET architecture

The DRUNET, a dilated-residual U-Net model, was presented by Devalla et al. [93] to segment optic nerve head tissues containing the choroid using glaucomatous and healthy OCT images. DRUNET is composed of two towers: a downsampling tower for capturing the contextual information (spatial arrangement of tissues), and an upsampling tower for capturing the local information (tissue structures). Each tower consists of two blocks: a standard block and two residual blocks that integrate with dilated convolutions. As opposed to U-Net, DRUNET uses 16 feature maps in every block in the network without doubling or halving the number of feature vectors. Figure 5.3 shows the DRUNET architecture. Thus, DRUNET consisted of only a total of 40,000 trainable parameters. The use of dilated convolutions helps DRUNET to learn rich spatial information while the use of a low number of feature vectors makes DRUNET weak in learning more complex patterns (abstractions) in images with pathologies.

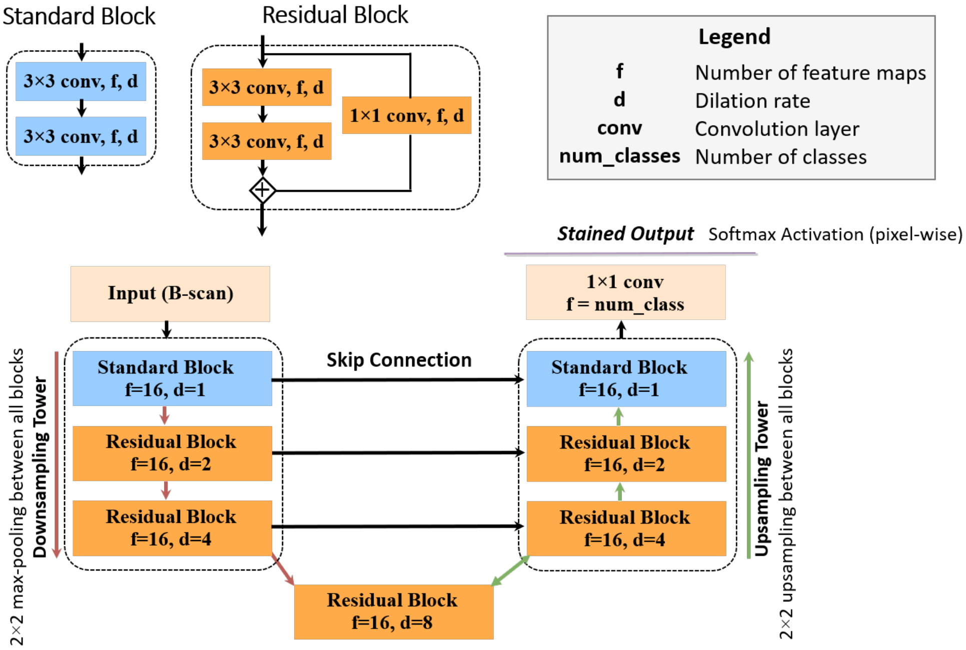

Figure 5.3 Network architecture of DRUNET.

5.4.4 Residual U-Net architecture

Residual U-Net [100] is another improved variant of U-Net that inserts a residual connection in every convolutional block in the U-Net strucutre. Similar to U-Net, it uses same order of feature number of feature vectors (f). The architecture of residual U-Net is shown in Figure 5.4. Due to its residual connection, the number of parameters used in Residual U-Net is doubled those used in a conventional U-Net. Yet it still lose some spatial information at the deeper layer of the network. To solve this, we aim to develop a new deep learning model that can capture spatial information and complex patterns together. Residual U-Net was used for detecting the upper and lower boundaries of choroid using fovea-centered SS-OCT images [99].

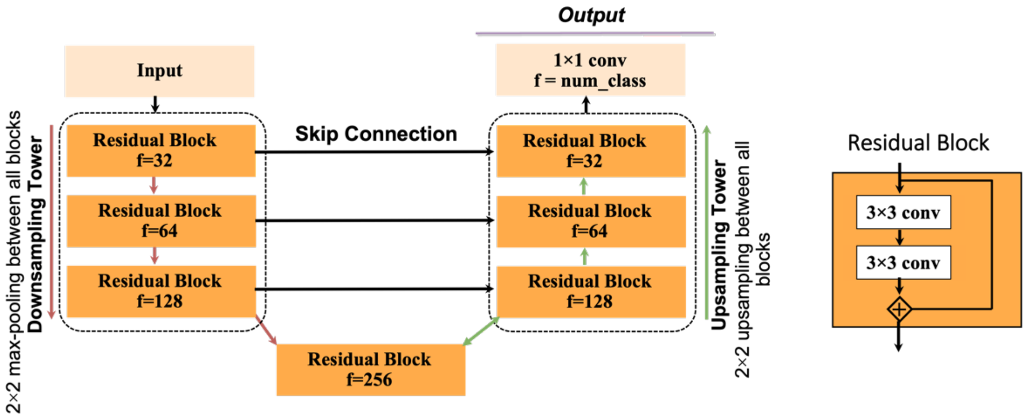

Figure 5.4 Network architecture of Residual U-Net.

Chapter 6

The proposed method for choroid layer and vessel segmentation in OCT images

Chapter 6 Proposed method for choroid layer and vessel segmentation in OCT images

This chapter describes the technical background and architecture of the proposed ChoroidNET model in Sections 6.1 and 6.2. The measurement techniques of choroidal parameters are provided in Section 6.3.

6.1 Technical Background

Initially, we preprocess each extracted patch using normalized gamma-corrected contrast-limited adaptive histogram equalization to denoise and enhance the contrast of OCT images. Normalization is performed to adjust the range of pixel intensity values in the input patch with a gray-level dynamic range. The gamma correction process is a gray-level transformation to enhance the poor luminance of the input patch [104].

$$N = \frac{\left[X - \min(X)\right]}{\left[\max(X) - \min(X)\right]} \tag{6.1}$$

$$R = X^{\gamma} \tag{6.2}$$

where N denotes a normalization function, X denotes the input patch, R denotes the gamma-adjusted image, and γ denotes a constant gamma value. Figure 6.1 illustrates the pre-processing procedures.

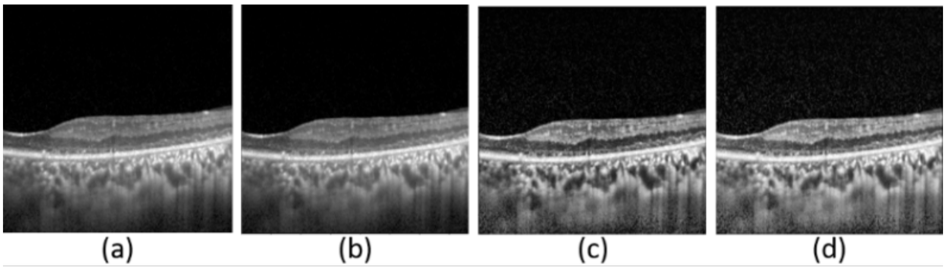

Figure 6.1 Pre-processing steps for a patch; (a) an input image, (b) after normalization, (c) after enhancement, and (d) after the gamma adjustment.

Training is then performed using the preprocessed patches. We also perform data augmentation during training, including affine transformation, horizontal flipping, random distortion, and zooming.

6.1.1 Dilated convolutions

A dilated convolution refers to a convolution conducted with a dilated filter. Yu et al. [105] and Chen et al. [106] reported that dilated convolutions can be used instead of down-sampling operations to expand the receptive field without degrading the resolution of intermediate feature maps by inserting zeros between the pixels of the kernel. Consider convolutional kernel K_l with a kernel size of $k \times k$ in dilated layer l. The receptive field F_{K_l} of the kernel K_l can be calculated as:

$$F_{K_l} = k + (k-1) \times (D_{K_l} - 1) \tag{6.3}$$

where D_{K_l} denotes the dilation rate of kernel K_l. Figure 6.2 shows how the dilated convolutions adaptively enlarge the FOVs by increasing the dilation rates.

For the dilation block of LSM, we increase the dilation factors in increments of 2. We experimentally found that this increasing order of dilation factors yields better performance in the choroid layer segmentation. However, aggressively increasing dilation factors is less effective for small objects such as choroidal vessels. Dilated convolutions with increasing dilation factors lead to weak spatial inconsistency between neighboring pixels; thus, it fails to aggregate local features. Hamaguchi et al. [107] used a local feature extractor after large contexts are aggregated by increasing the dilation factors to address this. The local feature extractor helps extract local features by decreasing the dilation factors. Inspired by this concept, for the dilation block of VSM, we first increase the dilation factors gradually and then drop them to recover consistency between neighboring pixels.

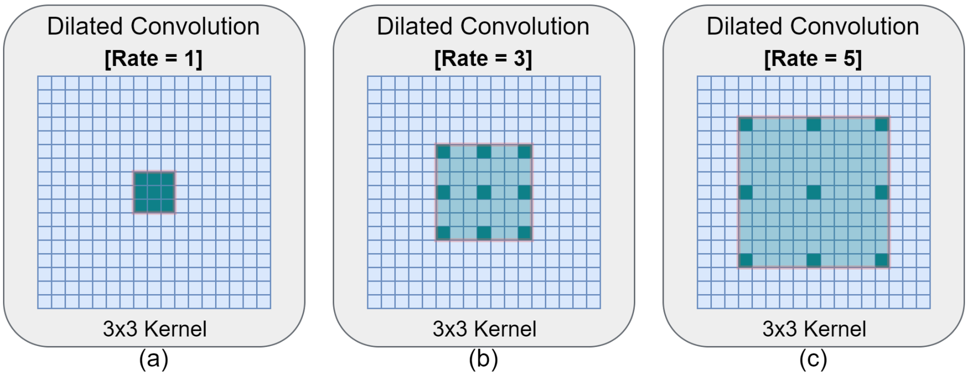

Figure 6.2 Representation of increasingly dilated convolutions with 3×3 kernel and their receptive fields for (a) rate = 1 (equivalent to standard convolution), (b) rate = 3, and (c) rate = 5.

6.1.2 DropBlock regularization

Dropout [108] is a widely used regularization technique for fully connected networks. It prevents the overfitting caused by coadaptation on the training dataset by reducing the complexity of the network architecture and randomly dropping out independent features. However, this technique is less effective for convolutional networks where the features are spatially correlated because semantic information can still leak through the networks. Thus, Ghiasi et al. [109] proposed DropBlock [110], a structured dropout form, to regularize convolutional networks effectively. We apply DropBlock to prevent our network from overfitting and effectively to remove semantic information. Figure 6.3 shows how DropBlock discards some contiguous regions that contain certain semantic information from a feature map of the choroid layer.

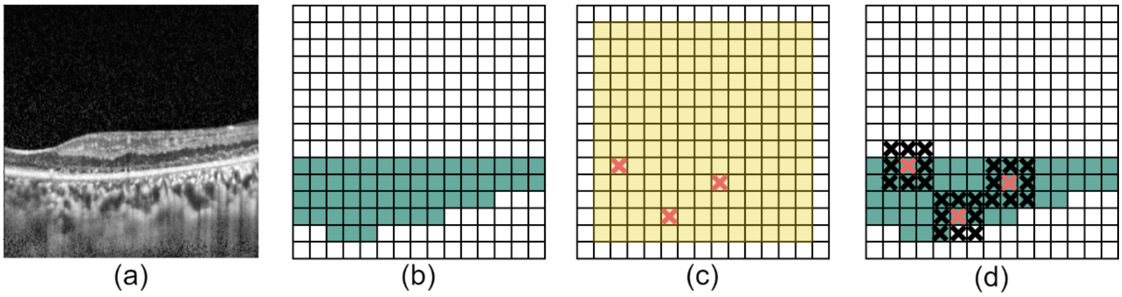

Figure 6.3 Illustration of how DropBlock drops features. (a) Input patch, (b) activation units (green area) of semantic information in (a) for the choroid layer, (c) DropBlock mask (yellow area) and sampled zero entries (red x's), and (d) zero entries on mask expanded to zero blocks (black x's around red x's).

6.1.3 Loss function and optimizer

The loss function (L) was based on the sum of binary cross-entropy loss (L_{BCE}) and Dice loss (L_D), as shown in the following Equations.

$$L(y,\hat{p}) = L_{BCE}(y,\hat{p}) + L_D(y,\hat{p}) \tag{6.4}$$

$$L_{BCE}(y,\hat{p}) = -(y\log(\hat{p}) + (1-y)\log(1-\hat{p})) \tag{6.5}$$

$$L_D(y,\hat{p}) = 1 - \frac{2y\hat{p}}{y+\hat{p}} \tag{6.6}$$

where $y \in [0,1]$ and $\hat{p} \in [0,1]$ respectively denote the set of pixels in the ground truth and the set of pixels predicted by the trained network. With this combined loss, the training can mix and leverage the curve smoothness of binary cross-entropy loss and the flexibility of Dice loss of class imbalance at the same time [111].

The RMSprop optimizer was used in our network to reduce the learning rate adaptively. It is a gradient-based optimization technique that utilizes a moving average of squared gradients based on normalization to balance momentum.

6.2 Architecture of ChoroidNET

Figure 6.4 shows the network architecture of ChoroidNET. The model comprises a layer segmentation module (LSM) and a vessel segmentation module (VSM). Each module consists of an encoder path, a decoder path, and a dilation block, which uses dense dilated convolutions instead of standard convolutions. The blocks used in the network are defined as follows. A standard (purple) block corresponds to the resulting activation map from two successive 3×3 standard convolutions. All layers in a standard block are regularized by DropBlock (DB) [109], batch-normalized (BN) [112], and activated by ReLU [102]. A gray block represents the activation map forwarded from the encoder path concatenated with the corresponding up-sampled map in the decoder path. The red and yellow blocks, at the bottleneck of LSM and VSM, respectively, are dilation blocks that comprise six dilated convolutions with different dilation factors. These dilation blocks help ChoroidNET overcome the loss of detailed spatial information and difficulty extracting contextual semantic features. ChoroidNET thus has a good segmentation accuracy, resulting in smooth boundaries of the choroid layer. The intersection area of the input patch and the choroid layer prediction from LSM is fed into VSM to obtain a more consistent segmentation of choroidal vessels.

Encoder Path. The number of feature vectors is doubled at each level of the encoder path. Thus, the bottommost level of the encoder path generates high-level semantic features. The purpose of the encoder path is to capture the contextual information of the input patches. Skip connections feed this information to the decoder path [113].

Decoder Path. After each level of the decoder path, a 2×2 up-sampling operation is applied to restore the image to its original size. The purpose of the decoder path is to perform semantic segmentation by concatenating up-sampled outputs and the contextual information transferred from the encoder path via skip connections. The features generated by the dilation block are added to achieve multi-scale context aggregation. Finally, a 1×1 convolution and a sigmoid activation are applied to obtain the pixel-wise binary segmentation for each pixel.

6.3 Measurement of choroidal parameters

There are two main parts to this measurement step. The first part is to segment the choroid layer and vessels and detect the fovea. The second is to measure the choroidal parameters. The details of the method are described in the following sub-sections. Figure 6.5 shows a flowchart illustrating an overview of the proposed measurement technique.

To measure the choroidal thickness at the fovea, the fovea must be detected in the processing step.

Initially, we applied the Sobel filter [114] to the input image f. Figure 6.6 illustrates the fovea detection process. The horizontal and vertical components of the gradients were calculated by convolving with the Sobel operators, as in Equations 6.7 and 6.8. The gradient magnitude image $G(x, y)$ was obtained using Equation 6.9.

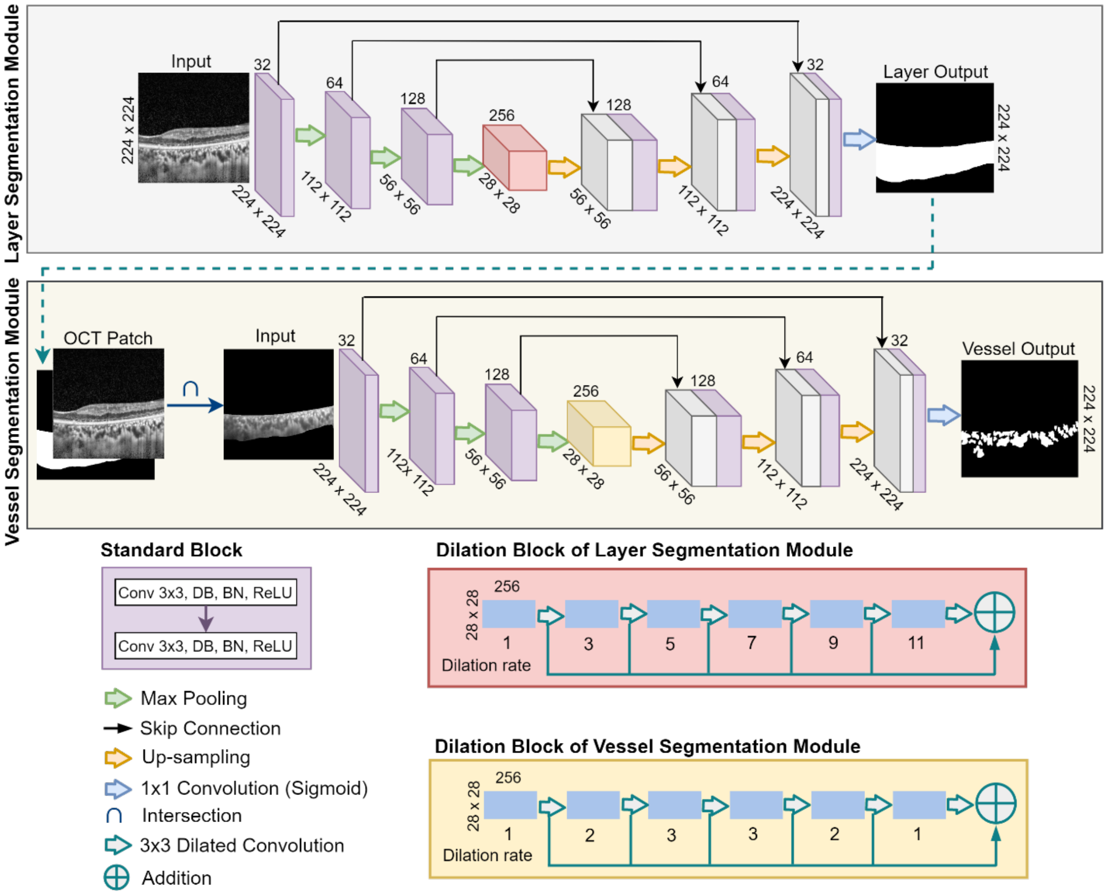

Figure 6.4 Network architecture of ChoroidNET.

$$\frac{\partial f}{\partial x} = \begin{bmatrix} 1 & 0 & -1 \\ 2 & 0 & -2 \\ 1 & 0 & -1 \end{bmatrix} \otimes f \qquad (6.7)$$

$$\frac{\partial f}{\partial y} = \begin{bmatrix} 1 & 2 & 1 \\ 0 & 0 & 0 \\ -1 & -2 & -1 \end{bmatrix} \otimes f \qquad (6.8)$$

$$G(x,y)=\sqrt{\left(\frac{\partial f}{\partial x}\right)+\left(\frac{\partial f}{\partial y}\right)} \tag{6.9}$$

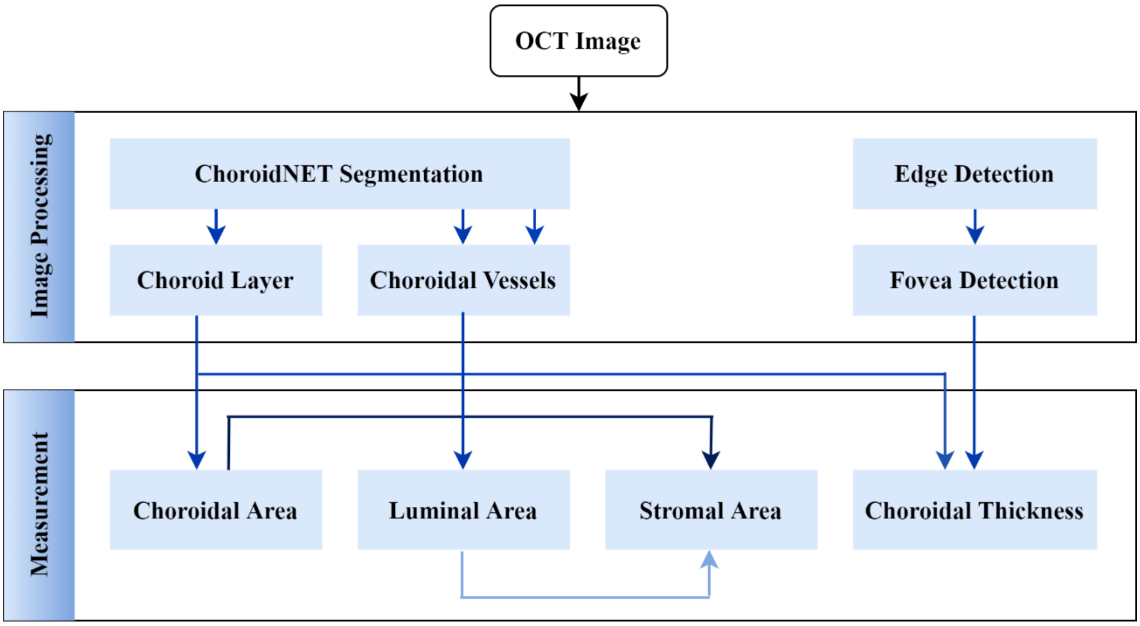

Figure 6.5 Overview of the proposed measurement technique.

A threshold was applied to the gradient magnitude image to obtain a binary edge map. After removing many small objects from the binary image, the detected internal limiting membrane (ILM) was obtained. Since all images in our dataset are foveal-centered, a sub-image was created by cropping around the center of the image. The edge linking technique was applied if there was more than one edge in the sub-image. The endpoints at the left and right sides of the image were connected with a line. We then calculated the difference between the detected ILM and the line. It is illustrated in Figure 6.7 (f). We assumed the place with the maximum difference as the fovea. The detected fovea is shown in Figure 6.7 (g).

In the measurement part, we calculated four choroidal parameters: the total choroidal area (TCA), the luminal area (LA), the stromal area (SA), and the choroidal thickness (CT) based on ChoroidNET's segmentation results of the choroid layer and vessels. Equations 6.10-6.13 show the formulas for calculating those parameters.

TCA is calculated as the pixels occupied by the choroid layer image CL (see Figure 6.7 (b)).

$$TCA=\sum\nolimits_{i=1,j=1}^{n} CL(i,j) \tag{6.10}$$

LA is calculated as the pixels occupied by the choroidal vessel image CV (see Figure 6.7 (c)).

$$LA=\sum\nolimits_{i=1,j=1}^{n} CV(i,j) \tag{6.11}$$

SA is calculated by extracting the luminal area from the total choroidal area. It is illustrated in Figure 6.7 (d).

$$SA=TCA-LA \tag{6.12}$$

CT is measured as the distance between the upper choroid layer to the lower choroid layer in

$CL(i,j)$ at the detected fovea. It is illustrated in Figure 6.7 (a).

$$CT = \sqrt{(x_l - x_u)^2 + (y_l - y_u)^2} \tag{6.13}$$

where (x_u, y_u) and (x_l, y_l) denote as the coordinates of the upper and lower choroid layers at the fovea.

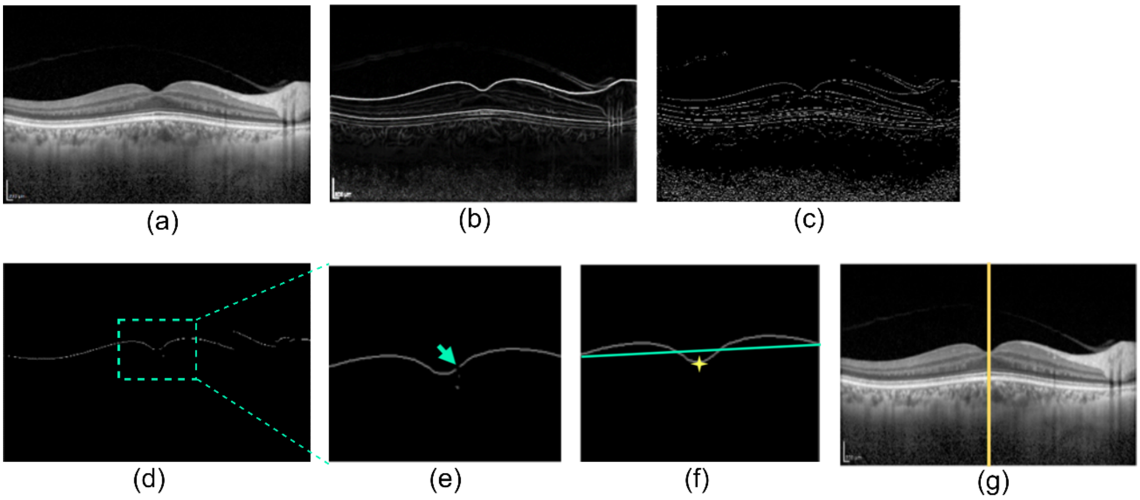

Figure 6.6 Fovea detection process. (a) Input, (b) Gradient magnitude image, (c) Binary edge image, (d) ILM boundary, (e) Sub-image that has unconnected edges of ILM, (f) Sub-image showing the connected ILM and the detected fovea, and (g) Detected fovea (yellow line).

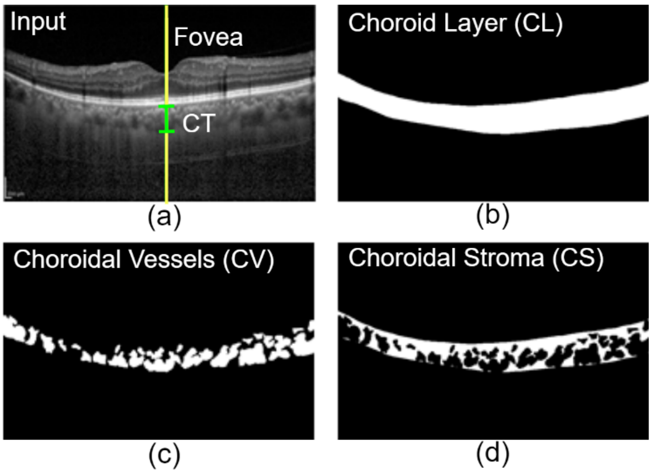

Figure 6.7 Representation of OCT images to illustrate the measurement technique. (a) An OCT image showing the fovea and CT, (b) Choroid layer image, (c) Choroidal vessel image, and (d) Choroidal stroma image.

Chapter 7

Experiments for choroid layer and vessel segmentation in OCT images

Chapter 7 Experiment for choroid layer and vessel segmentation in OCT images

This chapter presents the experiments on the choroid layer and vessel segmentation. Section 7.1 describes the datasets used in this work. The ground truth preparation process, evaluation metrics, and experimental setup are explained in Section 7.2. Section 7.3 presents the results obtained from these experiments. The discussion is given in Section 7.4.

7.1 Retinal OCT images

This section describes the details of the OCT.

7.1.1 Retinitis pigmentosa dataset (Dataset-1)

Our primary dataset contains a total of 105 images, acquired from 52 patients who diagnosed with typical RP. All the patients underwent EDI-OCT protocol at Chiba University Hospital. This study was approved by the Institutional Review Board of Graduate School of Medicine of Chiba University. All procedures were conformed to the tenets of the Declaration of Helsinki.

7.1.2 Public OCT dataset (Dataset-2)

Kermany et al. [115] published a large OCT dataset that contains approximately 80,000 images. These images were acquired via spectral-domain OCT (SD-OCT; Spectralis, Heidelberg Engineering) and collected from the Shiley Eye Institute of the University of California San Diego, the California Retinal Research Foundation, Medical Center Ophthalmology Associates, Shanghai First People's Hospital, and the Beijing Tongren Eye Center. This dataset was constructed to evaluate methods for classifying OCT images into four categories: CNV, DME, Drusen, and Normal. Abnormalities, such as the neovascular membrane and associated subretinal fluid in CNV images, retinal-thickening-associated intraretinal fluid in DME images, and multiple drusen, are present in their dataset. CNV and the appearance of drusen indicate clinical signs of AMD. As Dataset-2, we selected 80 OCT images (20 images from each category) that present a complete choroid view from the large dataset.

7.2 Ground truth preparation, evaluation metrics, and experimental setup

The ground truths of the choroid layer and choroidal vessels were annotated by an expert observer using the ibisPaint application [116]. An ophthalmologist from Chiba University Hospital also helped the ground truths preparation.

The segmentation performance for the choroid layer and choroidal vessels was quantitatively evaluated using five evaluation metrics: accuracy, the Dice coefficient, precision, recall, and specificity. The formulas for accuracy and specificity are expressed in Equations 7.1 and 7.2. Those of precision, recall, and the Dice coefficient (also denoted as F-measure) were defined in Chapter 4 (Equations 4.1-4.3). The numerical results are expressed as means ± standard deviation (SD).

$$\text{Accuracy} = \left(\frac{TP+TN}{TP+FP+TN+FN}\right) \tag{7.1}$$

$$\text{Specificity} = \left(\frac{TN}{TN+FP}\right) \tag{7.2}$$

Sixty images from Dataset-1 were used to create a training set and the remaining images were used to create a test set. 10 images from each category of Dataset-2 were used to create another training set and the remaining images were used to create another test set, respectively. Since the total number of images in the two datasets is small, we enlarge the training sets by using patches cropped from the original images (dimensions: 496×756 in Dataset-1 and 230×495 in Dataset-2). Previous studies have shown that increasing an image patch in a deep learning network provides a more precise segmentation performance since the network can capture more contextual information to make the prediction [117]. Consequently, using a larger image patch requires larger memory. Under consideration of available GPU memory, we chose a patch with enough choroid region, and its size is appropriate to apply down-sampling operations in our network. We extracted 250 patches (dimensions: 384×384) and 300 patches (dimensions: 224×224) from each image in a trainset set of Dataset-1 and Dataset-2. Note that the areas of some patches overlapped. 90% of each training set was used for training, and the remaining 10% was used for validation. ChoroidNET was trained on each training set end-to-end using a computer with an Intel Core i7 CPU and an NVIDIA GeForce GTX 1070 Ti GPU. The training was performed for 50 epochs with a batch size of 4 and an initial learning rate of 0.0001.

The performance of ChoroidNET is compared against U-Net++ L^3 [103], DRUNET [93], and Residual U-Net [100]. As mentioned in Section 5.4, U-Net++ is an improved U-Net architecture based on nested and dense skip connections. DRUNET and Residual U-Net also adopt the structure of U-NET. DRUNET integrates dilated residual blocks instead of standard convolutional blocks (except at the top-level). DRUNET was designed for segmenting the optic nerve head (ONH) tissues (including the choroid) in ONH-centered SD-OCT images. Residual U-Net was used for detecting the upper and lower boundaries of choroid using fovea-centered SS-OCT images. For a fair comparison, we trained and validated U-Net++, DRUNET, and Residual U-Net using the same training and test sets used for ChoroidNET, and performed the same data augmentation, pre-processing, and DropBlock regularization as that in our experiment.

7.3 Experimenal Results

This section describes the experimental results of the choroid layer and vessel segmentation using two OCT datasets.

7.3.1 Choroid layer and vessel segmentation using ChoroidNET

The segmented images produced by U-NET++, DRUNET, Residual U-NET, and ChoroidNET were qualitatively compared with their corresponding ground truths and quantitatively evaluated. Figures 7.1 and 7.2 show examples of the choroid layer and choroidal vessel segmentation results. Tables 7.1 and 7.2 compare the performance of the choroid layer and choroidal vessel segmentation for the tested networks.

The choroid layer segmentation results for ChoroidNET are qualitatively comparable to the ground truths. ChoroidNET shows the best segmentation performance (Dice coefficient: 94.9 ± 1.5, 95.1 ± 0.4) for both Dataset-1 and Dataset-2. U-Net++ segmented the choroid layer as smooth as the ground truths and also had the highest precision (96.2 ± 1.0) and specificity (99.6 ± 0.1). However, it was inferior to ChoroidNET in terms of the Dice coefficient and recall. The DRUNET produced irregular choroid boundaries and oversegmented areas outside the choroid layer for the CNV and DME images of Dataset-2. Residual U-Net results are similar to the ground truths; however, the segmented boundaries of the choroid are not smooth.

ChoroidNET outperformed the other models in terms of choroidal vessel segmentation performance. It had the highest Dice coefficient (80.8 ± 1.9, 82.4 ± 2.4) and recall (82.3 ± 2.2, 87.2 ± 2.8). U-Net++ yielded the second-best performance in terms of Dice coefficient (80.2 ± 2.6) for Dataset-1 and the highest precision (80.5 ± 5.7) and specificity (98.7 ± 0.3) for Dataset-2. Residual U-Net had the highest precision (84.1 ± 1.9) and specificity (99.4 ± 0.1) for Dataset-1. U-Net++ and Residual U-Net segmented irrelevant areas (intraretinal fluid) outside the choroid for DME images. DRUNET exhibited over-segmentation around the upper choroid layer in CNV and Drusen images.

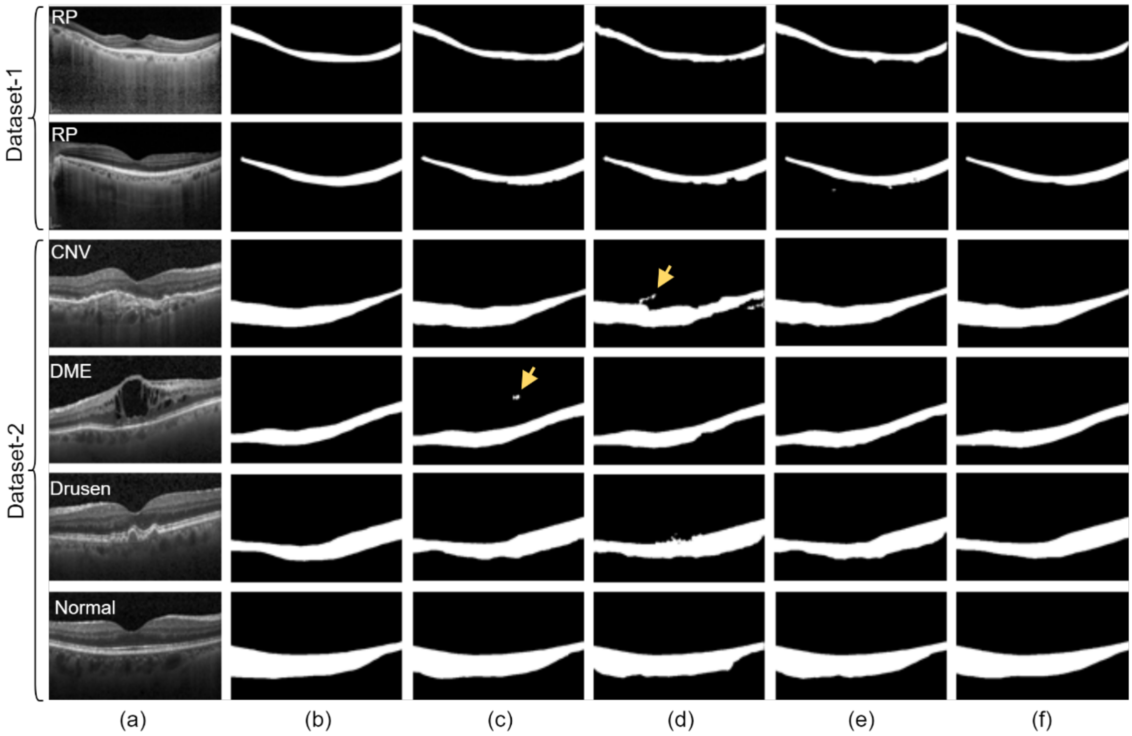

Figure 7.1 Choroid layer segmentation results. (a) Input, (b) ground truth, and results for (c) U-Net++, (d) DRUNET, (e) Residual U-Net, and (f) ChoroidNET. The yellow arrow indicates over-segmentation.

Table 7.1 Performance comparison of choroid layer segmentation (highest score in bold)

Dataset	Metric (mean ± SD)	U-Net++	DRUNET	Residual U-Net	ChoroidNET
1	Accuracy	98.8 ± 0.3	98.5 ± 0.8	98.7 ± 0.4	**99.0 ± 0.3**
	Dice coefficient	94.0 ± 1.4	92.4 ± 4.6	93.5 ± 2.1	**94.9 ± 1.5**
	Precision	**96.2 ± 1.0**	95.2 ± 1.1	95.2 ± 1.2	95.9 ± 0.9
	Recall	91.9 ± 2.5	89.7 ± 7.8	99.5 ± 0.1	**94.0 ± 3.1**
	Specificity	**99.6 ± 0.1**	99.5 ± 0.1	91.8 ± 3.8	**99.6 ± 0.1**
2	Accuracy	98.2 ± 0.2	97.8 ± 0.1	98.1 ± 0.1	**98.5 ± 0.2**
	Dice coefficient	94.0 ± 1.1	92.5 ± 1.3	93.6 ± 1.0	**95.1 ± 0.4**
	Precision	92.2 ± 2.4	91.1 ± 2.7	92.9 ± 1.9	**94.1 ± 1.6**
	Recall	96.0 ± 0.8	94.0 ± 1.3	94.3 ± 0.8	**96.1 ± 0.9**
	Specificity	98.6 ± 0.3	98.4 ± 0.3	98.8 ± 0.2	**99.0 ± 0.3**

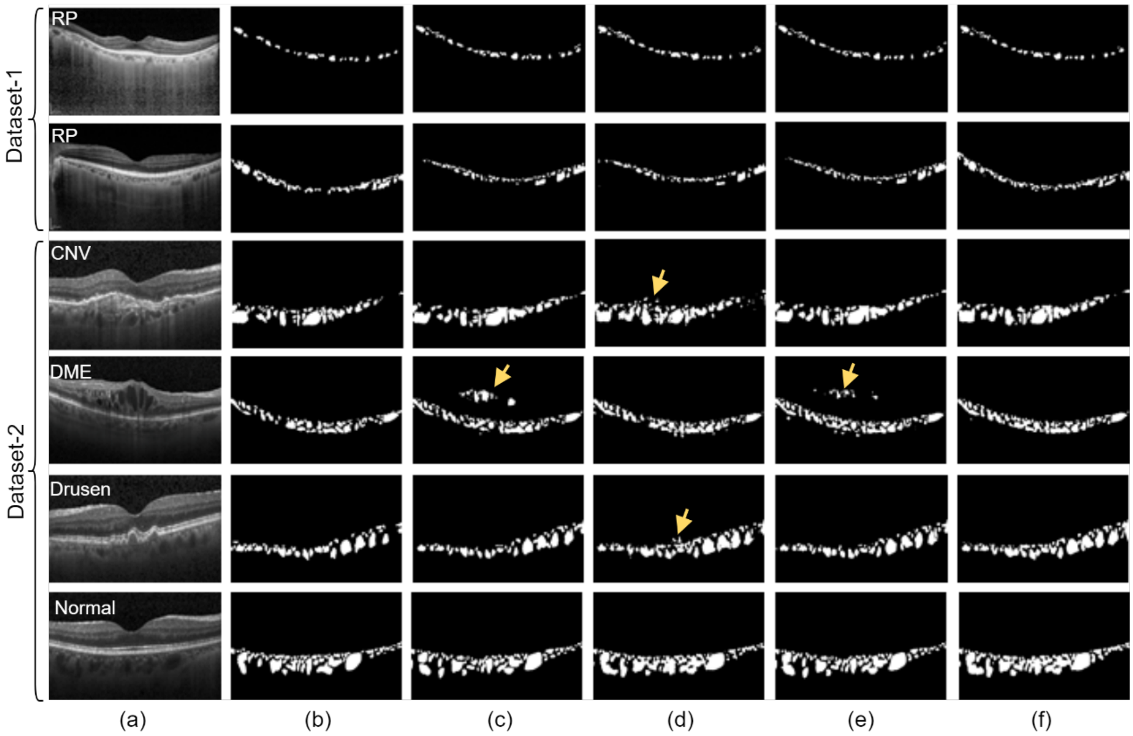

Figure 7.2 Choroidal vessel segmentation results. (a) Input, (b) ground truth, and results for (c) U-Net++, (d) DRUNET, (e) Residual U-Net, and (f) ChoroidNET. Yellow arrow indicates oversegmentation.

Table 7.2 Performance comparison of choroidal vessel segmentation (highest score in bold)

Dataset	Metric (mean ± SD)	U-Net++	DRUNET	Residual U-Net	ChoroidNET
1	Accuracy	**98.5 ± 0.2**	98.4 ± 0.2	98.4 ± 0.3	**98.5 ± 0.2**
	Dice coefficient	80.2 ± 2.6	79.2 ± 3.1	78.9 ± 2.6	**80.8 ± 1.9**
	Precision	81.5 ± 2.1	79.8 ± 2.6	**84.1 ± 1.9**	79.3 ± 2.2
	Recall	79.0 ± 4.2	78.6 ± 4.7	74.3 ± 3.8	**82.3 ± 2.2**
	Specificity	99.3 ± 0.1	99.2 ± 0.1	**99.4 ± 0.1**	99.1 ± 0.1
2	Accuracy	97.6 ± 0.3	97.4 ± 0.4	97.6 ± 0.4	**97.7 ± 0.4**
	Dice coefficient	80.8 ± 2.0	80.0 ± 2.6	81.0 ± 2.3	**82.4 ± 2.4**
	Precision	**80.5 ± 5.7**	77.0 ± 5.3	79.5 ± 4.9	78.2 ± 5.6
	Recall	81.0 ± 2.2	83.2 ± 1.1	82.5 ± 1.5	**87.2 ± 2.8**
	Specificity	**98.7 ± 0.3**	97.6 ± 1.6	98.6 ± 0.3	98.4 ± 0.4

7.3.2 Ablation studies of ChoroidNET

To provide insight into each design element of ChoroidNET, we conducted four ablation studies. The ablation models were trained and validated using the same training and test sets. Figure 7.3 shows the architectures of the ablation models. Figures 7.4 and 7.5 show the segmentation results of the choroid layer and the choroidal vessels, respectively, for the ablation models and ChoroidNET. Tables 7.3 and 7.4 compares the choroid layer and vessel segmentation performance of ChoroidNET and its ablation models.

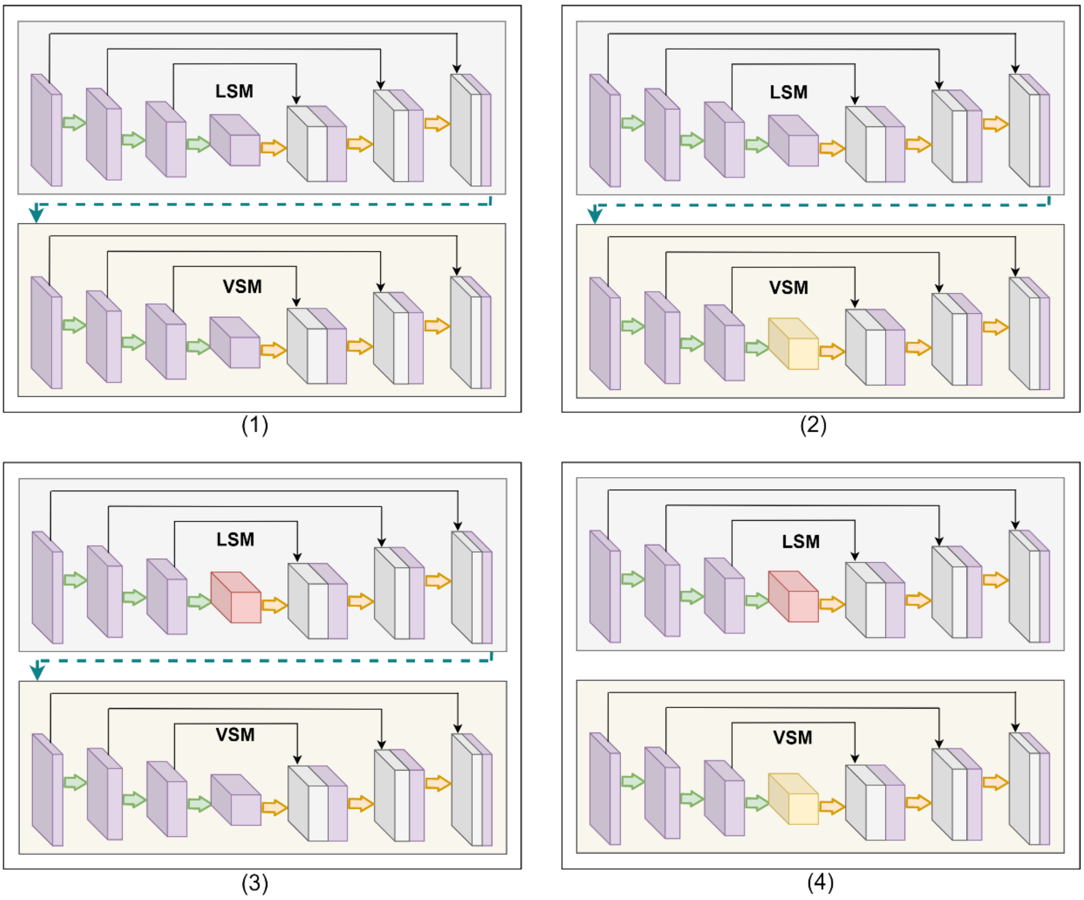

Figure 7.3 Ablation models of ChoroidNET. (1) without dilation blocks in LSM and VSM, (2) without dilation blocks in LSM, (3) without dilation blocks in VSM, and (4) without connection between LSM and VSM.

Ablation-1 and Ablation-2 did not use a dilation block in LSM. For choroid layer segmentation, the boundaries obtained by Ablation-1 and Ablation-2 are not as smooth as the ground truths. The choroid layer segmentation performance of Ablation-3 and Ablation-4 is the same as that of ChoroidNET. ChoroidNET outperforms Ablation-1 and Ablation-2 for the choroid layer segmentation and shows an absolute improvement of 1.9% for Dataset-1 and 1.2% for Dataset-2 in terms of the Dice coefficient. This demonstrates the importance of the dilation block in LSM.

For choroid vessel segmentation, Ablation-1 had the highest recall (83.2 ± 3.4, 92.3 ± 2.2) for Dataset-1 and Dataset-2, but it oversegmented the region outside the choroid layer and thus had the lowest precision (78.1 ± 2.6, 68.6 ± 5.6). Ablation-2 slightly outperforms Ablation-1 by 0.1% and

0.6% in terms of the absolute Dice coefficient. This highlights the efficiency of the dilation block in VSM. The performance improvements (in terms of the Dice coefficient) of ChoroidNET over the four ablation models are (0.3%, 0.2%, 0.6%, and 1.3%) for Dataset-1, and (3.7%, 3.1%, 0.9%, and 0.6%) for Dataset-2, respectively. The improvement of ChoroidNET over Ablation-4 demonstrates the effectiveness of the connection between LSM and VSM.

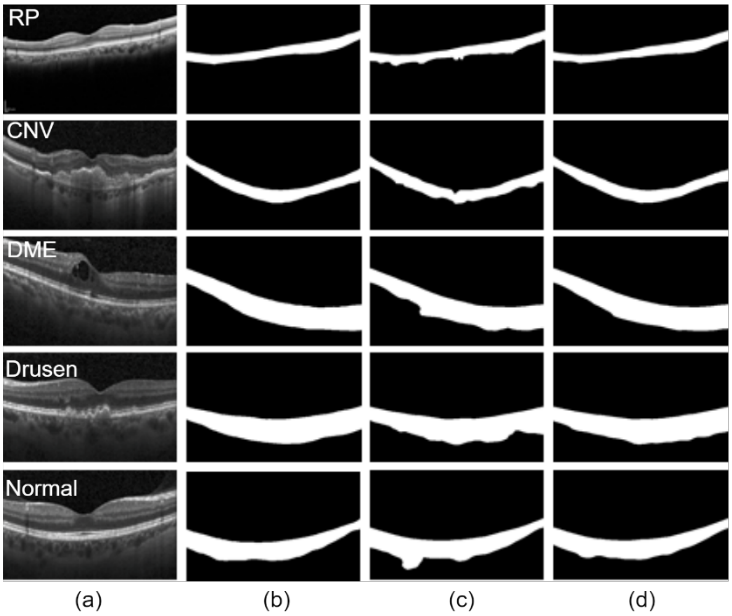

Figure 7.4 Choroid layer segmentation results. (a) Input, (b) ground truth, and results for (c) Ablation-1 and Ablation-2 and (d) Ablation-3, Ablation-4, and ChoroidNET. (RP from Dataset-1, and CNV, DME, Drusen, and Normal from Dataset-2)

Table 7.3 Performance comparison of choroid layer segmentation of ablation models and ChoroidNET (highest score in bold)

Dataset	Metric (mean ± SD)	Ablation-1 & Ablation-2	Ablation-3, Ablation-4 & ChoroidNET
1	Accuracy	98.6 ± 0.3	99.0 ± 0.3
	Dice coefficient	93.0 ± 1.8	**94.9 ± 1.5**
	Precision	92.2 ± 2.2	95.9 ± 0.9
	Recall	93.7 ± 3.0	94.0 ± 3.1
	Specificity	99.1 ± 0.2	99.6 ± 0.1
2	Accuracy	98.2 ± 0.3	98.5 ± 0.2
	Dice coefficient	93.9 ± 1.2	**95.1 ± 0.4**
	Precision	92.6 ± 2.2	94.1 ± 1.6
	Recall	95.1 ± 1.0	96.1 ± 0.9
	Specificity	98.8 ± 0.3	99.0 ± 0.3

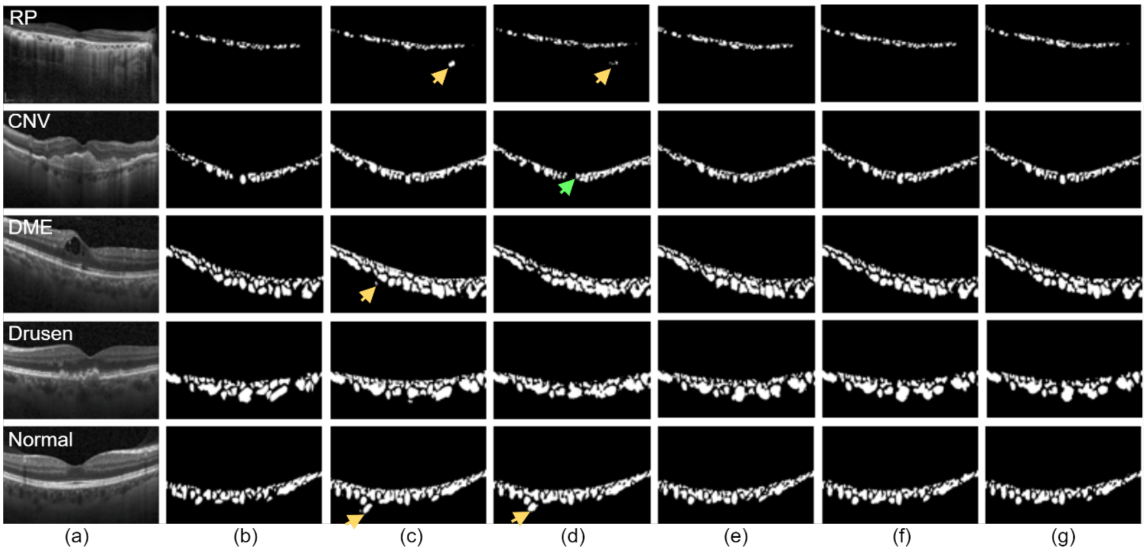

Figure 7.5 Choroidal vessel segmentation results. (a) Input, (b) ground truth, and results for (c) Ablation-1, (d) Ablation-2, (e) Ablation-3, (f) Ablation-4, and (g) ChoroidNET. (RP from Dataset-1, and CNV, DME, Drusen and Normal from Dataset-2)

Table 7.4 Performance comparison of choroidal vessel segmentation of ablation models and ChoroidNET (highest score in bold)

Dataset	Metric (mean ± SD)	Ablation-1	Ablation-2	Ablation-3	Ablation-4	ChoroidNET
1	Accuracy	98.4 ± 0.2	98.5 ± 0.2	98.4 ± 0.2	98.4 ± 0.2	98.5 ± 0.2
	Dice coefficient	80.5 ± 2.4	80.6 ± 1.0	80.2 ± 4.3	79.5 ± 3.3	**80.8 ± 1.9**
	Precision	78.1 ± 2.6	81.7 ± 2.6	78.6 ± 2.1	80.5 ± 2.9	79.3 ± 2.2
	Recall	**83.2 ± 3.4**	79.5 ± 1.5	82.0 ± 4.3	78.6 ± 6.3	82.3 ± 2.2
	Specificity	99.1 ± 0.2	99.3 ± 0.1	99.1 ± 0.1	99.2 ± 0.2	99.1 ± 0.1
2	Accuracy	96.9 ± 0.4	97.1 ± 0.4	97.5 ± 0.4	97.5 ± 0.4	97.7 ± 0.4
	Dice coefficient	78.7 ± 3.2	79.3 ± 2.2	81.5 ± 2.5	81.8 ± 2.5	**82.4 ± 2.4**
	Precision	68.6 ± 5.6	72.6 ± 4.4	76.2 ± 5.3	76.5 ± 5.4	78.2 ± 5.6
	Recall	**92.3 ± 2.2**	87.5 ± 2.1	87.5 ± 2.1	87.7 ± 1.9	87.2 ± 2.8
	Specificity	97.2 ± 0.4	97.8 ± 0.2	98.2 ± 0.3	98.2 ± 0.4	98.4 ± 0.4

7.3.3 Intra-observer viability of ChoroidNET

To assess intra-observer variability, our observer repeated the annotating process for the choroid layer and choroidal vessels. Dataset-2 was used for this comparison. Table 7.5 shows the variability between two sets of ground truths (GT1 and GT2) and ChoroidNET's segmentation. Intraclass correlation coefficient (ICC) was used to measure the variabilities. The ICC value of 1 indicates the highest agreement between the two observations. The intra-observer reproducibility of the choroid layer and vessel segmentation between GT1 and GT2 were excellent (Dice coefficient: 96.1 ± 1.1 and 84.1 ± 2.6) and (ICC: 0.983, 0.971). ChoroidNET also produced a high agreement with GT1 and GT2 (Dice coefficient: 95.1 ± 0.4, 95.1 ± 2.8) for choroid layer segmentation and (Dice coefficient: 82.4 ± 2.4, 82.1 ± 2.8) for choroidal vessel segmentation. Figure 7.6 shows ChoroidNET's segmentation results and their corresponding ground truths.

Table 7.5 Performance difference of inter-observer variability

	Metric (mean ± SD)	GT1 vs GT2	GT1 vs ChoroidNET	GT2 vs ChoroidNET
Layer	Accuracy	98.8 ± 0.3	98.5 ± 0.2	98.5 ± 0.8
	Dice coefficient	96.1 ± 1.1	95.1 ± 0.4	95.1 ± 2.8
	Precision	97.3 ± 1.5	94.1 ± 1.6	95.0 ± 4.8
	Recall	95.0 ± 2.6	96.1 ± 0.9	95.3 ± 3.2
	Specificity	99.5 ± 0.4	99.0 ± 0.3	99.1 ± 0.8
	ICC	0.983	0.955	0.964
Vessels	Accuracy	98.0 ± 0.8	97.7 ± 0.4	97.6 ± 0.9
	Dice coefficient	84.1 ± 2.6	82.4 ± 2.4	82.1 ± 2.8
	Precision	84.4 ± 4.5	78.2 ± 5.6	88.2 ± 3.1
	Recall	83.8 ± 3.0	87.2 ± 2.8	76.7 ± 5.1
	Specificity	98.9 ± 0.5	98.4 ± 0.4	98.2 ± 0.8
	ICC	0.971	0.840	0.861

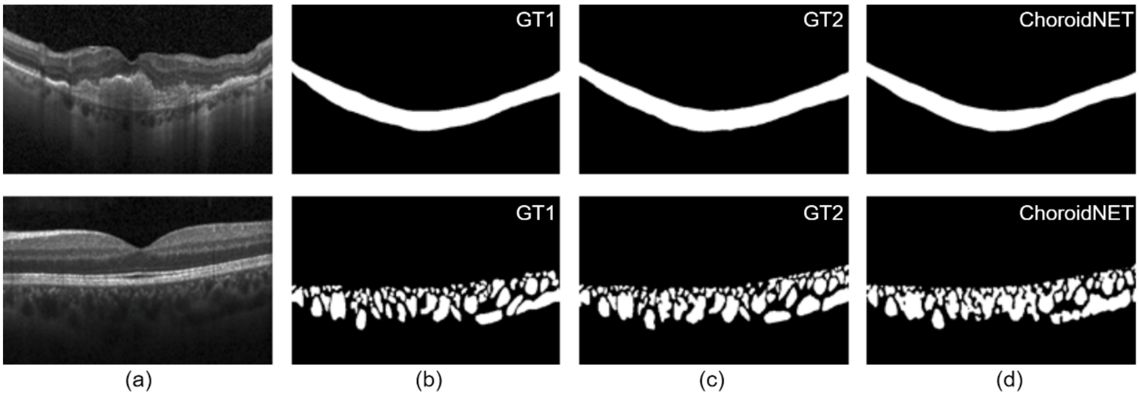

Figure 7.6 Intra-observer variability (a) Input, (b) ground truth (GT1), (c) ground truth (GT2), and (d) ChoroidNET result. (1st row – choroid layer and 2nd row – choroidal vessels)

7.3.4 Consistency of ChoroidNET

To validate our proposed network's consistency, we included 80 more images (20 images each from CNV, DME, Drusen, and Normal) from the source of Kermany et al. [115]. The proposed model was trained and validated on new training and test sets (40 images each). The training and validation processes were performed as in the previous training. We then compared the performances of two distinct trained models using two distinct test sets. Table 7.6 presents the quantitative performance of the proposed network for four sets. Set-1 corresponds to the results of the trained model-1 and the test set-1, set-2 corresponds to the results of the trained model-1 and the test set-2, set-3 corresponds to the results of the trained model-2 and the test set-1, and set-4 corresponds to the results of the trained model-2 and of test set-2, respectively. Figure 7.7 shows examples of the choroid layer and choroidal vessel segmentation results of test set-2. The mean Dice coefficients of four sets were 95.1 ± 0.4, 95.7 ± 0.5, 93.5 ± 1.3, 96.4 ± 0.5 for choroid layer segmentation, and 82.4 ± 2.4, 84.3 ± 0.3, 82.2 ± 2.1, 85.1 ± 0.2 for choroidal vessel segmentation. Thus, ChoroidNET showed consistent and good performance on newly tested CNV, DME, Drusen, and Normal images.

Table 7.6 Quantitative performance of ChoroidNET for four sets

	Metric (mean ± SD)	Set-1	Set-2	Set-3	Set-4
Layer	Accuracy	98.5 ± 0.2	99.0 ± 0.1	98.0 ± 0.4	99.1 ± 0.2
	Dice coefficient	95.1 ± 0.4	95.7 ± 0.5	93.5 ± 1.3	96.4 ± 0.5
	Precision	94.1 ± 1.6	97.3 ± 0.3	89.8 ± 2.9	97.1 ± 0.8
	Recall	96.1 ± 0.9	94.1 ± 0.9	97.6 ± 0.8	95.7 ± 0.8
	Specificity	99.0 ± 0.3	99.6 ± 0.1	98.1 ± 0.5	99.6 ± 0.1
Vessels	Accuracy	97.7 ± 0.4	98.3 ± 0.2	97.7 ± 0.4	98.4 ± 0.2
	Dice coefficient	82.4 ± 2.4	84.3 ± 0.3	82.2 ± 2.1	85.1 ± 0.2
	Precision	78.2 ± 5.6	81.1 ± 1.9	79.2 ± 5.7	83.8 ± 1.2
	Recall	87.2 ± 2.8	87.8 ± 1.9	85.4 ± 3.7	86.5 ± 1.7
	Specificity	98.4 ± 0.4	98.9 ± 0.1	98.5 ± 0.4	99.1 ± 0.1

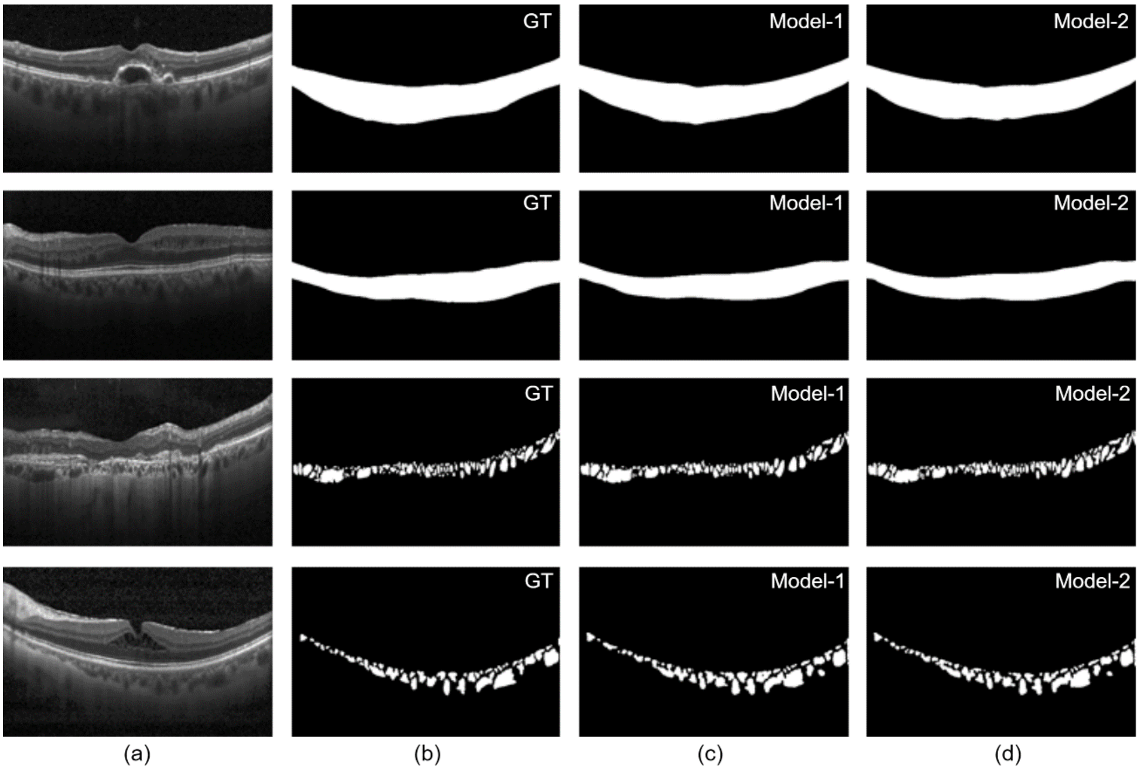

Figure 7.7 Choroid layer and vessel segmentation results of ChoroidNET using test set-2. (a) Input, (b) ground truth, (c) model-1, and (d) model-2. (1st and 2nd rows – choroid layer and 3rd and 4th rows – choroidal vessels)

7.3.5 Measurement of choroidal parameters

Statistical analysis was performed to assess agreement between two measures based on ChoroidNET's segmentation and the ground truths. Dataset-1 (retinitis pigmentosa dataset) was used for this analysis. Four statistical measures such as the mean of the difference (expressed as mean ± SD), 95% limits of agreement (LOA) (defined as [lower LOA, upper LOA], intraclass correlation coefficient (ICC), and Pearson's correlation (R) were calculated. 95% LOA is defined by mean ± 1.96 SD. ICC is used to access the reliability of measurement scales. It contains information on the correlation and the systematic difference between the two measures [118]. Thus, ICC is more advantageous than R. Both correlations range from 0 to 1. The value of 0 indicates no reliability, and 1 shows perfect reliability. The level of reliability can be interpreted according to the correlation values, (<0.50) as poor, (>0.5 and <0.75) as moderate, (>0.75 and <0.9) as good, and (>0.9) as excellent.

Table 7.7 shows the difference assessments between the results of the deep learning segmentation models (U-Net++, DRUNET, Residual U-Net, and ChoroidNET) and the ground truths. The difference between the two measures (Segmentation - Ground Truth) is calculated in millimeters (mm). The proposed method had the best ICC values (0.961, 0.940, 0.916) for TCA, LA, and CT. U-Net++ measurement had the best ICC value (0.840) for SA.

To present the agreement between measurements graphically, Pearson's correlation was plotted in Figure 7.8. The scatter plots show linear relations between two measurements based on the deep learning segmentation (x-axis) and the ground truths (y-axis).

Table 7.7 Difference assessment between deep learning segmentation and the ground truths

Parameters	Metric	U-Net++	DRUNET	Residual U-Net	ChoroidNET
TCA (mm^2)	mean ± SD	-0.012 ± 0.024	-0.016 ± 0.040	-0.010 ± 0.028	-0.006 ± 0.024
	95% LOA	[-0.060, 0.035]	[-0.094, 0.062]	[-0.065, 0.045]	[-0.054, 0.040]
	ICC	0.948	0.877	0.938	**0.961**
	R	**0.973**	0.899	0.959	0.969
LA (mm^2)	mean ± SD	-0.003 ± 0.019	-0.001 ± 0.021	-0.012 ± 0.021	0.004 ± 0.016
	95% LOA	[-0.041, 0.034]	[-0.043, 0.040]	[-0.054, 0.030]	[-0.028, 0.036]
	ICC	0.919	0.913	0.861	**0.940**
	R	0.928	0.911	0.917	**0.948**
SA (mm^2)	mean ± SD	-0.008 ± 0.024	-0.013 ± 0.035	0.003 ± 0.026	-0.010 ± 0.025
	95% LOA	[-0.054, 0.038]	[-0.082, 0.056]	[-0.049, 0.054]	[-0.058, 0.039]
	ICC	**0.840**	0.639	0.830	0.826
	R	**0.889**	0.697	0.846	0.867
CT (mm)	mean ± SD	-0.012 ± 0.028	-0.009 ± 0.034	-0.010 ± 0.032	-0.004 ± 0.023
	95% LOA	[-0.067, 0.042]	[-0.076, 0.058]	[-0.073, 0.053]	[-0.048, 0.040]
	ICC	0.851	0.805	0.813	**0.916**
	R	0.889	0.825	0.848	**0.931**

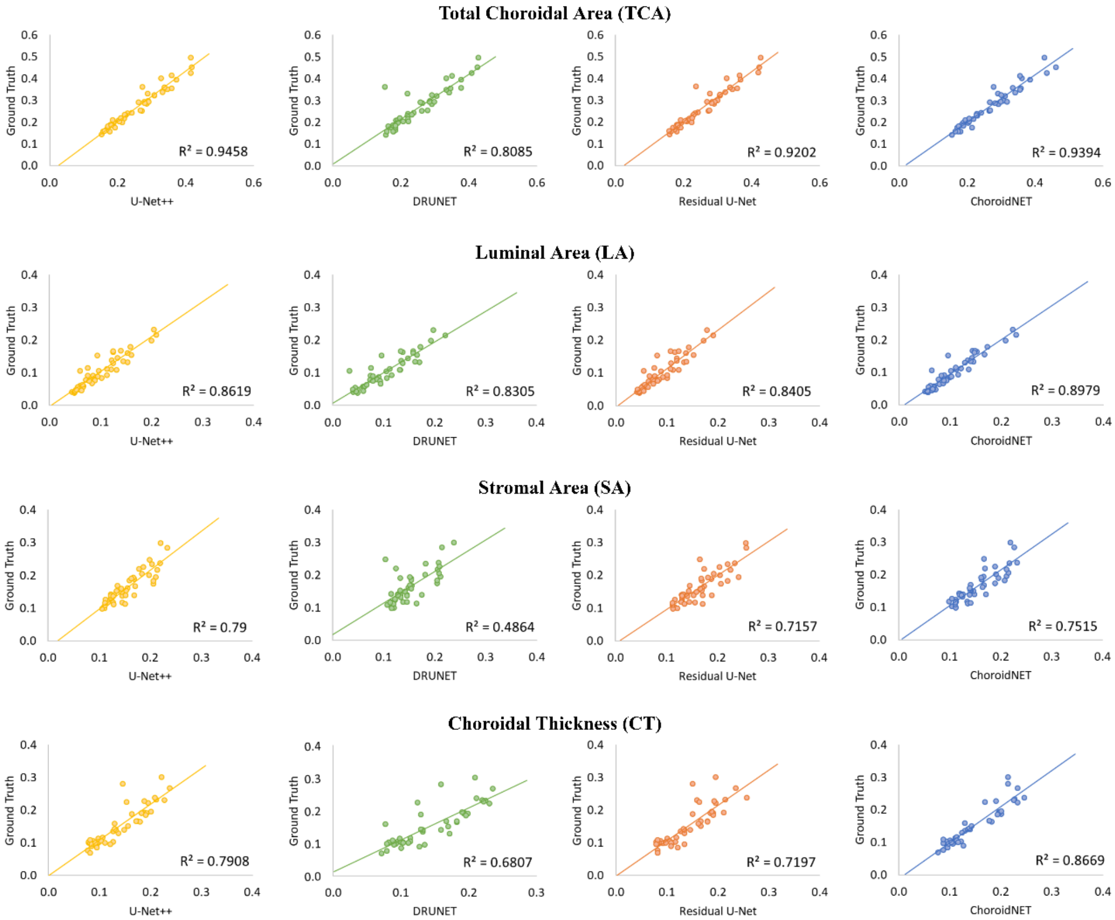

Figure 7.8 Correlation between two measurements based on the deep learning segmentation and the ground truths.

7.4 Summary and discussion

This work presents the choroid layer and vessel segmentation in retinal OCT images using ChoroidNET, a dense-dilated U-Net model. We performed a qualitative and quantitative segmentation analysis of the choroid layer and choroidal vessels. The experimental results in Tables 7.1 and 7.2 confirm that ChoroidNET is the best state-of-the-art model for segmenting the choroid layer and choroidal vessels.

In an eye with DME, an accumulation of fluid with cystic properties usually occurs in the retinal layers. In an OCT image, those accumulated fluid regions are similar to the characteristics of choroidal vessels. For DME images, U-Net++ and Residual U-Net had inconsistent vessel segmentation performance compared to DRUNET and ChoroidNET. The objective of the standard convolutions in U-Net++ and Residual U-Net is to extract the spatial information in the image. A deeper network can learn more semantic information. However, spatial information is lost at deeper layers; thus, the network predicts incorrect regions outside the choroid layer. Dilated convolutions reduce the loss of spatial data by expanding the receptive field of the network. Thus, the dilated convolutions in DRUNET and ChoroidNET facilitate the creation of large-scale feature maps with rich spatial information. The segmentation performance of DRUNET and ChoroidNET is, therefore, more consistent for DME images.

In the U-Net architecture, the number of filters is doubled after down-sampling in the encoder path and halved after up-sampling in the decoder path. However, in the DRUNET architecture, only 16 filters are used in both standard and residual blocks. DRUNET thus had poor vessel segmentation performance for CNV and Drusen images. The filter of a convolutional layer captures the patterns in image data. A higher number of filters allows the network to learn more complex patterns (abstractions) in image data and extract useful features. As a result, DRUNET could not separate the choroid pattern from the neovascular membrane in CNV images and mistakenly segmented small drusen (which occurs in the complex between RPE and the choroid) as the choroidal vessels. U-Net++, Residual U-Net, and ChoroidNET use a high number of filters (the same as that in U-Net), which considerably improves the recognition and segmentation of the choroid layer and vessels.

For Dataset-1, the segmentation performance of all models is generally similar and consistent with the ground truths. U-Net++, DRUNET, and Residual U-Net are sensitive to the pathologies (subretinal and intraretinal fluid) present in CNV, DME, and Drusen images. In contrast, there is no significant difference in the segmentation performance of ChoroidNET for CNV, DME, Drusen, and Normal images.

The number of parameters a network uses depends on the number of filters. ChoroidNET and Residual U-Net each use approximately 4.5 million parameters (compared to 2.2 million for U-Net++ and only 40,000 for DRUNET) and thus have a much higher computational cost and use much more memory. This is a significant drawback of ChoroidNET.

We tested the performance of ChoroidNET using two datasets from different OCT sources (EDI-OCT and SD-OCT). EDI-OCT allows enhanced visualization of choroids compared to SD-OCT. However, ChoroidNET shows no performance degradation for SD-OCT images, regardless of the enhanced visibility of the choroid.

We also evaluated the segmentation performance of ChoroidNET based on the prediction scores of the receiver operator characteristics area under the curve (ROC-AUC) and the precision-recall area under the curve (PR-AUC). ROC-AUC indicates the tradeoff between the true positive rate and the false-positive rate. PR-AUC represents the tradeoff between precision and recall. Table 7.8 shows the ROC-AUC and PR-AUC scores for the choroid layer and choroidal vessel segmentation. The range of scores is [0, 1]. A higher score indicates a better model performance.

Table 7.8 ROC-AUC and PR-AUC scores of ChoroidNET's layer and vessel segmentation

Dataset	AUC Score (mean ± SD)	Layer	Vessels
1	ROC-AUC	0.998 ± 0.002	0.993 ± 0.004
	PR-AUC	0.987 ± 0.009	0.878 ± 0.020
2	ROC-AUC	0.997 ± 0.001	0.992 ± 0.001
	PR-AUC	0.989 ± 0.002	0.906 ± 0.018

In summary, ChoroidNET significantly outperforms U-Net++, DRUNET, and Residual U-Net and is robust for images with various pathologies and different OCT types. In addition, it provides a good tradeoff between the true positive rate and false positive rate and between precision and recall for both choroid layer and choroidal segmentation. ChoroidNET is thus the most robust model.

With the performance of ChoroidNET, our measurement technique obtained the ICC values of TCA (0.961), LA (0.940), SA (0.826), and CT (0.916). In general, the proposed measurement offers a high level of agreement and excellent reliability, especially for TCA, LA, and CT, which are the most widely used parameters in the quantitative assessments of previous clinical research.

Chapter 8

Conclusion and future perspectives

Chapter 8 Conclusion and future perspectives

This chapter summarizes the principal outcomes of this thesis in Section 8.1 and describes the future works and other possible contributions related to our results in Section 8.2.

8.1 Thesis summary and other perspectives

8.1.1 Optic disc and optic disc edema segmentation in retinal fundus images

Several state-of-the-art methods reported a highly competitive success rate for detecting and segmenting retinal images captured by standard ophthalmic devices. Those methods usually fail to correctly see the optic disc (OD) in the mobile-phone retinal pictures characterized by a narrower field of view with poorer quality, having artifacts such as pale blurring of the OD area and external light reflections, incomplete vascular network, and reduced brightness and contrast. More, the abnormalities of retinal diseases combined with the characteristics mentioned above of mobile-phone images make OD detection more challenging.

Optic disc edema (ODE) is an essential ocular manifestation in neuro-ophthalmic diseases. The presence of ODE is recommended to detect at an early stage to avoid life-threatening visual impairments. ODE area was suggested as a reliable index to evaluate the stage (severity) of ODE. Retinal images with ODE have different textures from a standard OD and have abnormal characteristics such as blurring and enlargement of OD and obscuration of veins. Although many OD detection methods have been proposed for retinal images with glaucoma and diabetic retinopathy (DR), the ways to detect and segment ODE are rarely found.

A new automatic hybrid OD localization method (HLM) was proposed for the images of eyes with DR. The principle of our previously proposed exclusion method (EM) is simple. It detects that location where significantly fewer vessels are oriented horizontally than vertically as an OD. However, the accuracy of EM is low for DR images since the blood vessels in the retina usually distort and swell in the eyes with DR. HLM improved the OD detection accuracy by combining EM and a new line detection method (LDM). HLM analyzes the vascular network pattern and detects the OD location using EM when an image has a complete vessel network and LDM otherwise. Despite the presence of DR, HLM located the OD precisely with average accuracies of 98% for mobile-phone camera datasets (Exudate, Hemorrhage, and Healthy) and 93.53 % for standard retinal datasets (STARE, ROP, DIARETDB0, and DIARETDB1). It detected the locations of ODE with a high success rate of 97.14%.

An active contour model has been applied to segment the OD boundary for OD segmentation. However, the model is sensitive to artifacts acquired while a mobile phone imagines. To obtain a better OD segmentation performance, we refined by applying a simple thresholding step with a threshold of the pixel intensity value of the OD location obtained from the HLM. The entire process is denoted as HLM-ACCF. The HLM-ACCF received an average precision of 94.10%, an average recall of 80.23%, and an average F-measure of 86.61% for three mobile-phone datasets.

The HLM-ACCF method does not work well for images with ODE because the texture of the swelling area appears featureless compared to a standard OD. To tackle that, the factorization-based active contour (FAC) was applied for the ODE segmentation method based on an image texture feature. We tested the HLM-FAC using 35 ODE images and evaluated the segmentation performance against several existing methods. Comparisons indicate that the proposed method could segment ODE areas with the highest F-measure of 84.24%. Finding the ODE area is essential in the ODE severity grading process. Thus, our work can also be applied in an ODE grading/classification system to yield more precise results.

8.1.2 Analysis of choroidal structures in retinal OCT images

The choroid is a vascular layer of the eye and one of the significant sources of blood supply to the retina. It is involved in the pathogenesis of various ocular diseases. Understanding the choroidal changes plays a prominent role in visual health assessment. Accurate segmentation of the choroid layer and choroidal vessels is an initial task important for precisely measuring the choroidal features. The proposed ChoroidNET is a dense-dilated model that adopts the architecture of U-NET. It comprises two modules, the layer segmentation module and the vessel segmentation module for segmenting the choroid layer and choroidal vessels.

The performance of ChoroidNET is evaluated using two OCT datasets. Overall Dice coefficients of (94.9 ± 1.5, 95.1 ± 0.4) for choroid layer segmentation and (80.8 ± 1.9, 82.4 ± 2.4) for choroidal vessel segmentation were obtained using two datasets, respectively. The numerical results showed that ChoroidNET outperforms U-Net++, DRUNET, and Residual U-Net, and is robust to cases of pathological abnormality (i.e., neovascular membrane and associated subretinal fluid in images with choroid neovascularization, retinal-thickening-associated intraretinal fluid in images with diabetic macular edema, and multiple drusen).

In this work, we presented an automatic measurement of choroidal features in OCT images of eyes with retinitis pigmentosa (RP) based on ChoroidNET segmentation. We measured four choroidal features (total choroidal area, luminal area, stromal area, and choroidal thickness) in OCT images of RP eyes. We proved that our proposed ChoroidNET-based measurement achieved a high level of agreement between the ground truths. Since RP is a progressive disorder, ophthalmologists must monitor choroidal alterations over time. Currently, we are analyzing the changes in choroidal structure for a natural course of RP.

Further, the loss of the ellipsoid zone is one of the significant signs in RP patients. A natural course analysis of RP over a three-year interval reported that the length of the ellipsoid zone at the baseline was significantly correlated with the annual decrease in retinal sensitivity [119]. The analysis of the ellipsoid area is one of the possible contributions to future scope. The segmentation of other retinal layers and the sclera should be considered in future studies because the pathologies of different tissues in the retina are essential for diagnosing diseases such as Alzheimer's [120], age-related macular degeneration, DR, and scleritis.

8.2 Recommendation for future work

8.2.1 Image enhancement for mobile-phone retinal images

There are some limitations in our OD detection work. We tested adaptive histogram equalization as a pre-processing technique for mobile-phone retinal datasets before applying the HLM. The localization accuracy of HLM is reduced by 2% for the Exudate and Hemorrhage datasets. The F-measure of HLM-ACCF is reduced by 9.3% for Exudate, 3.98 for Hemorrhage, and 2.49% for Healthy. The detected OD location from the HLM is essential for the HLM-ACCF to obtain an accurate OD boundary. The Exudate and Hemorrhage datasets contain the pathological features of DR, i.e., exudates and hemorrhages that can be misclassified as an OD. We observed that classical enhancement methods are not efficient as applied to mobile-phone retinal images, which are distorted by reflections of the light and uneven contrast. An example case performed by the proposed algorithms with and without enhancement is shown in Figure 8.1. The loss of detected vessels around the OD region is a cause that the detection method fails.

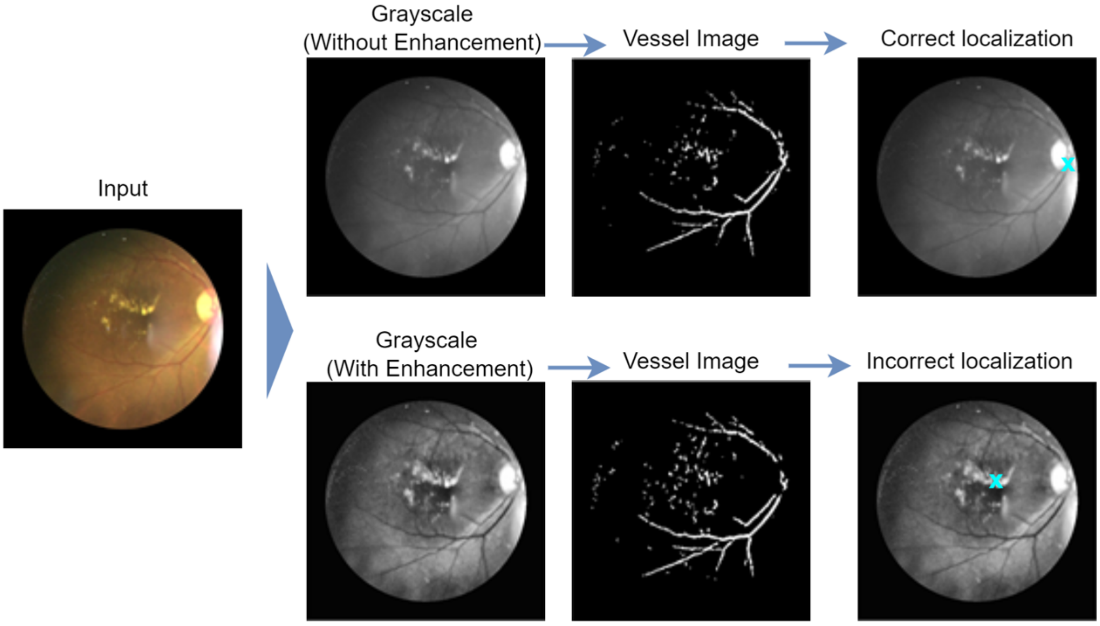

Figure 8.1 HLM with and without applying an enhancement technique.

Therefore, an appropriate pre-processing technique that applies to mobile-phone images is an open problem, and the issues stated should be considered subjects of future research. The proposed OD detection methods can be extended to find other components such as fovea and macula and abnormalities in the retina such as exudates and hemorrhages. The proposed OD segmentation methods can also be extended in object segmentation research.

8.2.2 Post-processing technique for ChoroidNET results

Dataset1 (retinitis pigmentosa dataset) contains some images with weak edges in the choroid region. Since the boundaries of the choroid are almost invisible in some cases, ChoroidNET produces the irregular lower border of the choroid. We will implement a post-processing technique in our future works, to refine irregular boundaries to be smooth and natural. With the refined results, our measurement results would be more accurate and better applicable in analyzing changes in the choroid for monitoring treatment outcomes or long-term course studies of RP diseases.

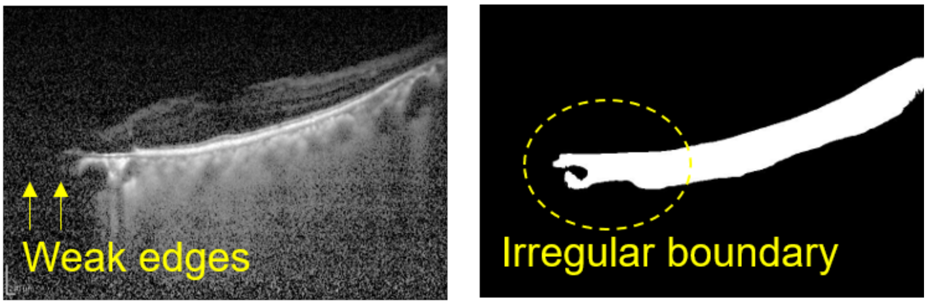

Figure 8.2 (a) An OCT image with weak edges and (b) irregular boundary resulting from ChoroidNET.

8.2.3 Possible applications and extensions of research

The possible applications and tentative extensions of this research can be summarized as follows.

- **Analysis of retinal changes in POEMS Syndrome**

  POEMS syndrome is a rare multisystemic disease caused by an underlying plasma cell disorder. POEMS stands for polyneuropathy, organomegaly, endocrinopathy, monoclonal plasma cells, and skin changes. It affects the whole body including the retinal nerves. There is a diagnostic criterion to diagnose POEMS syndrome. One of its minor criteria is the presence of papilledema (also known as optic disc edema). One of its major criteria includes the increase in vascular endothelial growth factor that can result in choroidal thickening. We can analyze the ODE area and choroidal features using our proposed segmentation and measurement techniques. Therefore, analyzing changes in the optic disc area and the choroid in POEMS syndrome is one of the possible applications that can extend from this thesis.

- **Multi-modal analysis of retinal changes**

  Current widely-used imaging modalities in ophthalmology include fundus photography, OCT, OCT angiography, fluorescein angiography, scanning laser ophthalmoscopy, indocyanine green angiography, and photoacoustic microscopy advances from the laser and optical imaging. Each modality can offer advantages and disadvantages in visualizing retinal tissues and vasculature over others. Combining one or more modalities can provide several benefits and be co-registered with one another. Multi-modal analysis of retinal changes is recommended to evaluate retinal diseases better.

- **Analysis of other neural retinal layers and sclera**

  The ChoroidNET model can also be extended to segment the neural retinal layers and RPE. Investigating other tissues in the retina can provide multiple perspectives in the diagnosis since the pathologies of those areas are also important for diagnosing diseases such as age-related macular degeneration, CNV, and other neurodegenerative diseases such as Alzheimer's disease.

References

[1] Vision Loss Expert Group of the Global Burden of Disease Study (2021) “Trends in prevalence of blindness and distance and near vision impairment over 30 years: an analysis for the Global Burden of Disease Study,” *The Lancet of Global Health*, vol. 9, pp. 130–143.

[2] Y. Morizane, N. Morimoto, A. Fujiwara, R. Kawasaki, H. Yamashita, Y. Ogura, and F. Shiraga (2019) “Incidence and causes of visual impairment in Japan: the first nation-wide complete enumeration survey of newly certified visually impaired individuals,” *Japanese Journal of Ophthalmology*, vol. 63, pp. 26–33.

[3] M. Egawa, Y. Mitamura, M. Niki, H. Sano, G. Miura, A. Chiba, S. Yamamoto, S. Sonoda, and T. Sakamoto (2019) “Correlations between choroidal structures and visual functions in eyes with retinitis pigmentosa,” *Retina, Journal of Retinal and Vitreous Diseases*, vol. 39, no. 12, pp. 2399–2409.

[4] D. Huang, E. A. Swanson, C. P. Lin, J. S. Schuman, W. G. Stinson, W. Chang, M. R. Hee, T. Flotte, K. Gregory, C. A. Puliafito, and J. G. Fujimoto (1991) “Optical coherence tomography,” *Science,* vol. 254, no. 5035, pp. 1178–1181.

[5] G. J. Jaffe and J. Caprioli (2004) “Optical coherence tomography to detect and manage retinal disease and glaucoma,” *American Journal of Ophthalmology,* vol. 137, no. 1, pp. 156–169.

[6] T. Sezer, M. Altinisik, A. K. Koytak, and M. H. Ozdemir (2016) “The choroid and optical coherence tomography,” *Turkish Journal of Ophthalmology,* vol. 46, pp. 30–37.

[7] R. F. Spaide, H. Koizumi, and M. C. Pozonni (2008) “Enhanced depth imaging spectral-domain optical coherence tomography,” *American Journal of Ophthalmology*, vol. 146, no. 4, pp. 496–500.

[8] Z. Zhang, R. Srivastava, H. Liu, X. Chen, L. Duan, D. W. K. Wong, C. K. Kwoh, T. Y. Wong, and J. Liu (2014) “A survey on computer-aided diagnosis for ocular diseases,” *BMC Medical Informatics and Decision Making*, vol. 14, Article No. 80.

[9] A. Hoover and M. Goldbaum (2003) “Locating the optic nerve in a retinal image using the fuzzy convergence of the blood vessels,” *IEEE Transactions on Medical Imaging*, vol. 22, pp. 951–958.

[10] N. Hommer, M. Kallab, Y. C. Sim, A. Lee, J. Chua, B. Tan, A. Schlatter, R. M. Werkmeister, D. Schmidl, L. Schmetterer, and G. Garhofer (2021) “Effect of hyperoxia and hypoxia on retinal vascular parameters accessed with optical coherence tomography angiography,” *ACTA Ophthalmologica*, DOI: 10.1111/aos.15077.

[11] R. Xie, B. Qiu, J. Chhablani, and X. Zhang (2021) “Evaluation of choroidal thickness using optical coherence tomography: A review,” *Frontiers in Medicine*, vol. 8, Article 783519, DOI: 10.3389/fmed.2021.783519.

[12] S. R. Singh, K. K. Vupparabonia, A. Goud, B. Sopt, K. K. Dansingari, and J. Chhablani (2019) "Choroidal imaging biomarkers," *Survey of Ophthalmology*, vol. 64, pp. 312–333.

[13] G. Yiu, S. J. Chiu, P. A. Petrou, E. Y. Chew, W. T. Wong, and C. A. Toth (2015) "Relationship of central choroidal thickness with age-related macular degeneration status," *American Journal of Ophthalmology*, vol. 159, no. 4, pp. 617–626.

[14] S. E. Chung, S. W. Kang, J. H. Lee, and Y. T. Kim (2011) "Choroidal thickness in polypoidal choroidal vasculopathy and exudative age-related macular degeneration," *American Academy of Ophthalmology*," vol. 118, pp. 840–845.

[15] S. Kuroda, Y. Ikuno, Y. Yasuno, K. Nakai, S. Usui, M. Sawa, M. Tsujikawa, F. Gomi, and K. Nishida (2013) "Choroidal thickness in central serous chorioretinopathy," *Retina*, vol. 33, no. 2, pp. 302–308.

[16] A. Invernizzi, E. Benatti, M. Cozzi, S. Erba, S. Vaishnavi, K. K. Vupparaboina, G. Staurenghi, J. Chhablani, M. Gillies, and F. Viola (2018) "Choroidal structural changes correlate with neovascular activity in neovascular age-related macular degeneration," *Investigative ophthalmology & visual science (iovs)*, vol. 59(10), pp. 3836–3841.

[17] R. Nourinia, H. Ahmadieh, E. Nekoei, P. Malekifar, and Z. Tofighi (2018) "Changes in central choroidal thickness after treatment of diabetic macular edema with intravitreal bevacizumab correlation with central macular thickness and best correlated visual acuity," *Retina*, vol. 38, no. 5, pp. 970–97.

[18] D. S. Dhoot, S. Huo, A. Yuan, D. Xu, S. Srivistava, J. P. Ehlers, E. Traboulsi, and P. K. Kaiser (2013) "Evaluation of choroidal thickness in retinitis pigmentosa using enhanced depth imaging optical coherence tomography," *British Journal of Ophthalmology*, vol. 99, pp. 66–69.

[19] R. Tan, R. Agrawal, S. Taduru, A. Gupta, K. Vupparabonia, and J. Chhablani (2018) "Choroidal vascularity index in retinitis pigmentosa: An OCT study," *Ophthalmic Surgery, Lasers and Imaging Retina*, vol. 49, pp. 191–197.

[20] A. Allam, A. Youssif, and A. Ghalwash (2015) "Automatic segmentation of optic disc in eye fundus images: A survey," *Electronic Letters on Computer Vision and Image Analysis*, vol. 14, pp. 1–20.

[21] A. Almazroa, R. Burman, K. Raahemifar, and V. Lakshminarayanan (2015) "Optic disc and optic cup segmentation methodologies for glaucoma image detection: A survey," *Journal of Ophthalmology* vol. 2015, Article ID 180972, DOI: 10.1155/2015/180972.

[22] N. Thakur and M. Juneja (2018) "Survey on segmentation and classification approaches of optic cup and optic disc for diagnosis of glaucoma," *Biomedical Signal Processing and Control*, vol. 42 pp. 162–189.

[23] H. N. Veena, A. Muruganandham, and T. S. Kumaran (2020) “A review on the optic disc and optic cup segmentation and classification approaches over retinal fundus images for detection of glaucoma,” *Springer Nature Applied Sciences*, 2:1476, DOI.

[24] F. Abdullah, R. Imtiaz, H. A. Madni, H. A. Khan, T. M. Khan, M. A. U. Khan, and S. S. Naqvi (2021) “A review in glaucoma disease detection using computerized techniques,” *IEEE Access*, vol. 9, pp. 37311–37333.

[25] N. M. Noor, N. E. A. Khalid, and N. M. Ariff (2013) “Optic cup and disc color channel multi-thresholding segmentation,” *IEEE International Conference on Control System, Computing and Engineering*, pp 530–534.

[26] T. Ruennark, P. Aimmanee, S. S. Makhanov, N. Kanchanaranya, and S. Vongkittiruk (2019) “Alternative deflation-inflation gradient vector flow snakes for prescreening glaucoma in mobile phone retinal images,” *In Proceedings of the 23rd International Computer Science and Engineering Conference (ICSEC)*, pp. 135–140.

[27] P. C. Siddalingaswamy and P. K. Gopalakrishna (2010) “Automatic localization and boundary detection of optic disc using implicit active contours,” *International Journal of Computer Applications*, 0975–8887, vol. 1, no. 7.

[28] M. Esmaeili, H. Rabbani, and A. M. Dehnavi (2012) “Automatic optic disk boundary extraction by the use of curvelet transform and deformable variational level set model,” *Pattern Recognition*, vol. 45, pp. 2382–2842.

[29] Y. Wang, X. Yu, J. Chi, and C. Wu (2019) “Automatic segmentation of optic disc and cup in retinal fundus images using improved two-layer level set method,” *Mathematical Problems in Engineering*, vol. 2019, Article ID. 4836296.

[30] S. S. Naqvi, N. Fatima, T. Khan, Z. U. Rehman, and M. A. Khan (2019) “Automatic optic disk detection and segmentation by variational active contour estimation in retinal fundus image,” *Signal, Image and Video Processing*, vol. 13, pp. 1191–1198.

[31] Y. Gao, X. Yu, C. Wu, W. Zhou, X. Wang, and H. Chu (2019) “Accurate and efficient segmentation of optic disc and optic cup in retinal images integrating multi-view information,” *IEEE Access*, vol. 7, pp. 148183–148197.

[32] F. Yin, J. Liu, D. W. K. Wong, N. M. Tan, C. Cheung, M. Baskaran, T. Aung, and T. Y. Wong (2012) “Automated segmentation of optic disc and optic cup in fundus images for glaucoma diagnosis,” *25th IEEE International Symposium on Computer-Based Medical Systems*, doi:10.1109/cbms.2012.6266344.

[33] Z. U. Rehman, S. S. Naqvi, T. M. Khan, M. Arsalan, M. A. Khan, and M. A. Khalil (2019) “Multi-parametric optic disc segmentation using superpixel based feature classification,” *Expert Systems with Applications*, vol. 120, pp. 461–473.

[34] B. Gui, R. Shuai, and P. Chen (2018) “Optic disc localization algorithm based on improved corner detection,” *Procedia Computer Science*, vol. 131, pp. 311–319.

[35] L. C. Rodrigues and M. Marengoni (2017) “Segmentation of optic disc and blood vessels in retinal images using wavelets, mathematical morphology, and Hessian-based multi-scale filtering,” *Biomedical Signal Processing and Control*, vol. 36, pp. 39–49.

[36] A. Sopharak, K. T. Nwe, Y. A. Moe, and M. N. Dailey (2008) “Automatic exudate detection with a naive Bayes classifier,” *International Conference on Embedded Systems and Intelligent Technology*, pp 139–142.

[37] J. Rahebi and F. Hardalaç (2016) “A new approach to optic disc detection in human retinal images using the firefly algorithm,” *Medical & Biological Engineering & Computing*, vol. 54, pp. 453–461.

[38] S. Abed, S. A. Al-Roomi, and M. Al-Shayeji (2016) “Effective optic disc detection method based on swarm intelligence techniques and novel pre-processing steps,” *Applied Soft Computing*, vol. 49, pp. 146–163.

[39] S. Lu (2011) “Accurate and efficient optic disc detection and segmentation by a circular transformation,” *IEEE Transactions on Medical Imaging*, vol. 30, pp. 2126–2133.

[40] A. R. Youssif, A. Z. Ghalwash, and A. R. Ghoneim (2008) “Optic disc detection from normalized digital fundus images by means of a vessels' direction matched filter,” *IEEE Transactions on Medical Imaging*, vol. 27, pp. 11–18.

[41] A. E. Mahfouz and A. S. Fahmy (2010) “Fast localization of the optic disc using projection of image features,” *IEEE Transactions on Image Processing*, vol. 19, no. 12, pp. 3285–3289.

[42] M. Lalonde, M. Beaulieu, and L. Gagnon (2001) “Fast and robust optic disc detection using pyramidal decomposition and Hausdorff-based template matching,” *IEEE Transactions on Medical Imaging*, vol. 20, pp. 1193–1200

[43] A. S. Abdullah, J. Rahebi, Y. E. Ozak, and M. Aljanabi (2020) “A new and effective method for human retina optic disc segmentation with fuzzy clustering method based on active contour model,” *Medical & Biological Engineering & Computing*, vol. 58, pp. 25–37.

[44] N. Thakur and M. Juneja (2019) “Optic disc and optic cup segmentation from retinal images using hybrid approach,” *Expert Systems with Applications*, vol. 127, pp. 308–322.

[45] T. M. Khan, M. Mehmood, S. S. Naqvi, and M. F. U. Butt (2020) “A region growing and local adaptive thresholding-based optic disc detection,” *PLoS ONE*, 15(1): e0227566, DOI: 10.1371/journal. pone.0227566.

[46] N. Muangnak, P. Aimmanee, S. Makhanov, and B. Uyyanonvara (2015) “Vessel transform for automatic optic disk detection in retinal images,” *IET Image Processing*, vol. 9, pp. 743–750.

[47] C. Duanggate, B. Uyyanonvara, S. Makhanov, and S. Barman (2011) “Parameter-free optic disc detection,” *Computerized Medical Imaging and Graphics*, vol. 35, pp. 51–63.

[48] N. Muangnak, P. Aimmanee, and S. Makhanov (2018) “Automatic optic disk detection in retinal images using hybrid vessel phase portrait analysis,” *Medical & Biological Engineering & Computing*, vol. 56, pp. 583–598.

[49] R. Besenczi, K. Szitha, B. Harangi, and A. Csutak (2015) “Automatic optic disc and optic cup detection in retinal images acquired by mobile phone,” *Ninth International Symposium on Image and Signal Processing and Analysis (ISPA)*, pp. 193–198. DOI: 10.1109/ISPA.2015.7306057.

[50] G. P. Van Stavern (2007) “Optic disc edema,” *Seminars in Neurology*, vol. 27, pp. 233–243.

[51] S. Urfalioglu, G. Ozdemir, M. Guler, and G. G. Duman (2021) “The evaluation of patients with optic disc edema: A retrospective study,” *Nothern Clinics of Istanbul*, vol. 8, no. 3, pp. 280–285.

[52] S. Akbar, M. U. Akram, M. Sharif, A. Tariq, and U. Yasin (2017) “Decision support system for detection of papilledema through fundus retinal images,” *Journal of Medical Systems*, 41:66.

[53] T. Saba, S. Akbar, H. Kolivand, and S. A. Bahaj (2021) “Automatic detection of papilledema through fundus retinal images using deep learning,” *Microscopy, Research and Technology*, vol. 84, pp. 3066–3077.

[54] L. Liu, X. Zhang, H. Zhao, X. Gao, D. Zhou, R. Dai, and J. Li (2020) “Reliability of optic disc edema in estimating of the severity of papilledema in patients with POEMS syndrome,” *Orphanet Journal of Rare Diseases*, 15:116.

[55] A. Usman, S. A. Khitran, M. U. Akram, and Y. Nadeem (2014) “A robust algorithm for Optic disc segmentation from colored fundus images,” *Proceeding in International Conference on Image Analysis and Recognition*, pp. 303–310.

[56] A. A. Salam, T. Khalil, M. U. Akram, A. Jameel, I. Basit (2016) “Automated detection of glaucoma using structural and non structural features,” *Springerplus*, 5(1):1519.

[57] N. Otsu (1979) “A threshold selection method from gray-level histograms,” *IEEE Transactions on Systems, Man, and Cybernetics*, *vol.* 9, pp. 62–66.

[58] T. T. Khaing and P. Aimmanee (2017) “Optic disk localization using exclusion method,” *Twelfth International Conference on Knowledge, Information and Creativity Support Systems* (KICSS2017), ISBN-13: 978-4815008147. pp 126–131.

[59] D. Duan D, M. Xie, Q. Mo, and Z. Han (2010) “An improved Hough transform for line detection,” *International Conference on Computer Application and System Modeling*, pp 354–357, DOI: 10.1109/ICCASM.2010.5620827.

[60] R. O. Duda and P. E. Hart (1972) “Use of the Hough transformation to detect lines and curves in picture,” *Communications of the ACM*, vol. 15, pp. 11–15

[61] M. Hall, E. Frank, G. Holmes, and B. Pfahringer (2009) “The WEKA data mining software: an update,” *SIGKDD Explorations*, vol. 11, pp. 10–18.

[62] T. F. Chan and L. A. Vese (2001) "Active contours without edges," *IEEE Transactions on Image Processing*, vol. 10, pp. 266–277.

[63] C. Kimme, D. Ballard, J. Sklansky (1975) "Finding circles by an array of accumulators," *Communications of the ACM*, vol. *18*, pp. 120–122.

[64] S. Echegaray, G. Zamora, H. Yu, W. Luo, P. Soliz, and R. Kardon (2011) "Automated analysis of optic nerve images for detection and staging of papilledema," *Investigative Ophthalmology & Visual Science*, vol. 52, pp. 7470–7478.

[65] M. Gao, H. Chen, S. Zheng, and B. Fang (2016) "A factorization based active contour model for texture segmentation," *Proceeding in IEEE International Conference on Image Processing*, pp. 4309–4313.

[66] Thammasat Eye Center, Thammasat University Hospital (Thailand) (2019) Mobile Camera Retinal Collections. http://www.tec.in.th/. (Accessed 9 July 2019)

[67] Volk (2017) Volk iNview retinal camera. In: Volk Optical Inc. https://volk.com/index.php/volk-products/ophthalmic-cameras/volk-inview/. (Accessed 1 September 2017)

[68] A. Hoover and M. Goldbaum (1975) "The STructure Analysis of the REtina (STARE) project," http://www.ces.clemson.edu/~ahoover/stare/. (Accessed 1 September 2016)

[69] Retinopathy of Prematurity (2020) EyeWiki https://eyewiki.aao.org/Retinopathy_of_Prematurity. (Accessed 1 June 2020)

[70] T. Kauppi, V. Kalesnykiene, and J. Kamarainenetal (2006) "DIARETDB0: Evaluation database and methodology for diabetic retinopathy algorithms," Machine Vision and Pattern Recognition Research Group, Lappeenranta University of Technology, Lappeenranta, Finland.

[71] T. Kauppi, V. Kalesnykiene, and J. Kamarainenetal (2007) "The DIARETDB1diabetic retinopathy database and evaluation protocol," *British Machine Vision Conference* (BMVC'07), Warwick, UK. pp.1–10.

[72] W. F. Hoyt, "The William F. Hoyt Neuro-Ophthalmology Collection," https://novel.utah.edu/Hoyt/ (Accessed on 28 January 2022).

[73] L. Cen, J. Ji, J. Lin, S. Ju, H. Lin, et al., (2021) "Automatic detection of 39 fundus diseases and conditions in retinal photographs using deep neural networks," *Nature Communications*, 12:4828.

[74] D. E. Kusumandari, A. Munandar, and G. G. Redhyka (2015) "The comparison of GVF snake active contour method and ellipse fit in optic disc detection for glaucoma diagnosis," *Proceeding in International Conference on Automation, Cognitive Science, Optics, Micro Electro-Mechanical System, and Information Technology*, pp. 123–126.

[75] T. T. Khaing, T. Ruennark, P. Aimmanee, S. Makhanov, and N. Kanchanaranya (2021) "Glaucoma detection in mobile phone retinal images based on ADI-GVF segmentation with EM

initialization," *ECTI Transactions on Computer and Information Technology*, vol. 15, no. 1, pp. 134–149.

[76] S. W. Wilson and H. S. Mahesh (2014) "Automatic detection of optic disc and optic cup using simple linear iterative clustering," *International Journal of Engineering Research and Technology*, vol. 3, no. 7, pp. 984–988.

[77] Z. Hu, X. Wu, Y. Ouyang, Y. Ouyang, and S. R. Sadda (2013) "Semiautomated segmentation of the choroid in spectral-domain optical coherence tomography volume scans," *Investigative ophthalmology & visual science (iovs)*, vol. 54, pp. 1722–1729.

[78] H. Danesh, R. Kafieh, H. Rabbani, and F. Hajizadeh (2014) "Segmentation of choroidal boundary in enhanced depth imaging OCTs using a multiresolution texture-based modeling in graph cuts," *Computational and Mathematical Methods in Medicine*, vol, 2014, 479268.

[79] B. Salafian, R. Kafieh, A. Rashno, M. Pourazizi, and S. Sadri (2018) "Automatic segmentation of choroid layer in EDI OCT images using graph theory in neutrosophic space," *arXiv: Image and Video Processing*.

[80] C. Wang, Y. X. Wang, and Y. Li (2017) "Automatic choroid layer segmentation using Markov random field and level set method." *IEEE Journal of Biomedical and Health Informatics*, vol. 21, no. 6, pp. 1694–1702.

[81] S. Masood, B. Sheng, P. Li, R. Shen, R. Fang, and Q. Wu (2017) "Automatic choroid layer segmentation using normalized graph cut," *The Institution of Engineering and Technology (IET)*, vol. 4, no. 3, pp. 397–411.

[82] Q. Chen, W. Fan, S. Niu, J. Shi, H. Shen, and S, Yuan (2015) "Automated choroid segmentation based on gradual intensity distance in HD-OCT images, *Optics Express*, vol. 23, no. 7, pp. 8974–8994.

[83] J. Tian, P. Marziliano, M. Baskaran, T. A. Tun, and T. Aung (2013) "Automatic segmentation of the choroid in enhanced depth imaging optical coherence tomography images," *Biomedical Optics Express*, vol. 9, no. 7, pp. 3049–3065.

[84] M. A. Hussian, A. Bhuiyan, H. Ishikawa, R. T. Smith, J. S. Schuman, and R. Kotagiti (2018) "An automated method for choroidal thickness measurement from enhanced depth imaging optical coherence tomography images," *Computerized Medical Imaging and Graphics*, vol. 63, pp. 41–51.

[85] H. Lu, N. Boonarpha, M. T. Kwong, and Y. Zheng (2013) "Automated segmentation of the choroid in retinal optical coherence tomography images," *35th Annual International Conference of the IEEE EMBS*, pp. 5869–5872.

[86] X. Sui, Y. Zheng, B. Wei, H. Bi, J. Wu, X. Pan, Y. Yin, and S. Zhang (2017) "Choroid segmentation from optical coherence tomography with graph-edge weights learned from deep convolutional neural networks," *Neurocomputing*, vol. 237, pp. 332–341.

[87] S. Masood, R. Fang, P. Li, H. Li, B. Sheng, A. Mathavan, X. Wang, P. Yang, Q. Wu, J. Qin, and W. Jia (2019) "Automatic choroid layer segmentation from optical coherence tomography images using deep learning," *Scientific Reports*, vol. 9, 3058.

[88] J. Kugelman, D. Alonso-Caneiro, S. A. Read, J. Hamwood, S. J. Vincent, F. K. Chen, and M. J. Collins (2019) "Automatic choroidal segmentation in OCT images using supervised deep learning methods," *Scientific Reports*, vol. 9, 13298.

[89] D. Alonso-Caneiro, J. Kugelman, J. Hamwood, S. A. Read, S. J. Vincent, F. K. Chen, and M. J. Collins (2019) "Automatic retinal and choroidal boundary segmentation in OCT images using patch-based supervised machine learning methods," *Asian Conference on Computer Vision (ACCV)*, pp. 215–228.

[90] M. Chen, J. Wang, I. Oguz, B. L. VanderBeek, and J. C. Gee (2017) "Automated segmentation of the choroid in EDI-OCT images with retinal pathology using convolutional neural networks," *Fetal, Infant and Ophthalmic Medical Image Analysis (OMIA)*, pp. 177–184, 10554.

[91] V. Badrinarayanan, A. Kendall, and R. Cipolla (2017) "SegNet: A deep convolutional encoder-decoder architecture for image segmentation," *IEEE Transactions on Pattern Analysis and Machine Intelligence*, vol. 12, no. 12, pp. 2481–2495.

[92] O. Ronneberger, P. Fischer, and T. Brox (2015) "U-net: Convolutional networks for biomedical image segmentation," in *International Conference on Medical Image Computing and Computer-Assisted Intervention (MICCAI)*, pp. 234–241.

[93] S. K. Devalla, P. K. Renukanand, B. K. Sreedhar, G. Subramanian, L. Zhang, S. Perera, J. Mari, K. S. Chin, T. A. Tun, N. G. Strouthidis, T. Aung, A. H. Thiery, and M. J. A. Girard (2018) "DRUNET: a dilated-residual U-Net deep learning network to segment optic nerve head tissues in optical coherence tomography images," *Biomedical Optics Express*, vol. 9, no. 7, pp. 3244–3264.

[94] H. Zhang, J. Yang, K. Zhou, F. Li, Y. Hu, Y. Zhao, C. Zheng, X. Zhang, and J. Liu (2020) "Automatic segmentation and visualization of choroid in OCT with knowledge infused deep learning." *IEEE Journal of Biomedical and Health Informatics*, vol. 24, no. 12, pp. 3408–3420.

[95] W. P. Hsia, S. L. Tse, C. J. Chang, and Y. L. Huang (2021) "Automatic segmentation of choroid layer using deep learning on spectral domain optical coherence tomography," *Applied Sciences*, vol. 11, 5488.

[96] N. Srinath, A. Patil, V. K. Kumar, S. Jana, J. Chhablani, and A. Richhariya (2014) "Automated detection of choroid boundary and vessels in optical coherence tomography images," in *Engineering in Medicine and Biology Society (EMBC), 2014 36th Annual International Conference of the IEEE*, pp. 166–169.

[97] X. Liu, L. Bi, Y. Xu, D. Feng, J. Kim, and X. Xu (2019) “Robust deep learning method for choroidal vessel segmentation on swept source optical coherence tomography images,” *Biomedical Optics Express*, vol. 10, no. 4, pp. 1601–1612.

[98] G. Lin, A. Milan, C. Shen, and I. Reid (2017) “RefineNet: Multi-path refinement networks for high-resolution semantic segmentation,” in *2017 IEEE Conference on Computer Vision and Pattern Recognition (CVPR)*, pp. 5168–5177.

[99] G. Zheng, Y. Jiang, C. Shi, H. Miao, X. Yu, Y. Wang, S. Chen, Z. Lin, W. Wang, F. Lu, and M. Shen (2021) “Deep learning algorithms to segment and quantify the choroidal thickness and vasculature in swept-source optical coherence tomography images,” *Journal of Innovative Optical Health Sciences*, vol. 14, no. 1 (2140002).

[100] Z. Zhang, Q. Liu, and Y. Wang (2018) “Road extraction by deep residual U-Net,” *IEEE Geoscience and Remote Sensing Letters*, vol. 15, pp. 749–753.

[101] H. Zhou, Z. Chu, Q. Zhang, Y. Dai, G. Gregori, P. J. Rosenfeld, and R. K. Wang (2018) “Attenuation correction assisted automatic segmentation for assessing choroidal thickness and vasculature with swept-source OCT,” *Biomedical Optics Express*, vol. 9, no. 12, pp. 6067–6080.

[102] A. F. Agarap (2018) “Deep learning using rectified linear units (RELU),” *Neural and Evolutionary Computing*, arXiv:1803.08375 [cs.NE].

[103] Z. Zhou, Md. M. R. Siddiquee, N. Tajbakhsh, and J. Liang (2018) “U-Net++: A nested architecture for medical image segmentation,” *Computer Vision and Pattern Recognition*, arXiv:1807.10165 [cs.CV].

[104] Z. Al-Ameen, G. Sulong, A. Rehman, A. Al-Dhelaan, T. Saba, and M. Al-Rodhaan (2015) “An innovative technique for contrast enhancement of computed tomography images using normalized gamma-corrected contrast-limited adaptive histogram equalization,” *EURASIP Journal on Advances in Signal Processing*, 2015:32.

[105] F. Yu, and V. Koltun (2016) “Multi-scale context aggregation by dilated convolutions,” in *International Conference on Learning Representations, ICLR*.

[106] L. Chen, G. Papandreou, I. Kokkinos, K. Murphy, and A. L.Yuille (2018) “DeepLab: Semantic image segmentation with deep convolutional nets, atrous convolution, and fully connected CRFs,” *IEEE Transactions on Pattern Analysis and Machine Intelligence*, vol. 40, no. 4, pp. 834–848.

[107] R. Hamaguchi, A. Fujita, K. Nemoto, T. Imaizumi, and S. Hikosaka (2018) “Effective use of dilated convolutions for segmenting small object instances in remote sensing imagery,” *2018 IEEE Winter Conference on Applications of Computer Vision*, vol. 1, pp. 1442–1450.

[108] N. Srivastava, G. Hinton, A. Krizhevsky, I. Sutskever, and R. Salakhutdinov (2014) “Dropout: a simple way to prevent neural networks from overfitting,” *Journal of Machine Learning Research*, vol. 15, pp. 1929–1958.

[109] G. Ghiasi, T. Lin, R. Pang, and Q. V. Le (2019) "NAS-FPN: Learning scalable feature pyramid architecture for object detection," in *IEEE Conference on Computer Vision and Pattern Recognition, CVPR*.

[110] G. Ghiasi, T. Lin, and Q. V. Le (2018) "DropBlock: A regularization method for convolutional networks," In *Conference of Neural Information and Processing Systems, NeurIPS*.

[111] S. Jadon (2020) "A survey of loss functions for semantic segmentation," *IEEE Conference on Computational Intelligence in Bioinformatics and Computational Biology (CIBCB)*.

[112] S. Ioffe and C. Szegedy (2015) "Batch normalization: accelerating deep network training by reducing internal covariate shift," in *Proceedings of the 32nd International Conference on Machine Learning*, vol. 37 (JMLR.org, Lille, France, 2015), pp. 448–456.

[113] M. Drozdzal, E. Vorontsov, G. Chartrand, S. Kadoury, and C.Pal (2016) "The importance of skip connections in biomedical image segmentation," *Deep Learning and Data Labeling for Medical Applications*, pp. 179–187.

[114] N. Kanopoulos, N. Vasanthavada, and R. L. Baker (1988) "Design of an image edge detection filter using the Sobel operator," *IEEE Journal of Solid-State Circuits*, vol. 23, no. 2, pp. 358–367.

[115] D. Kermany, K. Zhang, M. Goldbaum, et al. (2018) "Identifying medical diagnosis and treatable diseases by image-based deep learning," *Cell*, vol. 172, no. 5, pp. 1122–1131.

[116] ibisPaint Application, https://ibispaint.com, last accessed 2021/07/28.

[117] J. Hamwood, D. Alonso-Caneiro, S. A. Read, S. J. Vincent, and M. J. Collins (2018) "Effect of patch size and network architecture on a convolutional neural network approach for automatic segmentation of OCT retinal layers," *Biomedical Optics Express*, vol. 9, no. 7, pp. 3049–3065.

[118] Z. Zhou, Md. M. R. Siddiquee, N. Tajbakhsh, and J. Liang (2018) "U-Net++: A nested architecture for medical image segmentation," *Computer Vision and Pattern Recognition*, arXiv:1807.10165 [cs.CV].

[119] K. J. V. Stralen, K. J. Jager, C. Zoccali, and F. W. Dekker (2008) "Agreement between methods," *Kidney International*, vol. 74, pp. 1116–1120.

[120] A. Chiba, G. Miura, T. Baba, and S. Yamamoto (2019) "Determination of length of interdigitation zone by optical coherence tomography and retinal sensitivity by microperimetry and their relationship to progression of retinitis pigmentosa," *BioMed Research International*, 2019:1217270.

[121] J. den Haan, L. Csinscik, T. Parker, R. W. Paterson, C. F. Slattery, A. Foulkes, F. H. Bouwman, F. D. Verbraak, P. Scheltens, T. Peto, I. Lengyel, J. M. Schott, S. J. Crutch, T. J. Shakespeare, and K. X. X. Yong (2019) "Retinal thickness as potential biomarker in posterior cortical atrophy and typical Alzheimer's disease," *Alzheimer's Research & Therapy*, vol. 11:62.

Acknowledgments

I would like to acknowledge the following supporters who have contributed to my research and helped through my doctoral degree.

First, I would like to express my sincere gratitude to my advisor, Prof. Hideaki Haneishi, for his continuous support, encouragement, motivation, and guidance during my doctoral study at Chiba University. Completing this thesis could not have been possible without his expertise and excellent supervision.

I also would like to express my sincere appreciation to my thesis committee, Prof. Yu Wenwei, Prof. Tadashi Yamaguchi, and Prof. Toshiya Nakaguchi, for their insightful and constructive comments and interesting questions. My sincere thanks also go to Assoc. Prof. Pakinee Aimmanee and Prof. Stanislav S. Makhanov for giving me a great chance to join the double-doctoral-degree program between Sirindhorn International Institute of Technology, Thammasat University, and Chiba University and for acting as my external reviewers for the final thesis review at Chiba University.

Besides my thesis committee, I would like to extend my gratitude to the co-authors, Dr. Takayuki Okamoto, Dr. Chen Ye, Dr. Md Abdul Mannan, Dr. Gen Miura, Dr. Hirotaka Yokouchi, and Dr. Kazuya Nakano. They have been involved in and contributed to my research publications. I also would like to acknowledge the Graduate School of Medicine of Chiba University for permitting the approval of this study. Additional thanks to Dr. Hirotaka Yokouchi for providing OCT data and conducting valuable discussions regarding experiments in this thesis. I am thankful to all editors and reviewers who have given comments and feedback on my publications.

I gratefully acknowledge the NSK Scholarship Foundation for fully providing financial support during my stay in Japan. My sincere thanks to the managing directors of the foundation: Mr. Akira Suzuki and Mr. Nobuhiko Miyake, and the secretaries: Ms. Kazumi Ryutani, and Ms. Mitsuko Ryuzaki, for their warmest help and support. I wish to thank the support provided by JSPS Core-to-Core Program under grant number JPJSCCA20170004.

I sincerely thank our lab secretary, Ms. Shiho Sakata, for her tremendous support in preparing miscellaneous school documents and helping with her kindness in my daily life. I would like to thank Dr. Takashi Ohnishi, Dr. Yoko Kurabuchi, and the former secretary of our lab, Ms. Emi Yamaguchi, for their kind support in both academic and other aspects. I would like to acknowledge the Center for Frontier Medical Engineering for providing me with research facilities. I thank my fellow labmates for offering me a hospitable lab environment that motivates me to conduct research.

Last but not least, I would like to extend my heartfelt gratitude to my parents and elder sisters for the spiritual support and endless love they have given me throughout my life.

2022 August 22
Tin Tin Khaing

List of Publications

- Tin Tin Khaing, Takayuki Okamoto, Chen Ye, Md. Abdul Mannan, Hirotaka Yokouchi, Kazuya Nakano, Pakinee Aimmanee, Stanislav S. Makhanov, and Hideaki Haneishi (2021) ChoroidNET: a dense dilated U-Net model for choroid layer and vessel segmentation in optical coherence tomography images, *IEEE Access,* 9:150951-150965. (DOI: 10.1109/ACCESS.2021.3124993)

- Tin Tin Khaing, Pakinee Aimmanee, Stanislav S. Makhanov, and Hideaki Haneishi (2022) Vessel-based Hybrid Optic Disc Segmentation Applied to Mobile-Phone Camera Retinal Images, *Medical & Biological Engineering & Computing*, 60:421-437. (DOI: 10.1007/s11517-021-02484-x)

- Tin Tin Khaing, Takayuki Okamoto, Chen Ye, Md. Abdul Mannan, Gen Miura, Hirotaka Yokouchi, Kazuya Nakano, Pakinee Aimmanee, Stanislav S. Makhanov, and Hideaki Haneishi (2022) Automatic measurement of choroidal thickness and vasculature in optical coherence tomography images of eyes with Retinitis Pigmentosa, *Artificial Life and Robotics*, 27:70-79. (DOI: 10.1007/s10015-022-00737-y)

Conference Proceeding

- Tin Tin Khaing, Himasara Navanjana Warnakulasuriya, Darshil Bagadia, Pakinee Aimmanee, and Hideaki Haneishi (2022) Automatic segmentation of swelling optic disc using factorized gradient vector flow, *International Conference on Electrical Engineering/Electronics, Computer, Telecommunications and Information Technology (ECTI-CON),* Huahin, Thailand. (May 24-27, 2022). (Doi: 10.1109/ECTI-CON54298.2022.9795601)